NORTHWESTERN UNIVERSITY

High-Temperature Cast Aluminum for Efficient Engines

A DISSERTATION

SUBMITTED TO THE GRADUATE SCHOOL
IN PARTIAL FULFILLMENT OF THE REQUIREMENTS

for the degree

DOCTOR OF PHILOSOPHY

Field of Materials Science and Engineering

By

Andrew C. Bobel

EVANSTON, ILLINOIS

June 2017

ⓒ Copyright by Andrew C. Bobel 2017

All Rights Reserved

ABSTRACT

High-Temperature Cast Aluminum for Efficient Engines

Andrew C. Bobel

Accurate thermodynamic databases are the foundation of predictive microstructure and property models. An initial assessment of the commercially available Thermo-Calc TCAL2 database and the proprietary aluminum database of QuesTek demonstrated a large degree of deviation with respect to equilibrium precipitate phase prediction in the compositional region of interest when compared to 3-D atom probe tomography (3DAPT) and transmission electron microscopy (TEM) experimental results. New compositional measurements of the Q-phase (Al-Cu-Mg-Si phase) led to a remodeling of the Q-phase thermodynamic description in the CALPHAD databases which has produced significant improvements in the phase prediction capabilities of the thermodynamic model.

Due to the unique morphologies of strengthening precipitate phases commonly utilized in high-strength cast aluminum alloys, the development of new microstructural evolution models to describe both rod and plate particle growth was critical for accurate mechanistic strength models which rely heavily on precipitate size and shape. Particle size measurements through both 3DAPT and TEM experiments were used in conjunction with literature results of many alloy compositions to develop a physical growth model for the independent prediction of rod radii and rod length evolution. In addition a machine learning (ML) model was developed for the independent prediction of plate thickness and plate diameter evolution as a function of alloy composition, aging temperature, and aging time. The developed models are then compared with physical growth laws developed for spheres and modified for ellipsoidal morphology effects.

Analysis of the effect of particle morphology on strength enhancement has been undertaken by modification of the Orowan-Ashby equation for $\langle 110 \rangle_{\alpha\text{-}Al}$ oriented finite rods in addition to an appropriate version for similarly oriented plates. A mechanistic strengthening model was developed for cast aluminum alloys containing both rod and plate-like precipitates. The model accurately accounts for the temperature dependence of particle nucleation and growth, solid solution strengthening, Si eutectic strength, and base aluminum yield strength. Strengthening model predictions of tensile yield strength are in excellent agreement with experimental observations over a wide range of aluminum alloy systems, aging temperatures, and test conditions. The developed models enable the prediction of the required particle morphology and volume fraction necessary to achieve target property goals in the design of future aluminum alloys.

The effect of partitioning elements to the Q-phase was also considered for the potential to control the nucleation rate, reduce coarsening, and control the evolution of particle morphology. Elements were selected based on density functional theory (DFT) calculations showing the prevalence of certain elements to partition to the Q-phase. 3DAPT experiments were performed on Q-phase containing wrought alloys with these additions and show segregation of certain elements to the Q-phase with relative agreement to DFT predictions.

Acknowledgments

I would like to thank all the people who have supported me and my research here at Northwestern and at General Motors. First, I would like to thank my adviser Prof. Greg Olson for his guidance and support throughout my time in his group. Your immeasurable incite into all things materials is an irreplaceable source of knowledge. I hope to always "expect victory!" and continue to represent the group on the field of valor. Thank you to all my committee members, Prof. Wolverton, Prof. Voorhees, and Dr. Hatcher, for agreeing to be on my committee and for the helpful discussions regarding my research.

Thanks goes to all the past and present members of the Olson group who have helped me throughout this process, your support is immeasurable. Amit, thank you for maintaining both Wiglaf and Thor2, and well as having great suggestions for LEAP analysis. Nick your help with sample preparation was very much appreciated. Thank you Ricardo, for the many helpful discussions without which this project would not have gone as smoothly. Thank you Dana, for helping me get started on the APT and for continuing on with the project at QuesTek. Ricardo, Fan, and Wei is was a pleasure sharing an office with you. Kazu together we learned how to make 3D figures, hopefully you can put that knowledge to use in your future. Amit, Fuyao, Fan, and Chuan good luck finishing up your doctoral work, I wish you all the best.

To all the students, faculty, and staff at Northwestern who have assisted with my research, thank you. Thank you Logan, your machine learning code and knowledge of programming was invaluable. Kyoungdoc, thank you for all the support you provided me on the first-principles front. For all those at NU*ANCE*, specifically Jinsong, Ben, Shuyou, and Karl your help on the TEM, SEM, and FIB was invaluable. Dieter, thank you for all your assistance on the APT and maintaining the NUCAPT facility, which was so crucial for my

research. Carla, your support in the OMM lab was much appreciated.

To all those at QuesTek, your collaboration and support throughout this project has been immense, especially Nick, Weiwei, Dana, Abhinav, and Dave. Your guidance and assistance on both all things Thermo-Calc and in the lab was especially helpful. Weiwei, without you we would never had had the database we have today, thank you. Abhinav, it was a pleasure working on the modeling side with you, and thank you for all your help with sample preparation. To all those at General Motors, for giving me this opportunity and allowing me to intern over the course of my Ph.D., thank you. Anil, thank you for your support and mentorship, I look forward to continuing to work with you at GM. To Mike for guiding the project throughout and supporting me whenever I needed anything, thank you so much. To Vik and Ratan for your assistance on the TEM, Bob and Ina for helping me with sample preparation and on the SEM, thank you.

To all my friends I've made here at NU, especially Jorge and Ashley, Logan, Jeff, Vuk, Dinç, and Ethan. Your many years of friendship have given me some of the best memories I will cherish for the rest of my life. To my mother, your love and support throughout my academic career and personal life have led me to where I am today, this would not have been possible without your continued belief in me. I am so grateful for everything you have done and everything I know you will continue to do. To my girlfriend, Caitlin, I'm so happy that I have you in my life. I love you.

This material is based upon work supported by the Department of Energy under Award Number DE-EE0006082. This work made use of the EPIC facility of Northwestern University's NUANCE Center, which has received support from the Soft and Hybrid Nanotechnology Experimental (SHyNE) Resource (NSF ECCS-1542205); the MRSEC program (NSF DMR-1121262) at the Materials Research Center; the International Institute for Nan-

otechnology (IIN); the Keck Foundation; and the State of Illinois, through the IIN. APT measurements were performed at the Northwestern University Center for Atom-Probe Tomography (NUCAPT). Funding for the purchase of the LEAP tomograph and for upgrades was generously provided by NSF-MRI (DMR 0420532), ONR-DURIP (N00014-0400798) and ONR-DURIP (N00014-0610539).

Disclaimer: This report was prepared as an account of work sponsored by an agency of the United States Government. Neither the United States Government nor any agency thereof, nor any of their employees, makes any warranty, express or implied, or assumes any legal liability or responsibility for the accuracy, completeness, or usefulness of any information, apparatus, product, or process disclosed, or represents that its use would not infringe privately owned rights. Reference herein to any specific commercial product, process, or service by trade name, trademark, manufacturer, or otherwise does not necessarily constitute or imply its endorsement, recommendation, or favoring by the United States Government or any agency thereof. The views and opinions of authors expressed herein do not necessarily state or reflect those of the United States Government or any agency thereof.

Contents

List of Figures

List of Tables

1 Introduction

Lightweight cast aluminum alloys have been increasingly used in the automotive industry to replace cast iron, reduce vehicle mass, and increase fuel efficiency. With growing demands for higher fuel economy, increasing demands for high temperature tensile, fatigue, and creep properties have become critical. Current analysis into the property requirements for future engine designs have led to the need for the development of new innovative cast aluminum alloys that can meet the property requirements of higher operating engine temperatures while maintaining the good castability and ductility of currently used alloys. To use a systems design and integrated computational materials engineering (ICME) approach, it is critical to have refined thermodynamic databases for the compositional space of interest and state-of-the-art computational models for property predictions. This approach for the design of new alloys allows for the elimination of the previously common trial-and-error method of materials development.

Computational engineering of new high-performance materials has drastically reduced the time and cost necessary to go from concept to production with the development of computational thermodynamics, kinetics, and integrated computational materials engineering (ICME) design tools. The design of a novel high-temperature cast aluminum alloy must utilize strengthening effects of all forms: precipitation strengthening, eutectic modification, and solid solution strengthening. Such an alloy should improve on and produce more thermally stable phases at the operating temperature of interest, while still maintaining the combination of fluidity, freezing range, and reduction of defect formation of legacy alloys. This work focuses on the development and refinement of computational tools and databases needed for the design of a thermally stable Q-phase containing cast aluminum alloy. It is noteworthy that the ICME tools needed for the design of such an alloy are severely lacking, and thus the development and advancement of the necessary tools focusing on high-temperature stable strengthening phases will make feasible the development of future alloy designs. This work aims to fully understand the quaternary Q-phase, in terms of both thermodynamics and kinetics. The composition of the Q-phase is explored via atom probe tomography (APT) and is used to create a new CAlculation of PHase Diagram (CALPHAD) thermodynamic description of the Q-phase and improve the observed phase boundaries of competing phases. The kinetics of growth and coarsening of the Q-phase are explored via transmission electron microscopy (TEM) in many wrought and cast prototype alloys developed to understand the impact of aging time, temperature, and phase competition. The observed kinetics of coarsening is then modeled via machine learning techniques and compared to classical theory. Following this analysis, the effect of particle size and shape on precipitation strengthening is explored via the Orowan-Ashby description and is updated for finite rods. This work then presents a mechanistic model for the prediction of tensile strength for rod and plate containing alloys that is applicable for both aging and testing at ambient and high operating temperatures. This work concludes with an assessment of the impact of trace elemental additions to Q-phase containing alloys and their predicted and observed partitioning.

1.1 Motivation

Since 1990 the U.S. transportation sectors petroleum consumption has exceeded U.S. domestic production, with the transportation sector alone accounting for 70% of the total

U.S. petroleum use in 2015 [1]. To ease the U.S. dependence on petrol for the more than 114 million cars and 125 million light trucks in the U.S as of 2015, the Department of Energy (DoE) Energy Efficiency and renewable Energy Program has target a 25% lighter powertrain by 2025 and 40% lighter powertrain by 2050. This will result in a significant increase to engine energy density, with higher exhaust temperatures, and cylinder pressures. To meet these new requirements, new state-of-the-art aluminum alloys with substantially improved properties are required. With the average time to implement a new alloy into production being 10 years, traditional methods of experimental trial and error are no longer viable for alloy development.

This work is part of the collaboration between Northwestern University (Evanston, IL), General Motors (Detroit, MI), and QuesTek Innovations (Evanston, IL) for the advancement of cast aluminum alloys for high-temperature applications. This is part of the DoE's development of new energy-efficient and environmentally friendly technologies to reduce America's dependence on foreign petroleum and reduce greenhouse gas emissions. The project aims to combine ICME with advanced analytical tools to drastically reduce the time necessary to design a new light-weight cast-alloy with the desired high-temperature properties to meet the demands of future engine applications. This research intends to support the necessary ICME tools needed for the alloy development, by understanding the main strengthening precipitate phase of interest, the Q-phase, and developing the models necessary to accurately predict properties of interest at relevant conditions.

1.2 Background

1.2.1 Aluminum Alloy Overview

Aluminum alloys are divided into two major categories: wrought and cast, and can be further categorized into either heat-treatable or non heat-treatable depending on if they utilize precipitation strengthening to achieve their target properties. Wrought and cast alloy naming conventions have been developed, with wrought alloys having a four-digit system and cast having a three-digit system and a decimal denoting ingot compositions. The number designation systems for both wrought and cast aluminum alloys is shown in Table 1.1. Those alloy systems containing both Mg, Si, and Cu additions are of most interest for this project since those are the necessary elements for the Q-phase to form, such as the wrought 2xxx and 6xxx series systems, and the cast 3xx.x series system. These alloy systems are heat-treatable and are strengthened by a number of precipitate phases. After casting, heat-treatable alloys are given a solution/homogenization treatment and then quenched to create a supersaturated solid solution (SSSS). Upon artificial aging at higher temperatures, Guiner-Preston (GP) zones begin to nucleate on clusters of solute atoms, vacancies, or dislocations [2, 3, 4]. After further aging the GP zones grow to become metastable intermediate precipitates, where the peak strength of the alloy is often obtained [5, 6]. Upon further aging, equilibrium precipitate phases will form, either nucleating on or transforming from the metastable phases. At this state the alloy is considered overaged and corresponds to a decrease in strength, typically due to large particle sizes and low number densities. Equilibrium phases present in the overaged alloy vary based on the composition and the aging temperature, and in most systems often results in multiple phases being present. A list of common strengthening phases found in the Al-Si-Mg-Cu system is given in Table 1.2.

Table 1.1: Aluminum alloy designations.

Wrought Alloy Systems			Cast Alloy Systems		
Series	Primary Alloying Element(s)	Secondary Additions	Series	Primary Alloying Element(s)	Secondary Additions
1xxx	>99.0% pure Al		1xx.x	>99.0% pure Al	
2xxx	Cu	Mg, Li	2xx.x	Cu	
3xxx	Mn		3xx.x	Si	Cu, Mg
4xxx	Si	Mg	4xx.x	Si	
5xxx	Mg		5xx.x	Mg	
6xxx	Mg, Si		6xx.x	Ununsed	
7xxx	Zn	Cu, Mg,Cr, Zr	7xx.x	Zn	Cu, Mg
8xxx	Sn, Li	Zr, B	8xx.x	Sn	

Table 1.2: Common strengthening phases in the Al-Si-Mg-Cu system.

Phase	Approx. Composition	Shape	Ref.
θ’	Al_2Cu	Plate	[7, 8]
β"	Mg_5Si_6	Rod	[9, 10, 11, 12]
β’	Mg_9Si_5	Rod	[13, 14]
S’	Al_2MgCu	Rod	[15, 16]
Q	$Al_5Cu_2Mg_8Si_6$	Rod	[17, 18, 19]

The known stable phases in the Al-Si-Mg-Cu system are shown in Figure 1.1, on a Gibbs tetrahedron projected down the Si axis. The Open Quantum Materials Database (OQMD), a database of DFT-calculated thermodynamic and structural properties, was used to search for all stable compounds in the quaternary Al-Si-Mg-Cu system [20, 21]. The stable θ (Al_2Cu), β (Mg_2Si), S (Al_2MgCu), and Q-phases ($Al_3Cu_2Mg_9Si_7$), as identified by DFT calculations, are present. The θ’-phase is one of the most important strengthening phases in aluminum alloys and has a long history of important implications in understanding materials. The θ'-phase was at the heart of the discovery of the phenomenon of precipitation hardening in 1911 by Wilm [22], and was also the precipitate system used by Guinier and Preston to decsribe the structural cause of hardneing in Al-Cu alloys in the 1930's [2, 3]. The crystal structure of the θ'-phase is well accepted: it is body-centered tetragonal (*I4/m*) with lattice constants $a = 4.04$ Å, $c = 5.80$ Å, and having a platelet morphology with coherent $(001)_{\theta'}||\{001\}_{\alpha\text{-}Al}$ interfaces parallel to their broad faces [8, 23, 24]. The θ'-phase is allotropic to the equilibrium θ-phase which occurs upon further aging and has the C16 (*I4/mcm*) structure.

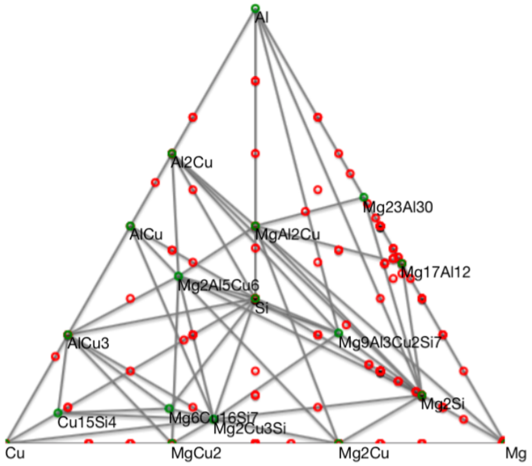

Figure 1.1: Gibbs tetrahedron for the Al-Si-Mg-Cu system showing all stable phases as identified by the OQMD.

The β" (Mg_5Si_6) and β' (Mg_9Si_5) phases are commonly occurring rod-shaped Mg and Si rich precipitate phases that are just two of the many equilibrium β (Mg_2Si) phase precursors that have been reported. The β"-phase has been found to be monoclinic (*C2/m*), with cell parameters $a = 15.16$ Å, $b = 4.05$ Å, $c = 6.74$ Å, and $\beta = 105.3°$ [9, 10, 11, 12].

Upon aging, much like the θ' to θ transition, a crystallographic transformation occurs as β" becomes β'. The β'-phase has a reported hexagonal crystal structure (*P6*$_3$ or *P6*$_3$*/m*), with cell parameters $a = b = 7.05 - 7.15$ Å and $c = 4.05$ Å or $c = 1.215\ nm$ [14, 25, 26, 27]. The β' rods are fully coherent with the $\langle 100\rangle_{\alpha\text{-}Al}$ along the c-axis. The equilibrium form of the β phase (Mg_2Si) is cubic (*Fm-3m*) with $a = 0.635\ nm$ and forms plates or cuboids with dimensions several micrometers long [13, 14].

The S'-phase is a rod/lath-shaped metastable strengthening phase found in Al-Mg-Cu alloys, such as the 2xxx series. The S'-phase is a reported precursor for the equilibrium S-phase (*Cmcm*, $a = 0.4000\ nm, b = 0.923\ nm, c = 0.714\ nm$) [28, 29] with a composition of Al_2MgCu. Both are reported to be similar in composition and structure, such that evidence to justify differentiating from such a metastable S" or S' from the equilibrium S-phase does not appear to be warranted [16]. The S'-phase rods are extended along the $\langle 100\rangle_{\alpha\text{-}Al}$ direction and exhibit an $\{210\}_{\alpha\text{-}Al}$ habit plane, though it has been reported that the habit plane can be rotated by several degrees from $\{210\}_{\alpha\text{-}Al}$ [30].

The equilibrium Al-Cu-Mg-Si quaternary, or the "Q-phase", is a precipite phase that occurs in many types of Al alloys, from cast 3xx.x alloys [31], wrought 2xxx [32, 33] and 6xxx [32, 34, 35] series alloys, and even Al-matrix composites [33]. The Q-phase has a hexagonal crystal structure with lattice constants $a = 10.35 - 10.40$ Å and $c = 4.02 - 4.05$ Å with 21 atoms per unit cell and a proposed crystal structure related to the Th_7S_{12} structure with Si replacing Th, Al and Mg atoms placed on S sites, and Cu located at voids [17, 18, 35]. The Q-phase has a lath or rod-like morphology [31, 36], whose dimensions have been reported to range from $2.0 - 5.0\ nm^2$ for the cross-section and from $60 - 100\ nm$ in length [34]. The Q-phase rods are extended along the $\langle 100\rangle_{\alpha\text{-}Al}$ direction with a $\{510\}_{\alpha\text{-}Al}$ habit plane and orientation relationship with the matrix of either $[0001]_Q||[001]_{\alpha\text{-}Al}$ and $(11\bar{2}0)_Q||(510)_{\alpha\text{-}Al}$, or $[0001]_Q||[001]_{\alpha\text{-}Al}$ and $(21\bar{3}0)_Q||(100)_{\alpha\text{-}Al}$ [37, 38]. Though a commonly occurring phase, relatively little is known about the Q-phase; even the composition is controversial. Reported stoichiometries include $Al_4Cu_2Mg_8Si_7$ [18], $Al_5Cu_2Mg_8Si_6$ [19] which is the most widely used in CALPHAD databases, $Al_4CuMg_5Si_4$ [15], and $Al_3Cu_2Mg_9Si_7$ [17]. A more detailed review of the Q-phase composition will be given in Chapter 3.

In today's automotive applications, the most commonly used cast aluminum alloys for cylinder head applications are A356, 319, and AS7GU (A356+0.5%Cu) [39]. A356 is widely used for its good room temperature ductility and fatigue properties, yet above 200°C the tensile strength of the alloy rapidly drops due to coarsening of the β' phase precipitates into the equilibrium β (Mg_2Si) phase. The Cu containing 319 is a cheaper alternative to the A356 alloy and is primarily strengthened by θ' precipitates, which has the largest strengthening enhancement of any known phase in the Al system [31, 36]. 319 has a higher tensile strength than A356 at temperatures <200°C but the additional strength is lost at higher temperatures due to the rapid coarsening of the θ' precipitates. Alloy 319 is further hampered by shrinkage porosity and poor room temperature ductility, due to the high Fe and Cu contents. The recently-developed AS7GU alloy [39], which is a variant of the A356 alloy with 0.5 wt.% Cu, is strengthened primarily by the Q-phase, and shows an enhancement in creep resistance and tensile strength at room temperature and elevated temperatures over both A356 and 319 [40]. Above 250°C all three alloys show similar fatigue properties and are drastically reduced compared to their room temperature data due to continued coarsening of their strengthening phases. Thus the need for a thermally stable microstructure is necessary for the design of novel alloys that meet the increasingly higher demand of future applications.

1.2.2 Material Objectives

For an automotive alloy, specifications have been given by the DoE and GM to meet the design requirements needed in future cylinder head applications and are summarized in Table 1.3. Listed baseline properties are based on alloy 356 sand cast properties taken from Table 7 of the ASM Handbook Volume 15: Casting [41]. Both the ultimate tensile strength

Table 1.3: Future Alloy Design Requirement Matrix.

Property	Temperature	Baseline	Targets	
		DOE Cast Al	DOE Proposal	GM Proposal
Ultimate Tensile Strength (MPa)	Room Temp	227.5	275.8	300
	150°C	N/A	N/A	280
	250°C	51.7	N/A	100
	300°C	N/A	65.5	65.5
Yield Strength (MPa)	Room Temp	165.5	206.8	210
	150°C	N/A	N/A	200
	250°C	34.5	N/A	75
	300°C	N/A	44.8	45
Plastic Elongation (%)	Room Temp	3.5	3.5	>3.5
Fatigue Strength at 10^7 cycles	Room Temp	58.6	75.8	N/A
	150°C	N/A	N/A	70
	250°C	N/A	N/A	50
Density (g/cm^3)	Room Temp	2.7	<6.4	<6.4
Fluidity	–	Excellent	Excellent	Same as 319
Hot Tearing Resistance	–	Excellent	Excellent	Same as 319
Manufacturing Cost	–	–	<110% Baseline	<110% Baseline

(UTS) and the yield strength (YS) need to see improvement across all temperature ranges. At room temperature, the UTS and YS need to be improved to 300 Mpa and 210 MPa, respectively, but are of secondary importance to the high temperature UTS and YS properties. At an operating temperature of 300°C the UTS is required to be 65.5 MPa, while the YS is 45 MPa. Plastic elongation has been designated as another critical factor and needs to be as good or better than 3.5% at room temperature. Automotive cylinder heads undergo high-temperature fatigue and has been identified as a key target property. Both tenisle and fatigue performance are impacted by porosity, oxide films, dendrite arm spacing (DAS), silicon eutectic and intermetallic particles, and matrix strength, and the reader is encouraged to read the recent summarization by Wang *et al.* [42, 43]. To improve high temperature fatigue performance it is critical to minimize casting defects, which can depend on melt quality, mold filling, and solidification conditions. These processing conditions are beyond the scope of this work and are left to be controlled and modeled by GM. For an automotive alloy the affordability constraint is required, such that no expensive alloying elements are added to the design or those that will require special recycling of scrap material. This is typically done to eliminate Sc and Li from consideration.

To demonstrate current alloy UTS and YS properties with the desired targets set by GM, Figure 1.2 compares both strength properties versus testing temperature. Tensile tests were performed by GM and for each testing temperature the A356 alloy was held for 200 hrs from a peak aged condition. Alloy A356 UTS drops as much as 86% and YS drops 84% from room temperature to desired operating temperature conditions. As can be seen UTS and YS drop sharply from 150°C to 200°C. The desired targets (in red) call for higher UTS and YS properties at all temperatures >200°C, while room temperature properties are already attained by current alloys. To further combat fatigue a yield strength that does not converge on the tensile strength is also desired, such that the alloy maintains the ability to work harden with load and thus has a better ability of resisting fatigue that currently plagues aluminum alloys.

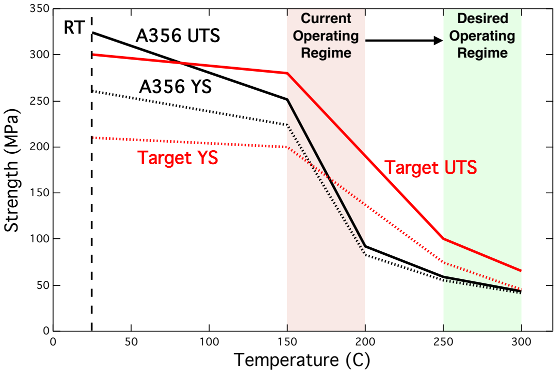

Figure 1.2: UTS and YS data for A356 aged for 200 hrs at temperature compared to GM project objectives.

1.2.3 Systems Design Approach

To properly and efficiently implement the powerful tools of ICME design, one must first understand the complex interactions of all sub-systems within materials. Given the inherent complexity of materials, this project employs a systems design approach, in which the material is treated as a system of hierarchical structures with reciprocal relationships between processing, structure, properties, and performance. This concept of materials was first proposed by C.S. Smith [44]. Once property objectives have been established, the three-link chain of Figure 1.3, which demonstrates the reciprocity proposed by Cohen in the 1970’s [45], can serve as a back bone upon which Smith’s hierarchical sub-systems can be applied. The reciprocity can be interpreted as moving up or down the three-link chain of Figure 1.3.

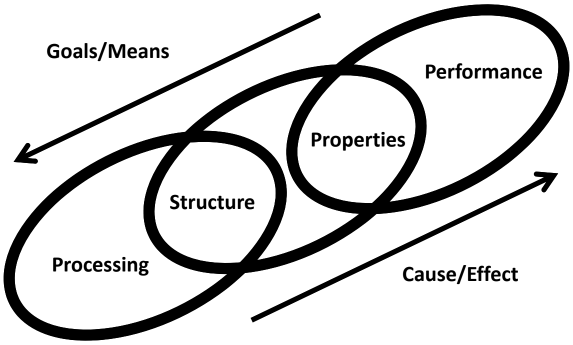

Figure 1.3: Interrelation between processing, structure, properties, and performance [46].

Working up the chain corresponds the the traditional cause/effect approach of understanding materials science, where processing affects structure, structure affects the materials properties, while the properties give a level of performance to the material. Working down the chains goal/means framework provides the basis for materials design. The process of materials design begins with defining the desired materials performance. The properties that produce the desired performance objectives are then determined and the structures that yield those properties are then identified. Finally, the processing steps necessary to produce those structures are selected. This framework of relating internal microstructure sub-systems to overall material properties can be applied to all cases of materials. The exercise of representing the full system and identifying key structure-property and processing-structure links has been undertaken for the case of a high-temperature aluminum precipitation strengthened system, and is represented in the systems design chart in Figure 1.4. Those subsystems of interest relating to precipitation strengthening are highlighted.

Primary relationships in the system design chart are represented by lines connecting the dependent subsystems. These relationships correspond to hierarchical computational

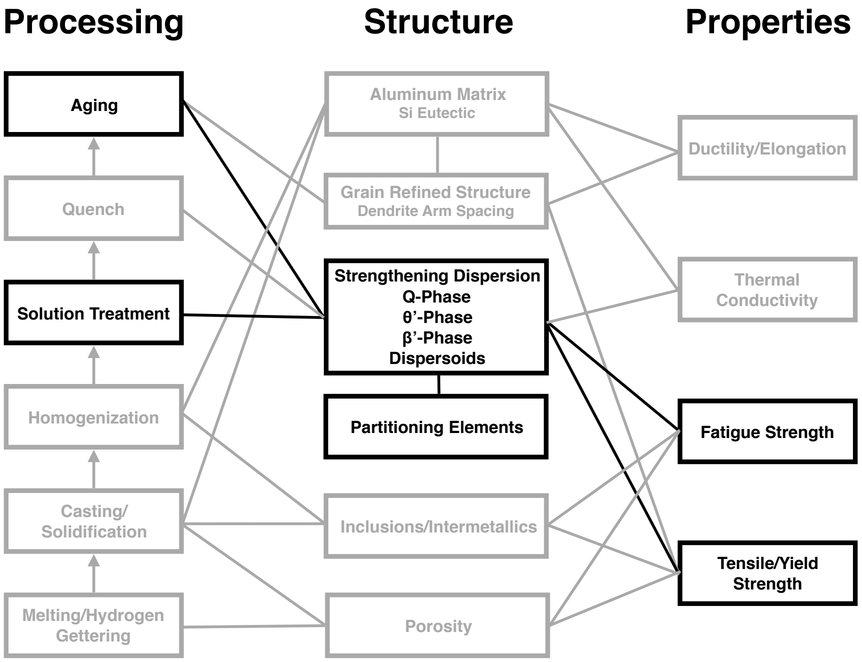

Figure 1.4: Systems design chart for a high-temperature precipitation strengthened aluminum alloy.

design tools and empirical observations that are used to predict the given subsystem. The individual computational design tools are developed from experimental research on the structure subsystems. In this research the computational models to describe the relationships between subsystems are developed to accurately calculate the property of tensile yield strength. The flow chart in Figure 1.5 displays the experiments and computational models utilized to predict a given alloys YS and how the experimental results are used as input in developing the computational models. To predict the strengthening dispersion substructure aging studies are performed on a series of alloys. APT, TEM, and SEM experiments can be used to identify all stable phases after aging for a given alloy composition and temperature.

These stable phases are compared to those predicted by Thermo-Calc simulations, and the thermodynamic databases can be adjusted to accurately reflect experimental observations. APT and TEM experiments are also used to measure particle morphology. These results are used to create a model that can predict precipitate morphology given an alloy composition, aging time, and temperature. These thermodynamic and particle morphology models correspond to the highlighted relationships connecting the processing and structure columns of the system design chart. By performing mechanical tests and utilizing the microstructural information obtained via APT and TEM a mechanistic strengthening model can be produced. The strengthening model corresponds to the relationship linking the strengthening dispersion and tensile yield strength substructures in the systems design chart. In this way the systems design approach drives the work discussed in this research.

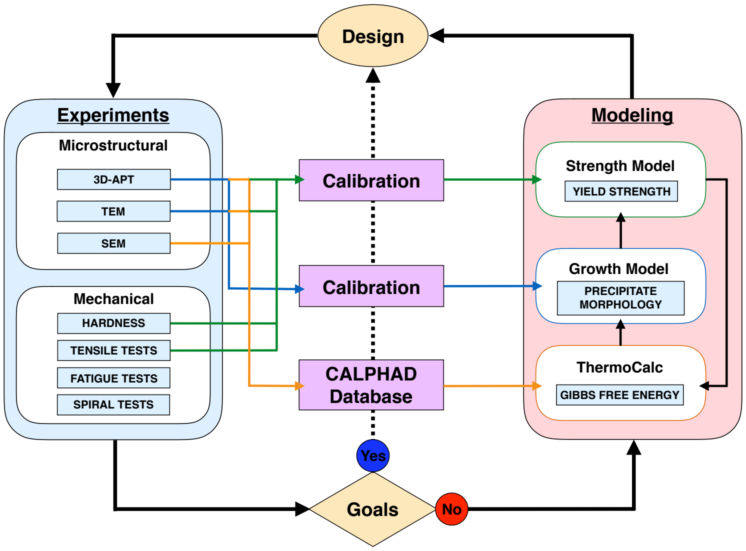

Figure 1.5: Flow chart for incorporating analytical experimental techniques and computational models into materials design.

2 Computational Tools and Experimental Methods

This chapter will provide an overview of the various computational tools and experimental methods used throughout this work. Individual tools and techniques developed for this project will be discussed in detail in their respective chapters.

2.1 Computational Design Tools

Advanced computational models are critical in quantifying the sub-structures associated with a system and understanding the reciprocal relationships between them. The use of such models reduces the need for experimentation and accelerates the design process. The advanced thermodynamic software package Thermo-Calc provides the framework for modeling the materials structure and is directly correlated to the quality of the database used. First-principles calculations based on density functional theory (DFT) are used to calculate phase and interfacial properties that would otherwise be difficult to measure experimentally. In addition, DFT calculations are used to predict and filter for solute partitioning and exotic phases. Machine learning (ML) is a useful tool for predicting properties of interest given that a large enough data set has been produced. Here the use of an ML model is used to predict the growth and coarsening of plate-like particles, where currently a physical model does not exist.

2.1.1 Thermo-Calc

Thermo-Calc is a thermodynamic software package developed by the Royal Institute of Technology in Stockholm, Sweden (KTH) [47]. Thermo-Calc uses the CALculation of PHase Diagram (CALPHAD) approach to make calculations at thermodynamic equilibrium and user constrained/partial equilibrium conditions for multicomponent systems. By defining temperature, pressure, composition, and present phases, Thermo-Calc calculates Gibbs free energies using a given thermodynamic database and performs global minimization to handle complex heterogeneous interactive systems and output equilibrium thermodymanic values. In this research, Thermo-Calc is used to calculate compositions and phase fractions of α-Al matrix, precipitate phases, and Si eutectic at homogenization and aging temperatures. Solidification predictions are also performed using Scheil-Gulliver simulations, which assume the diffusion coefficients of the components in the liquidus phases are infinite while those in the solidified phases are zero [48, 49].

2.1.2 Thermodynamic Databases

The calculations of Thermo-Calc are limited by the quality of the thermodynamic database used for the simulation. The following are the two primary databases used in this research for modeling the Al-Si-Mg-Cu system.

TCAL2 Thermo-Calc Software Al-based alloys Database version 2 is a thermodynamic database for the calculation of phase equilibria in multicomponent aluminum systems. The database contains a 34-element framework with 401 defined phases. The database was developed using 168 binary, 62 ternary, and 12 quaternary aluminum systems. This database is primarily used as a baseline for comparison between Thermo-Calc simulations and equilibrium experiments. The phases of interest are the `FCC_L12#1` for the α-Al matrix, `Q_ALCUMGSI` for the Q-phase, `AL2CU_C16` for the θ-phase, and `MG2SI_C1` for the β-phase. The database uses a stoichiometric compound description for the Q-phase with a composition of $Al_5Cu_2Mg_8Si_6$. The database does not include separate descriptions for the metastable θ' and β'-phase precursors.

QTDB The QuesTek aluminum Database is a modifiable proprietary thermodynamic database developed by QuesTek LLC. This database was originally similar to that of TCAL2 but is specifically used for the ability to be modified with experimental results acquired through this project. Details on the modifications resulting from this research will be discussed in detail in Chapter 3.

2.1.3 First-principles Calculations

First-principles calculations based on Density Functional Theory (DFT) have been successfully employed to provide key information about energetics, kinetics, diffusion and phase stability in alloy systems [8, 17, 50, 51, 52, 53, 54]. DFT calculations have been performed by Kyoungdoc Kim of the Wolverton/Voorhees groups at Northwestern as part of the overall GM-NU-QuesTek project. DFT calculations are performed for defect properties, solute partitioning, and interfacial structure of the equilibrium Q-phase $Al_3Cu_2Mg_9Si_7$. Defect formation energies are explored to understand off stoichiometric compositions of the Q-phase as identified by experimental results and is discussed in Chapter 3. Solute partitioning is explored to consider and recommend minor elemental additions to make the Q-phase energetically more stable and is discussed in Chapter 6.

First-principles DFT calculations are performed using the Vienna Ab initio Simulation

Package (VASP) [55, 56] and projector-augmented wave potentials [57]. The Perdew-Burke-Ernzerhof (PBE) parameterization of the generalized gradient approximation (GGA-PBE) [58] was used for all calculations. All structures were relaxed with respect to all cell-internal and cell-external degrees of freedom at an energy cutoff of 450 eV (520 eV is used for formation energy calculations) and k-point meshes were used to achieve at least 9,000 k-points per reciprocal atom. Formation energy is sufficient to converge energy difference to within 1 meV/atom. Further details of individual calculations will be given in their respective chapters.

2.1.4 Machine Learning

Machine learning has been used in materials science to build predictive models for a variety of applications, including melting temperatures of binary inorganic compounds [59], crystal structure predicitions [60] and mechanical properties of metal alloys [61]. The machine learning software package MAGPIE [62] (`bitbucket.org/wolverton/magpie`) developed by Logan Ward is used to create a predictive model for the growth/coarsening kinetics of θ' plate shaped precipitates over a range of aluminum alloy systems. A set of attributes was chosen to uniquely define each data point of the assembled particle size data set that is relatable to the physics that influences coarsening. The attributes selected include: aging time, aging temperature, and bulk alloy composition in at.% (aluminum content is dependent on the alloying additions and was not needed). Both the diameter and thickness of the plates was modeled independently. Further details of the ML modeling, such as attribute expanders and selection, can be found in Chapter 4.

2.2 Experimental Methods

Advanced analytical experimental techniques are required to observe and quantify the microstructure and mechanical properties of materials. Experiment is necessary to create and calibrate computational models such that the iterative computational design process can be improved. This research primarily utilizes 3-D atom probe tomography (3DAPT) to accurately measure various compositions within the micro-structure and measure particle sizes on the nanometer scale. Transmission electron microscopy (TEM) is used to observe a larger area of the microstructure than 3DAPT experiments are capable, and is used to identify and measure precipitate phases. Scanning electron microscopy (SEM) is used to a lesser extent due to the lower resolution and large interaction volume of analytical energy dispersive spectroscopy (EDS) capabilities, but is helpful at looking at a large scale view of the alloy, compared to 3DAPT or TEM. In addition to microstructural characterization techniques, it is necessary to acquire the alloy mechanical properties of interest. To obtain strength properties both microhardness and tensile testing of the various prototype alloys has been performed.

2.2.1 Alloy Design and Castings

As part of the overall project, prototype alloys were designed and cast for characterization. Prototype design was primarily carried out by QuesTek using the QTDB. The designs were created by specifying an amount of precipitate phases desired at the aging temperature of interest. Designs were made to achieve the desired phase fractions utilizing a "tieline" approach. Starting with a base alloy, the FCC α-Al matrix equilibrium composition and precipitate phase compositions are calculated in Thermo-Calc. Then using the law of mixtures, a new bulk composition is back-calculated for a specified amount of precipitate phases. With this new bulk composition a "step diagram" (phase fraction vs. temperature) and Scheil simulation are generated to observe which phases are at equilibrium at a range of temperatures and determine the solidus temperature. Through this process the desired solutionizing window, necessary for optimal precipitation strengthening, and eutectic fraction are varied for the alloy desired.

Casting of various alloys was performed at the GM Warren Technical Center foundry. Two types of castings were produced: small lab-scale button castings and lab-scale plate castings. The lab-scale button casts are made using a copper mold that produce flat circular buttons approximately $30\ mm$ in diameter and $6\ mm$ thick. Lab-scale plate castings are end-chill sand cast on a copper block, with final plate dimensions of $2'' \times 6'' \times 6''$. Bulk alloy compositions were obtained for all alloys cast by GM using spark atomic optical emission spectroscopy (OES). In addition to the GM castings, several specimens were prepared at QuesTek. These samples were melted in a Saturn induction furnace and cast into $200\ g$ plates in an open air-cooled graphite crucible approximately $6.5'' \times 3.75'' \times 1.0''$. Bulk alloy compositions were obtained from QuesTek castings using inductively coupled plasma optical emission spectroscopy (ICP-OES).

All samples underwent a homogenization/solution heat treatment at $490 - 530$ °C for 5 hrs, unless previously hot-rolled in which they were aged for 1 hr. Homogenization temperature was determined using Thermo-Calc Scheil solidification model simulations to determine the minimum temperature that liquid could form and thus prevent incipient melting. All samples were water quenched immediately after removal from the furnace.

2.2.2 Microhardness Testing

Microhardness testing is a fast method for measuring a material's resistance to plastic deformation, and can also be used to determine YS since hardness and YS are directly related. Microhardness measurements performed at Northwestern were made using a Struers Duramin 5 Vickers diamond indenter with a $200\ g$ load and $10s$ dwell time. All samples were polished to a minimum of $1\ \mu m$ diamond paste polish before indentation. A minimum of ten measurements were made for each specimen. Measurements were recorded using the Duramin software to automatically measure the diagonal lengths of each indent. Vickers hardness number, HV, is recorded as kgf/mm^2 from the equation:

$$HV = \frac{2F \sin{(136^\circ/2)}}{d^2} \tag{2.1}$$

where F is the load applied and d is the average indentation diagonal length. A simple empirical regression formula relating hardness (in HV) to yield strength (in MPa) in aluminum alloys has been developed by Grong and has been shown to work for Al-Mg-Si alloys [63, 64]. The simple regression model has been shown to work well for samples produced in this research in which both microhardness and tensile tests have been performed. The regression model is given in Equation 2.2.

$$HV = (1/3)\sigma_y + 16.0 \tag{2.2}$$

Similar Vickers microhardness measurements were performed at GM and QuesTek.

2.2.3 Tensile Testing

Uniaxial tensile testing was performed by GM. Tensile specimens were made from the end-chill sand cast plates. Each plate was divided into fine, medium, and coarse secondary dentrite arm spacing (SDAS) regions depending on their distance from the chill plate. This was done to observe the effects of the dendrite microstructure on UTS, YS, and elongation. Each cut plate section was heat-treated to peak age (200°C for 5 hrs). Tensile bars were then machined from the cut sections. The sample geometry is shown in Figure 2.1. Prior to tensile testing, each sample was conditioned for 200 hrs at the testing temperature, ranging from room temperature to 300°C. After conditioning samples were test at temperature. Testing was done on a Instron 5568CH235H machine at a strain rate of $1.00\ \%/min$. A minimum of 3 samples were test for each temperature and SDAS.

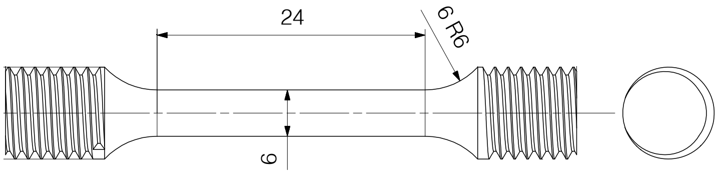

Figure 2.1: Geometry of tensile specimens. All dimensions are in millimeters.

2.2.4 Scanning Electron Microscopy

Scanning electron microscopy (SEM) was performed to analyze microstructure at high magnifications and measure composition using energy dispersive spectroscopy (EDS). Eutectic Si microstructure and phases that occur during the solidification process are observed. Homogenization treatments are also verified by the dissolution of these primary precipitate phases. SEM work was performed at Northwestern University's Atomic and Nanoscale

Characterization Experimental Center's (NUANCE) Electron Probe Instrumentation Center (EPIC) using a Hitachi S3400N-II SEM microscope and at GM using a Zeiss EVO 50. SEM samples are prepared by polishing to a $1\ \mu m$ diamond paste polish with an additional $0.05\ \mu m$ alumina slurry or colloidal silica polish. Samples were attached to a metal sample holder using double sided carbon tape (if mounted in an acrylic puck) or screwed down (if on an SEM stub) with either additional carbon or copper tape being used to connect the sample to the metal holder to provide a conductive path. Images were taken in both secondary electron (SE) and backscatter electron (BSE) mode.

2.2.5 Transmission Electron Microscopy

Transmission Electron Microscopy (TEM) was performed to identify precipitate phases and measure particle morphology. TEM work was performed at Northwestern's NUANCE EPIC Center using a Hitachi HT-7700 Biological S/TEM, Hitachi HD-2300A Dual EDS Cryo S/TEM, and JEOL JEM-2100F FasTEM microscopes. TEM work was also performed at the GM Technical Center in Warren, MI using a JEOL 2100F aberration-corrected S/TEM. The HT-7700 microscope is a 120 kV instrument primarily utilized for it's large specimen tilt ($\pm\ 45°$) pole piece and $0.2\ nm$ resolution capabilities. The HD-2300 dedicated STEM is a 200 kV instrument capable of SE SEM imaging and bright-field (BF), annular dark field (ADF) and high-angle annular dark field (HAADF) TEM imaging modes. This instrument benefits from ultra-sensitive dual-EDS capabilities and has a large specimen tilt ($\pm\ 45°$) pole piece. The JEOL JEM-2100F FasTEM is a 200 kV instrument with $0.1\ nm$ resolution in HRTEM mode with a HAADF STEM detector, Oxford EDS system, and Gatan GIF system for atomic resolution Z-contrast imaging capable of sub-nanoscale resolution EDS and EELS point analysis. This instrument has a limited specimen tilt (± $\sim 15°$) pole piece. The GM JEOL 2100F is similar to the NU JEOL instrument, but is aberration corrected for HRTEM imaging outside of STEM mode and has a larger specimen tilt (± $45°$) pole piece. The two JEOL instruments were also used in this research with a Gatan double-tilt heating stage capable of reaching $800°$C for the purpose of performing *in-situ* heating experiments.

TEM specimens were prepared from thin-slices or "foils" of cut material approximately $0.4\ mm$ thick, and a flat surface of $\sim 10\ mm$ x $\sim 10\ mm$. These thin-foils were then thinned to $\sim 100 - 200\ \mu m$ in thickness and polished to a $1\ \mu m$ diamond paste polish on both sides. $3\ mm$ disks were then punched from the polished foils. The discs were then twin-jet electropolished using a Tenupol 5 with a solution of 33% nitric acid and 67% methanol at $-15°$C to $-25°$C with an applied 14 V.

Particle sizes were determined from TEM images taken down either the $\langle 100 \rangle$, $\langle 110 \rangle$, or $\langle 111 \rangle$ zone axis of the α-Al matrix. Given the unique orientation relationships for the Q-, θ'-, and β'-phases, both the measured rod lengths and plate diameters must be adjusted according to the tilt direction. Images taken down the $\langle 110 \rangle$ α-Al zone axis contain particles $45°$ out of the imaging plane due to the [100] and [010] growth directions of the rod lengths and plate diameters. The measured values for these two directions should be multiplied by a factor of $\sqrt{2}$. Those particles growing in the [001] direction need no modification because they lie in the image plane. For images taken down the $\langle 111 \rangle$ α-Al zone axis, the $\langle 100 \rangle$ particles lie approximately $35.264°$ out of the imaging plane (the angle between the [111] plane normal and $\langle 100 \rangle$ is $54.736°$). The measured values must therefore be multipled by a factor of $1/cos(35.264°) \approx 1.225$.

2.2.6 Atom Probe Tomography

3-D Atom probe tomography (3DAPT) was performed using laser-pulsing mode local electrode atom probe tomography (LEAP) [65, 66] on a LEAP-4000XSi (Cameca, Madison, WI) at the Northwestern University Center for Atom-Probe Tomography (NUCAPT). 3DAPT allows for the atom by atom reconstruction of a sample for highly accurate and spatially resolved structural and chemical analysis. This research uses 3DAPT to determine precipitate compositions, precipitate sizes, matrix composition, and phase fractions for the prototype alloys.

The atom probe operates by applying an electric field to an atomically sharp tip. Field ionization of the surface atoms of the tip is caused by either voltage or laser (temperature) pulsing [67]. The voltage or laser pulse causes the atoms to evaporate from the surface and hit a detector. In this way individual pulses and ion detection are correlated, allowing for time-of-flight measurements to provide the mass/charge ratio of each ion and their identity [68]. Mass/charge spectrum assignment and ranging must be done appropriately during analysis for accurate results. A schematic of the LEAP is shown in Figure 2.2 [69].

To produce APT needle-shaped samples less than fifty nanometers in diameter, rectangular prism samples are cut with square cross-sections of $400\ \mu m$ x $400\ \mu m$ and 8-10 mm long, using either an Accutom precision high speed saw or an IsoMet low speed saw with a diamond wafering blade. Only those samples with the most square cross-section are selected for further processing; this is necessary to obtain good tip shape. The samples are then prepared into atomically-sharp needles by vertical electropolishing. Samples are first electropolished in a 10% perchloric acid in 90% acetic acid solution with a continuously applied voltage of $\sim 15-20$ V. The meniscus of the solution is used to preferentially remove material to produce a "neck". Once the "neck" is deemed thin-enough compared to

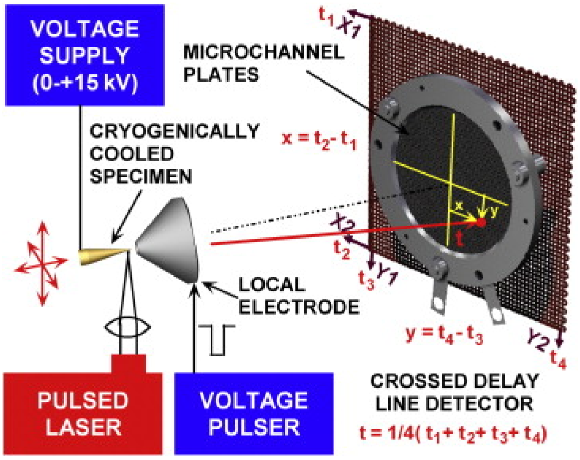

Figure 2.2: Schematic of the local electrode atom probe microscope [69].

the original thickness (typically $\sim 1/5$) the sample is cleaned in ethanol and the solution is changed. To separate the "neck" and produce the final needle shape a solution of 2% perchloric acid in 98% butoxyethanol is used with a pulsed voltage of 8-10 V. The sample is then immediately cleaned with ethanol. Ideally the sample is immediately loaded into the LEAP, and pumped down to ultra high vacuum ($< 10^{-8}$ torr) to prevent the formation of oxides on the sample, though this is less of a concern for aluminum samples.

Due to the unique electropolishing behavior needed to prepare APT samples, only the low Si containing wrought alloys could be prepared using the vertical electropolishing method. This is due to the Si eutectic component in the high Si cast alloys that remains unaffected during the electropolishing process [31]. To prepare the cast alloys for APT, site-specific dual-beam focused-ion beam (FIB) machining was used on polished samples. The polished samples used in the FIB process were $\sim 6\ mm \times \sim 6\ mm\ \times (0.5 - 1\ mm)$ polished to at minimum a $1\ \mu m$ diamond paste polish. A dual-beam FEI Helios FIB microscope with an Omniprobe micromanipulator, located in the EPIC center, was utilized for material lift-out using a technique developed by Thompson et al. for the rapid preparation for APT samples [70]. The Si eutectic particles were avoided during this lift-out to provide samples of primarily dendritic aluminum matrix. An array of pre-fabricated Si microposts was used as a substrate onto which the APT specimens were mounted. An ion beam of 30 kV was used in all milling steps with a post-sharpening step using a 5 kV ion-beam for Ga damage "cleanup". Figure 2.3 demonstrates what the FIB process looks like during mounting and after sharpening of the tip.

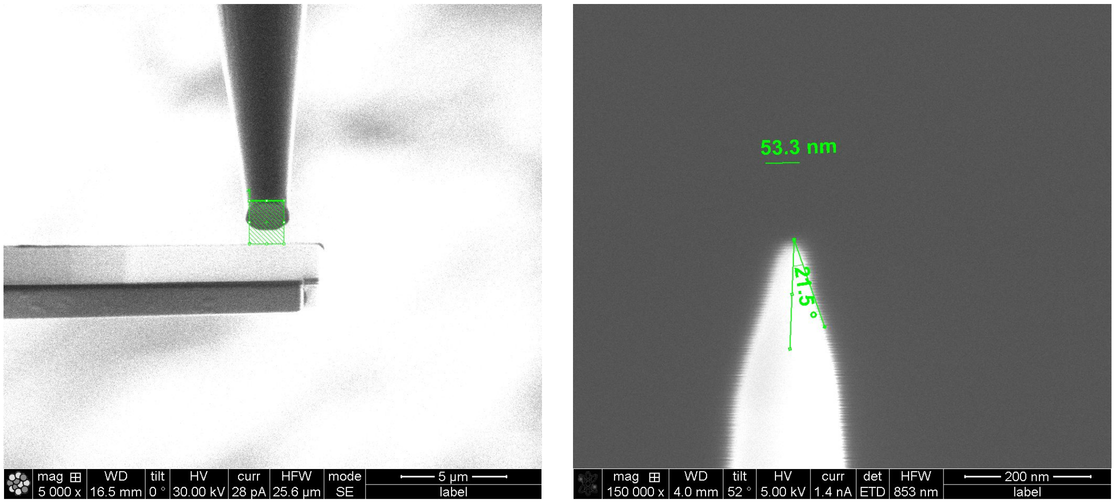

(a) (b)

Figure 2.3: FIB process showing the (a) mounting of lift-out material onto a Si post, and (b) a sharpened tip

All APT samples were run in laser pulsing mode at temperatures between 30-50 K, picosecond laser pulse energy of 40-50 pJ per pulse, at a rate of 500 kHz, and an evaporation rate of $0.5 - 5\%$ depending on the quality of the tip. Higher initial laser pulse energies 80-100 pJ) were used during alignment to quickly find the tip at lower voltages, thus reducing the chances of tip fracture during initial alignment. Successful LEAP runs acquired between 20 and 90 million atoms. Data sets were analyzed using the IVAS 3.6 (Cameca) reconstruction software. The interface between two phases was determined using an isoconcentration surface were the interface concentration was determined such that it enclosed a 2-D concentration profile of the strongest partitioning elements perpendicular to the primary particle growth direction. Once the interfaces are generated, the proximity histogram method (proxigram) [71, 72] was used to analyze the composition of the precipitate phases vs. distance from the isoconcentration surface chosen, this can be performed over a single interface of over an average of interface. This work primarily utilized longer aged samples, providing larger precipitates. This allows for the mitigation of matrix/precipitate overlap concerns that is easily identifiable in smaller precipitate analysis and can lead to misleading composition assessments [9]. The larger precipitate sizes allow for the use of the plateau method [73] in determining the chemical composition of the precipitates. Concentrations are achieved by averaging over the flat 2-D profile within the isoconcentration surface and internal from the diffuse interface observed due to the overlap effect. The rod-type particle radius and plate-type thickness measurements were obtained from the 2-D concentration profiles of the strongest partitioning elements used to define the isoconcentrations. Typically the rod lengths and plate diameters were too large to be contained within the APT reconstruction and be measurable.

Alloy matrix compositions were determined from the APT reconstructions via precipitate extraction. Isoconcentration surfaces were generated at lower concentrations than those defined previously such that they enclosed the precipitates and some of their surrounding interface. A new reconstruction was then created with all particles removed. This new reconstruction therefore only included the α-Al matrix, and the total bulk composition is the matrix composition. In this way a larger sample volume is utilized in determining matrix composition than the proxigram method used for precipitates, which does include some matrix but only that directly surrounding the defined surface.

The phase fraction of all precipitate phases and matrix is calculated by application of a multi-dimensional adaptation of the lever rule. The method developed in this research is solved numerically and is easily expandable for an infinite number of alloy components and phases. Knowledge of the phases present, the phase compositions, and the bulk alloy composition is necessary. The mathematical basis for this calculation is represented in the linear program:

$$\begin{aligned} \text{minimize:} \quad & f(x) = 1 - \sum_{j=1}^{n} \phi_j \\ \text{subject to:} \quad & \sum_{j=1}^{n} X_j^i \phi_j \leq X_{Bulk}^i, \; i = 1, \ldots, m \\ & 0 \leq \phi_j \leq 1, \qquad\quad j = 1, \ldots, n \end{aligned}$$

were ϕ_j is the phase fraction for phase j (including the matrix) and X_j^i is the composition of element i in phase j. This linear program solves for n phase fractions in an m component alloy, such that they sum up to 100%, the total amount of element i approaches that of the bulk composition of i, and is constrained such that each phase fraction must be between 0% and 100%. Solving of the linear program was performed in MATLAB for each alloy with measured matrix, precipitate, and bulk compositions.

3 Q-Phase Precipitation in Aluminum Alloys

3.1 Background

The Al-Si-Mg-(Cu) alloy system is widely used in the automotive and aircraft industries due to their significant precipitation strengthened age hardening behavior. Knowledge of the compositional and phase stability of precipitation strengthening phases that occur in these systems is essential for understanding and predicting mechanical properties. The structure, morphology, and composition of these precipitate phases are a common discussion topic in modern literature, but confusion still exists concerning the quaternary Q-phase. 3-D atom probe tomography (3DAPT) measurements of chemical composition on the nanometer sized rod shaped precipitates found in these aluminum alloys allows for the compositional distinction between these phases which have traditionally been characterized via TEM techniques.

Recent studies on the β-phase in the Al-Si-Mg Cu-free system using high-resolution TEM (HRTEM) imaging have shown that there exists a series of intermediate phases occurring upon further aging after the precipitation of the β"-phase. These phases include the traditional β'-phase and three additional intermediate phases labeled U1, U2, and B', also commonly identified as type A, B, and C respectively, with different crystal structures and composition [74, 75]. The currently accepted precipitation sequence for this Cu-free system has been found to be [5, 76, 77]:

$$SSSS \rightarrow atomic\,clusters \rightarrow GP\,zones \rightarrow \beta\text{"} \rightarrow \beta', U1, U2, B' \rightarrow \beta, Si$$

All of these precipitate phases, except for β and Si, exhibit a rod-like morphology and grow along the $\langle 100 \rangle$ directions of the Al matrix. An overview of these Cu-free phases and the Q-phase is given in Table 3.1. It should be noted that the Al containing $Mg_5Al_2Si_4$ β"-phase composition, which has been supported by APT and DFT calculations [9, 10], is a recent departure from the classical Al free composition much like the U1, U2, and B' variants of the β'-phase.

Table 3.1: Precipitate phases found in the Cu-free Al-Mg-Si system and the Q-phase.

Phase	Composition	Space Group	Bravais	Lattice Parameters (nm)
β"	Mg_5Si_6, $Mg_5Al_2Si_4$	C2/m	Mono.	a=1.516, b=0.405, c=0.674, β=105.3° [9, 10, 11, 12]
β'	Mg_9Si_5	$P6_3$	Hex.	a=b=0.715, c=0.405, γ=120° [13, 14]
U1	$MgAl_2Si_2$	$P\bar{3}m1$	Trig.	a=b=0.405, c=0.674, γ=120° [13, 78, 79]
U2	MgAlSi	Pnma	Ortho.	a=0.675, b=0.405, c=0.794 [13, 78, 80]
B'	$Mg_9Al_3Si_7$	Hex.	Hex.	a=b=1.04, c=0.405, γ=120° [13, 81]
β	Mg_2Si	$Fm\bar{3}m$	Cubic	a=0.635 [13, 25]
Q	$Mg_9Al_3Si_7Cu_2$, $Mg_8Al_5Si_6Cu_2$	$P\bar{6}$	Hex.	a=b=1.039, c=0.402, γ=120° [17, 18, 19]

The similarity of these phases, in particular the B' (type C) phase, to the Q-phase has made the topic very controversial. In addition, atomistic analysis of various rod shaped precipitates using high angle annular dark field scanning TEM (HAADF-STEM) have identified a hexagonal "Si network" present within all the Cu containing and Cu- free rod cross-sections, except for the monoclinic β"-phase [5, 76, 82]. Before the 1980s there was no evidence of the precipitation of the Q-phase upon aging in the Al-Si-Mg-Cu system, with studies showing metastable versions of β-phase in the current phase region of Q-phase formation.

Similarities between the β'-phases and the Q-phase are the cause of much confusion. In particular, the B' (type C) phase differs only in the composition from the Q-phase, having the same structure and nearly identical hexagonal lattice parameters a=1.035-1.040 nm and c=0.402-0.405 nm [13, 17, 18, 81, 83]. The morphology and crystal lattice constants alone are unable to uniquely identify these phases, therefore requiring accurate compositional analysis or the use of atomic resolution microscopy and image simulation [84]. Often in archival literature the rod-type precipitates are distinguished via their cross-sectional morphology which as will be demonstrated is not valid, often leading to the misidentification of the Q-phase as β'. The nanometer-sized scale of the rod-shaped precipitate cross-sections, typically reported in the range of 3.0-12.0 nm^2 [18], makes analytical electron microscopy techniques prone to high uncertainty. For example, the probe diameter of energy dispersive X-ray spectroscopy (EDS) is on the same order of magnitude as the particle cross-sections. This probe size leads to large overlap between the phase of interest and the FCC aluminum matrix making the Al concentration unquantifiable. Modern-day 3DAPT does not exhibit this problem due to its atomistic nature and makes it the most appropriate technique for the compositional analysis of nanometer scale precipitates. To date, the only published studies of Q-phase precipitation using 3DAPT have been performed on 319 series aluminum alloys [31, 85] and 6xxx type alloys [86].

In this work 3DAPT has been performed on a number of both wrought and cast aluminum alloys with varying Cu contents to obtain an accurate compositional assessment of both the Q, β, and metastable β'/β" precursors. TEM was used to confirm the morphology of these phases and identify phases with low number density. From these investigations we identify varying Q-phase compositions with changes in Mg and Cu content. We then propose the existence of a Cu:Mg sub-lattice within the Q-phase structure that accounts for the observed solubility within the Q-phase, but is disfavored energetically in DFT estimates. A re-assessment of the ThermoCalc QTDB database is performed with an updated Q-phase compositional description based on the experimental APT results. The updated database is compared with the commercial TCAL2 database and experimental results.

3.2 Methodology

3.2.1 Experimental Methods

A series of six wrought (less than 2 wt.% Si) and four cast (greater than 5 wt.% Si for eutectic solidification) alloys were investigated. Two additional alloys (HQHCu and HQLCu) were designed and cast by QuesTek, upon the author's request, to assess the QTDB database at high Mg contents. The composition for these two alloys are not given. Table 3.2 shows the bulk alloy chemical compositions obtained using spark atomic emission spectroscopy (OES) along with the homogenization treatments used, arranged with cast to wrought alloys from low to high Cu contents. All alloys were homogenized for 5 hrs (or 1 hr if previously hot-rolled) at either 490°C or 530°C, depending on Cu content to prevent incipient melting. For the GMQ2 sample a 2-step homogenization heat treatment of 490°C for 6 hrs followed by 550°C for 16 hrs was used. All samples were water quenched after homogenization heat treatment. Samples were then aged at 200°C for 24, 72, and 1000 hrs to achieve near equilibrium conditions.

Table 3.2: Bulk alloy chemical compositions as determined by OES.

Alloy	Si (wt.%)	Mg (wt.%)	Cu (wt.%)	SHT (°C/hours)	Age Time
356	6.59	0.41	0	530/5	1000
CM	7.50	0.56	0.13	530/5	1000
CQ	5.90	0.49	0.81	530/5	72
CTQ	5.30	0.27	3.16	490/5	72
WQ	0.74	0.49	0.75	HR+530/1	72
WTQ3	1.00	0.31	0.89	490/5	1000
GMQ2	0.81	0.63	1.07	490/6+550/16	1000
WTQ2	1.18	0.29	1.44	490/5	1000
WTQ1	1.02	0.25	2.24	490/5	24
WTQ	1.20	0.35	3.10	HR+490/1	72

APT wire specimens and FIB samples were prepared as discussed in Section 2.2.6 for the wrought and cast alloys, respectively. APT was performed in LEAP mode and analyzed using IVAS 3.6, see Section 2.2.6 for details. The isoconcentration surface (iso-surface) used to define the Al-matrix/(Q & β)-precipitate interface was determined via projected 2-D concentration profiles of Mg+Si content perpendicular to the primary particle growth direction. The surface was chosen such that it accurately enclosed the projected 2-D concentration profile. This typically corresponded to a 10-20 Mg+Si at.% concentration for long aging conditions. For samples containing θ'-phase (Al_2Cu), isoconcentration surfaces used to define the Al-matrix/θ'-phase was defined using Cu concentration between 5-7 at.%. TEM specimens were prepared by the electropolishing procedure discussed in Section 2.2.5. TEM images were obtained using the JEOL 2100F at GM and the HT7700 microscope at NU (see Section 2.2.5). SEM images and EDS analysis were performed at NU using the S3400N-II SEM (see Section 2.2.4).

3.2.2 Computational Methods

First-principles DFT calculations to explore the proposed Cu:Mg sub-lattice within the Q-phase structure were performed by Kyoungdoc Kim using VASP as discussed in Section 2.1.3. Formation energy is sufficient to converge energy differences within 1 meV/atom. Formation enthalpies of the Q-phase off stoichiometric compounds were calculated based on the following equation:

$$\Delta H^{eq}(A_aB_bC_cD_d) = E(A_aB_bC_cD_d) - [x_AE^{eq}(A) + x_BE^{eq}(B) + x_CE^{eq}(C) + x_DE^{eq}(D)]$$

where the equilibrium formation enthalpy $\Delta H^{eq}(A_aB_bC_cD_d)$ (eV/atom), for any quaternary compound $A_aB_bC_cD_d$ is given by the energy of $A_aB_bC_cD_d$ relative to the composition-weighted average of the energies of the pure constituents each in their equilibrium crystal structures. In the Arnberg $Al_4Cu_2Mg_8Si_7$ Q-phase unit-cell [18] used in this series of calculations, there are 21 atoms (a+b+c+d). $E(A_aB_bC_cD_d)$ is the energy per solute atom of the compound $A_aB_bC_cD_d$ relaxed to its equilibrium geometry. $E^{eq}(A)$, $E^{eq}(B)$, $E^{eq}(C)$, and $E^{eq}(D)$ are the energies of the constituents, A, B, C, and D, respectively, each relaxed to their equilibrium geometries. Here $x_A = a/(a+b+c+d)$, $x_B = b/(a+b+c+d)$, $x_C = c/(a+b+c+d)$, and $x_D = d/(a+b+c+d)$ are the molar concentrations of A, B, C, and D, respectively.

Native defect formation energy was also calculated to determine which likely vacancy and anti-site related to the observed off stoichiometric experimental compositions. The various phases in equilibrium were obtained using the grand canonical linear program (GCLP) method [87] to search for equilibrium phases in the quaternary Al-Cu-Mg-Si system using the OQMD. The chemical potentials are then calculated to determine the defect formation energies using the following equation:

$$\Delta H^f_{defect} = E_T - \sum_i n_i \mu_i$$

where E_T is the total ground state energy of the super cell plus defect as calculated, n_i are the number of elements i in the super cell, and μ_i is the chemical potential for that element. A $1 \times 2 \times 3$ super cell containing 126 atoms was used for the Q-phase to converge energy difference within 0.03 ev/atom.

Thermo-Calc equilibrium simulations are carried out using Thermo-Calc version 2016a with the TCAL2 and QTDB databases discussed in Section 2.1.2. Equilibrium calculations were performed for all alloys using the experimentally measured bulk composition from OES. Isotherm phase diagrams have been generated for the Al-rich corner of the phase diagram with set temperature, Si content, and varying Cu and Mg contents.

3.3 Results and Discussion

3.3.1 APT Precipitate Composition Analysis

APT was performed on all alloys listed in Table 3.2 aged for 24 hrs or longer at 200°C. The proxigram method was used to analyze the composition of the precipitate phases as a function of distance from the isoconcentration surface chosen (Section 2.2.6). The precipitate concentrations listed were obtained from the plateau method. The alloys are discussed based on the equilibrium precipitation phases present within the alloy system.

3.3.1.1 β'-Phase Containing Alloys

The 356 alloy was the only alloy observed to contain β'-phase precipitates. Long rod-shaped β'-phase precipitates are found in the 356 sample aged for 72 hrs at 200°C along with large Si particles. Figure 3.1(a) shows a 3-D reconstruction of this sample. Due to the presence of the Si particle (green 10 at.% Si iso-surface), the β' particles were outlined using a 10 at.% Mg (purple) iso-surface to isolate them from the Si particle. Ga atoms, which are introduced during the FIB process and segregate to dislocations and grain boundaries [88, 89], are shown in yellow and indicate dislocation interaction with the precipitates, suggesting dislocation-based heterogeneous nucleation.

The proxigram used to analyze the composition of the β'-phase is shown in Figure 3.1(b). The dashed vertical line represents a general location of the interface between the α-Al matrix and the β'-phase, with the spatial composition profile for the matrix being on the left and the β'-phase on the right. The average composition of the β'-phase precipitates is: 18.03 Al- 53.11 Mg- 28.85 Si at.%. This composition is in line with the B' (β'-phase Type C) precursor phase $Mg_9Al_3Si_7$ [13, 81] rather than the classical Al free β'-phase Mg_9Si_6 [13, 14]. The experimentally measured β'-phase composition is richer in Mg than the DFT determined compound stoichiometry. Presence of the B'-phase in Cu free 356 is similar to what has been reported by Edwards et al. for the Al-Mg-Si 6061 alloy. In 6061 it was determined that upon aging at 200°C the predominant rod-shaped precipitate phase was the B'-phase [90].

Upon further aging of the 356 sample at 200°C to 1000 hrs, a transition from the β'-type rods to more plate/cuboidal β-phase is observed. As shown in the 3-D reconstruction in Figure 3.1(c), a large particle of β-phase (purple 25 at.% Mg surface) can be seen connected to Si particles (green 60 at.% surface). The composition of this particle was found

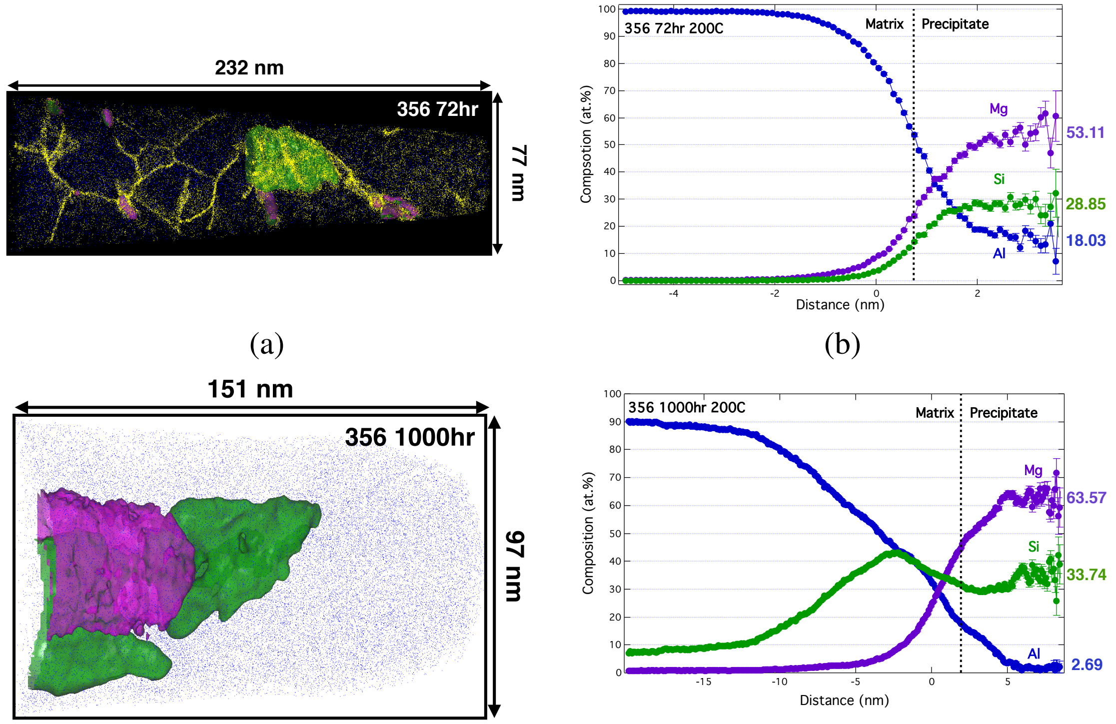

(a) (b)

(c) (d)

Figure 3.1: (a) 3-D reconstruction of a sample of 356 aged for 72 hrs at 200°C. Si iso-surface is shown in green while the Mg iso-surface is shown in purple. (b) Proxigram of the β'-phase particles found in (a). (c) 3-D reconstruction of a sample of 356 aged for 1000 hrs at 200°C. Mg and Si iso-surface colors are as in (a). (d) Proxigram of β-phase particle found in (c).

to be 2.69 Al- 63.57 Mg- 33.74 Si at.% and is effectively the accepted Mg_2Si stoichiometry [13, 25] with some dissolved Al, see Figure 3.1(d).

3.3.1.2 Q-Phase Containing Alloys

Rod and lath-shaped Q-phase precipitates are present in the CM 1000 hr, WQ 72 hr, CQ 72 hr, and WTQ3 1000 hr samples, in order of increasing Cu content, all aged at 200°C. 3-D reconstruction of these tips can be seen in Figure 3.2, with Al atoms shown in blue and the chosen isoconcentration surface highlighting the Q-phase shown in purple. The following isoconcentration surfaces were used to highlight the Q-phase precipitates: for CM a 20 at.% Mg+Si surface, for WQ and WTQ3 a 10 at.% Mg+Si surface, and for CQ a 5 at.% Mg surface due to the fine Si particles present (7 at.% Si surface). The Q-phase compositions determined using the plateau proxigram method for this set of alloys is summarized in Table 3.3.

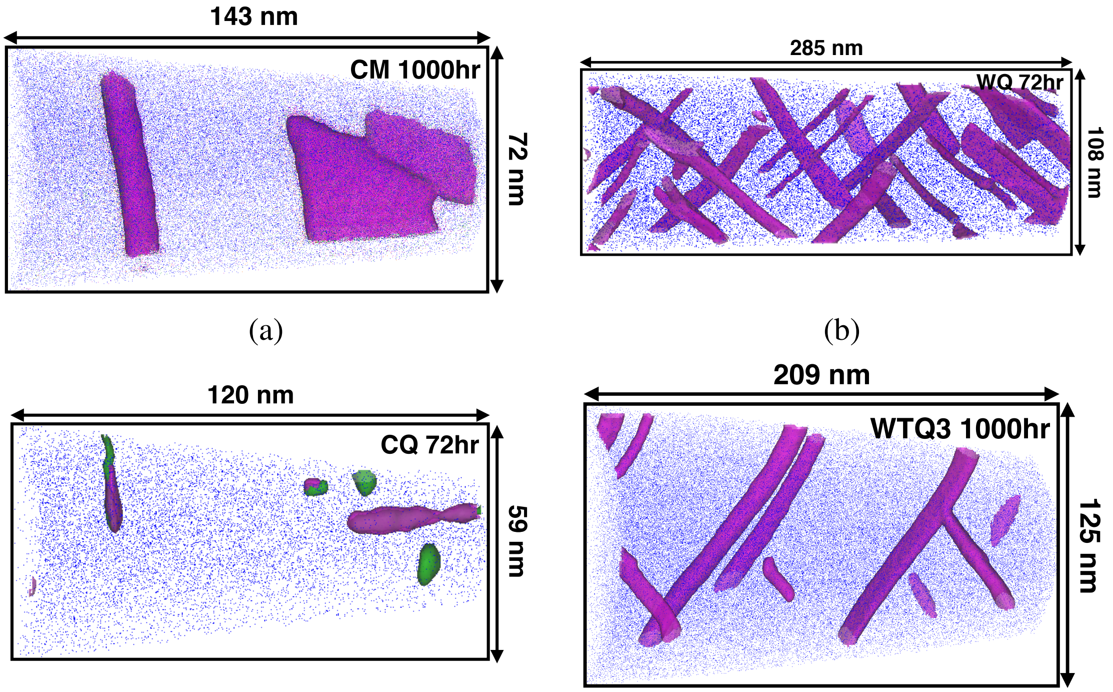

(a) (b)

(c) (d)

Figure 3.2: (a-d) 3-D reconstructions displaying Al atoms in blue, Mg+Si/Mg iso-surfaces in purple, and Si iso-surfaces in green for (a) CM 1000 hr, (b) WQ 72 hr, (c) CQ 72 hr, and (d) WTQ3 1000 hr. All samples were aged at 200°C.

It should be noted that there is no compositional difference between the rod and lath shaped Q-phase precipitates. Take for example the CM 1000 hr 200°C sample that includes both prominently. Both the rod-type and lath-type compositions have been analyzed using

Table 3.3: Near equilibrium Q-phase compositions for alloys aged at 200°C.

Alloy	Aging Time (hrs)	Al (at.%)	Si (at.%)	Mg (at.%)	Cu (at.%)
CM	1000	20.14	29.00	46.14	4.72
WQ	72	21.96	25.34	41.18	11.52
CQ	72	24.06	26.72	39.2	10.01
WTQ3	1000	19.62	26.53	41.97	11.88

the proxigram method using the individual isoconcentration surfaces, and are illustrated in Figure 3.3. As can be seen, the composition of each are nearly identical and tabulated in Table 3.4. Cross-sectional morphology alone should therefore not be used as a means to distinguish between the various rod-shaped precipitates, such as the Cu-free β' and Cu-containing Q-phases.

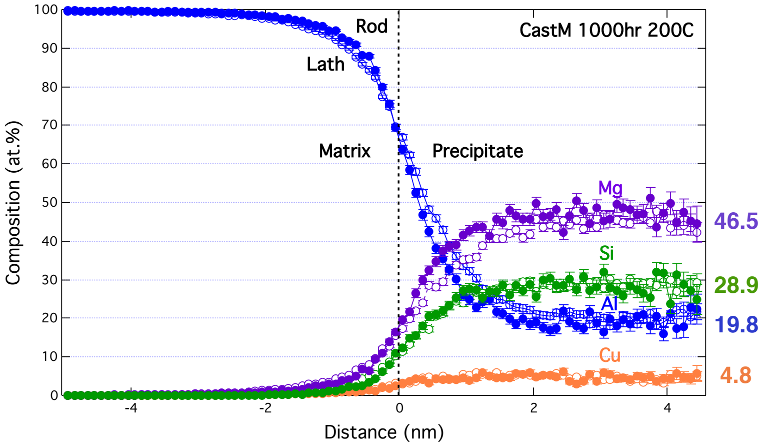

Figure 3.3: Proxigram from a sample of CM aged at 200°C for 1000 hrs. Rod-type precipitate compositions are shown in solid circles while the lath-type precipitate compositions are shown in open circles.

This bifurcation in Q-phase shape could possibly be due to variation in the local lattice geometries or disordering of Cu atoms in the Q-phase lattice. This would imply different

Table 3.4: Q-phase compositions for both rod- and lath-type precipitates in the CM 1000 hr 200°C sample.

Type	Al (at.%)	Si (at.%)	Mg (at.%)	Cu (at.%)
Rod	18.98	28.69	47.41	4.91
Lath	20.54	29.12	45.64	4.71

crystal structures and various Q-phase variants much like the β' variants, expect here the composition remains the same. High-resolution annular dark field TEM/STEM studies performed by Cayron, Ehlers, and Marioara [5, 76, 77, 83] have previously highlighted the influence on the Cu local-geometries in distinguishing Q-phase variations, i.e. the Q, L, C, QP and QC-phases. These variants tend to have different cross-section morphologies with slightly varying habit planes. The variant crystal lattices exhibit a hexagonal base lattice of Si atoms, with subunit triangular clusters, with the continuous transformation between the variants corresponding to ordering of these clusters. An exception to this being the disordered L variant, which exhibits the hexagonal Si network but disordering of other elements around it. A schematic representation, from [5] is shown demonstrating the transformation between the C- and Q-phases in Figure 3.4.

This schematic representation highlights the underlying network of Si atoms (large spheres) that relates the two crystal structures. These Si network columns extend down the c-axis and thus run along the length of the rod morphology. The smaller spheres are "non-network" atoms and correspond to either Al, Mg, or Cu. Different Cu-ordering as seen for the C and Q-phase precipitates and are highlighted by green lines. This same schematic representation of Si network atoms and non-network (Al, Mg, Cu) atoms is also applicable to the L, β', U2, and B' phases. This representation demonstrates the strong similarities between the Cu-free and Cu-containing phases. Though it is noted that no correlation

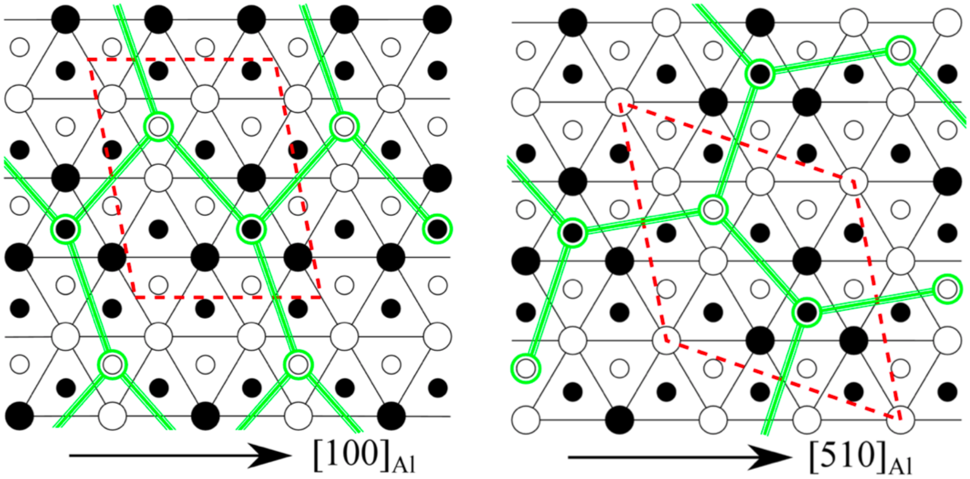

(a) (b)

Figure 3.4: Schematic representation of (a) the C-phase and (b) the Q-Phase [5]. Relative atom heights are highlighted by the color of the sphere: white = 0 Åand black = 2.025 Å. Si network atoms are the larger spheres and connected with solid lines. "Non-network" atoms are the smaller spheres being Al, Mg, or Cu. The Cu atom ordering has been highlighted with green lines. The dashed red lines are the unit cells. From [5].

between the Cu local-geometries and the cross-sectional morphology has been reported in literature and the composition of some of the Q-phase variants are still unknown.

3.3.1.3 Q and θ'-Phase Containing Alloys

In addition to Q-phase precipitation, θ'-phase plates are observed in APT samples of WTQ1 24 hr, WTQ 72 hr, and CTQ 72 hr, in order of increasing Cu content. The CTQ sample did not contain Q-phase rods due to the low number density, but have been identified using TEM (see section 3.3.2). On the other hand, APT samples of GMQ2 and WTQ2 aged for 1000 hrs at 200°C only contained Q-phase rods and did not include θ'-platelets due to their low number density, which again have been identified using TEM. 3-D reconstructions for these samples are shown in Figure 3.5. In these reconstructions Al atoms are shown in blue, the Mg+Si isoconcentration surface outlining the Q-phase is purple, and the Cu isoconcentration surface outlining the θ'-phase is orange. The isoconcentration surfaces used for the Q and θ'-phases and any Si particles in Figure 3.5 are: for GMQ2: 10 at.% Mg+Si; for WTQ2: 20 at.% Mg+Si; for WTQ1: 7 at.% Mg+Si and 7 at.% Cu; for WTQ: 5 at.% Mg+Si and 5 at.% Cu; and for CTQ: 9 at.% Mg+Si, 5 at.% Cu, and 45 at.% Si iso-surfaces.

The θ'-phase composition in these alloys was found to be the expected stoichiometric Al_2Cu compound as shown in the proxigram in Figure 3.6 from a sample of WTQ aged at 200°C for 72 hrs. The θ' composition found using the plateau method was 60.9 at.% Al- 34.2 at.% Cu- 2.7 at.% Mg- 2.2 at.% Si. The presence of dissolved Mg and Si inside the θ' plates is due to the presence of Q-phase rods embedded inside. The Q-phase composition of the CTQ alloy is not available due to the phase not being contained in the APT runs as stated previously. The Q-phase compositions for alloys GMQ2, WTQ2, WTQ1, and WTQ are summarized in Table 3.5. The Q-phase composition in these alloys in the presence of θ'-phase is near constant even though the bulk Cu composition in these alloys varies from 1.07-3.10 wt.%, implying that the composition of the Q-phase is invariant beyond a certain bulk Cu level.

Table 3.5: Near equilibrium Q-phase compositions for alloys containing θ'-phase aged at 200°C.

Alloy	Aging Time (hrs)	Al (at.%)	Si (at.%)	Mg (at.%)	Cu (at.%)
GMQ2	1000	19.83	26.41	42.76	11.00
WTQ2	1000	17.76	27.71	43.04	11.50
WTQ1	24	21.07	25.83	40.87	12.22
WTQ	72	20.08	27.51	40.64	11.77

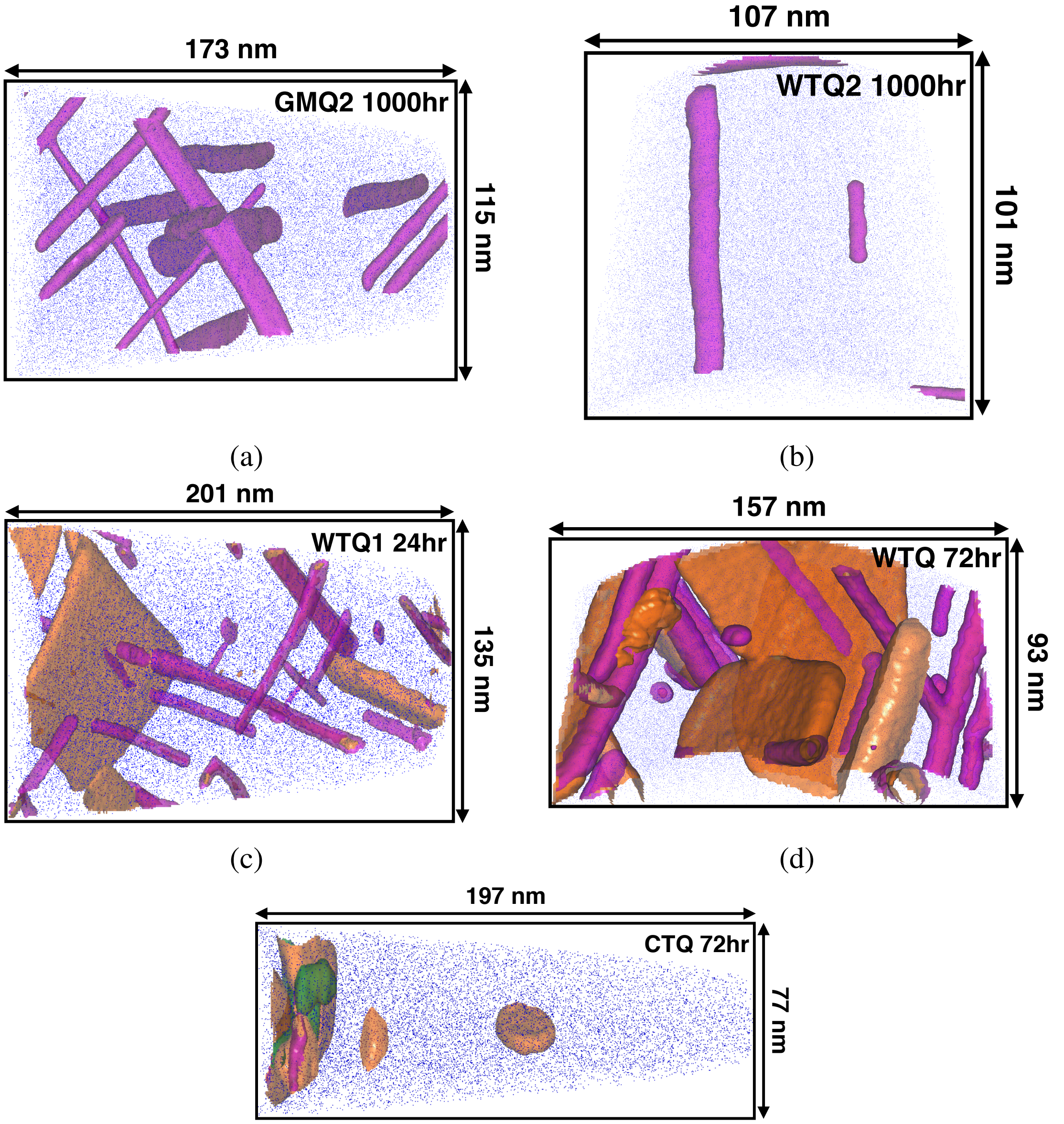

(a) (b) (c) (d) (e)

Figure 3.5: 3-D reconstructions for the Q and θ'-phase containing alloys aged at 200°C. Mg+Si/Mg iso-surfaces are shown in purple, Si iso-surfaces are shown in green , and Cu iso-surfaces are shown in orange. (a) GMQ2 aged for 1000 hrs, (b) WTQ2 aged for 1000 hrs, (c) WTQ1 aged for 24 hrs, (d) WTQ aged for 72 hrs, and (e) CTQ aged for 72 hrs.

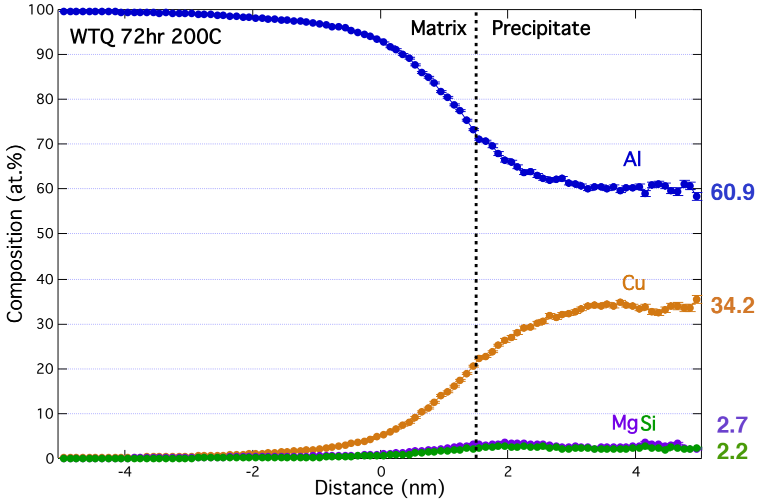

Figure 3.6: Proximity histogram of the θ'-phase plates from the sample of WTQ aged at 200°C for 72 hrs shown in Figure 3.5(d).

3.3.1.4 Q-phase Composition Variation

3DAPT analysis of the Q-phase precipitates in the ten alloys aged to near equilibrium conditions show a variety of compositions contrary to reported literature stoichiometries. Table 3.6 includes compositions of the Q-phase previously found in the literature. Our measured compositions containing high Cu content after aging at 200°C are similar to that of Phragmen's [19], though slightly leaner in Al and richer in Mg. Following Phragmen's experiment, the crystal structure of the Q-phase was solved by Arnberg and Aurivillius [18] using four-circle diffraction. When comparing the APT Q-phase compositions to Arnberg's stoichiometry, the Al content is the same, but the APT compositions are leaner in Si and richer in Mg and Cu.

An EDS study performed by Matsuda et al. [82] reported lower levels of Cu and higher levels of Si when compared with the Cu rich Q-phase measured by APT. This stoichiometry, however, is similar to that of the low Cu containing CM alloy, which demonstrated much lower levels of Cu solubility in the Q-phase. In our case the CM alloy Q-phase had higher levels of Mg while the Si content remained the same. Matsuda's alloy contained 0.5 wt.% Cu which is larger than the CM alloy bulk Cu content of 0.17 wt.%. Thus the relative Cu content measured in the Q-phase is in agreement with the trend in bulk Cu content of each alloy. Matsuda et al. suggested that this low Cu containing Q-phase was either a metastable Q'-phase or was the B'-phase with Cu. This study has found that the low Cu containing rod-shaped phase was indeed stable out to 1000 hrs of aging at 200°C, suggesting that it is stable Q-phase with no observed transformation to the β-phase as would be expected for the β'-phase or its variants. It is clear from our results that the equilibrium composition of the Q-phase is dependent on that of the matrix in which the precipitate forms.

Table 3.6: Chemical compositions of the Q-phase as reported in literature.

Study	Stoichiometry	Al (at.%)	Si (at.%)	Mg (at.%)	Cu (at.%)
Phragmen [19]	$Al_5Cu_2Mg_8Si_6$	23.8	28.57	38.09	9.52
Arnberg [18]	$Al_4Cu_2Mg_8Si_7$	19.04	33.33	38.09	9.52
Matsuda [82]	$Al_4Cu_1Mg_6Si_6$	23.5	35.3	35.3	5.9
Löffler [91]		16.8	29.8	44.3	9.1
Wolverton [17]	$Al_3Cu_2Mg_9Si_7$	14.28	33.33	42.85	9.52

A prior study performed by Löffler et al. [91] used plane front directional solidification techniques to produce bulk Q-phase. It is interesting to compare the macroscopic Q-phase composition with the nano-scaled precipitate rods. This bulk Q-phase composition is leaner in Al and slightly richer in Si and Mg than those of this study. Of note is that the Löffler study found no significant solubility range within the Q-phase, while the current study shows a large range of Cu content. This Cu variation may only be attainable in precipitate form. Additionally, first-principles calculations performed by Wolverton [17] have identified $Al_3Cu_2Mg_9Si_7$ as the most stable ground-state composition of the Q-phase. This stoichiometry, which has similar Mg and Cu content as our APT results, is leaner in Al and richer in Si, but overall very similar to that of the bulk Q-phase composition reported by Löffler.

The existence of solubility ranges within the Q-phase composition is evident over the set of alloys examined in this study. The Al and Si contents of the Q-phase remain fairly stable over the alloy composition range explored and regardless of the bulk Si content. The same cannot be said for the Mg and Cu amounts with regard to alloying content. In Figure 3.7 we compare the Mg, Cu, and Mg+Cu contents identified in the Q-phase and β'-phase precursor of alloy 356. We see that on average the Mg+Cu content is consistent across all explored alloy systems including the alloys that have very little to no Cu. This is evidence of a potential Cu:Mg sub-lattice within the Q-phase crystal structure. This sub-lattice would allow for Mg atom anti-site substitution on the Cu lattice sites, thus explaining the variation on the Cu content seen in the CM alloy and Matsuda et al. study. This sub-lattice also bridges the gap of the Q-phase with the Mg rich β'-phase type C precursor (B') seen in the 356 alloy if allowed to extend to zero Cu levels with additional Mg on the Cu sites as opposed to the Cu vacancies present in the DFT determined B' stoichiometry.

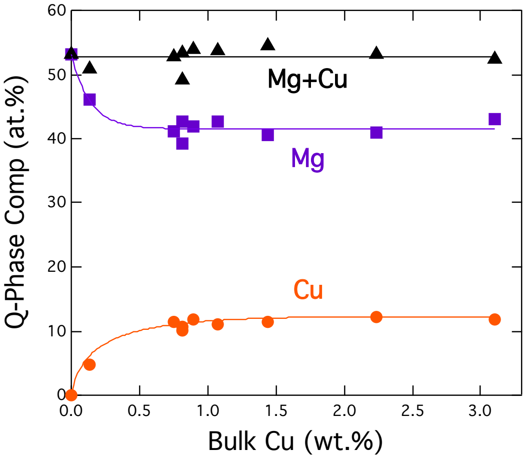

Figure 3.7: Measured Mg, Cu, and Mg+Cu concentrations of the Q-phase with varying bulk Cu content.

3.3.2 TEM Phase Identification

TEM analysis was undertaken to identify precipitate phases at equilibrium conditions that were potentially missed by the APT due to its small sampling volume, and to identify precursor phases at shorter aging times. TEM was used to identify precipitate phases in all alloys except for WTQ and WQ. The APT analysis for these alloys already contained all the expected phases.

TEM analysis of 356 alloy was performed on samples aged for 5 hrs, 72 hrs, and 1000 hrs at 200°C. The evolution of the β-phase and precursor precipitates can be seen in the high-resolution and bright-field micrographs in Figure 3.8. Analysis of the 5 hr aged sample showed rod-shaped precipitate phases with iconic β" monoclinic rod cross-sections [9, 10, 12]. The rod-shaped morphology of the precipitates was maintained in the 72 hr sample. Upon 1000 hrs of aging the presence of the rod precipitates is extremely rare, replaced by plate-like or cubic shaped β-phase as previously seen in the APT reconstruction.

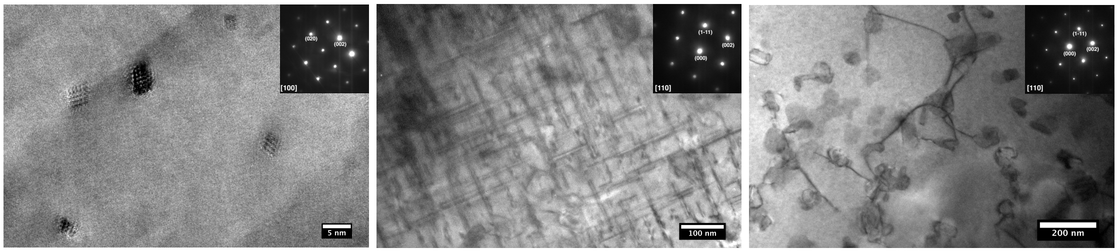

(a) (b) (c)

Figure 3.8: (a) HRTEM micrograph depicting β" monoclinic rod cross-sections along the $\langle 100\rangle_{\alpha\text{-}Al}$ zone axis after aging a sample of 356 at 200°C for 5 hrs. (b) and (c) Bright-field TEM images along the $\langle 110\rangle_{\alpha\text{-}Al}$ zone axis after aging for 72 hrs and 1000 hrs, respectively.

Q-phase precipitate rods and Si rich nano-particles were identified in all other aged alloy samples, including CTQ whose 3-D reconstruction had previously only demonstrated θ'-phase plates. θ'-phase plates are observed in aged samples of GMQ2 and WTQ2 in contrast to the 3-D reconstruction shown previously, which was due to the low number density of the plates in the alloy systems. The TEM micrographs for these samples are shown in Figure 3.9. The images were taken off-zone axis for enhanced contrast. Figure 3.9(a) and (b) demonstrate the presence of the platelet θ'-phase which was not detected in the APT samples for both GMQ2 and WTQ2, while Figure 3.9(c) demonstrates the presence of the Q-phase rods that were not observed in the APT run for the CTQ sample. This demonstrates the necessity of using both APT and TEM techniques together in identifying precipitate phases due to their different length scales.

With regard to a Cu:Mg sub-lattice, this study finds that at zero Cu levels the B'-phase observed in alloy 356 is metastable, resulting in β-phase Mg_2Si upon further aging at 200°C. This is in contrast to the very low Cu containing CM alloy (0.13 wt.%). A bright-field TEM micrograph of alloy CM aged for 1000 hrs at 200°C tilted down the $\langle 111\rangle_{\alpha\text{-}Al}$

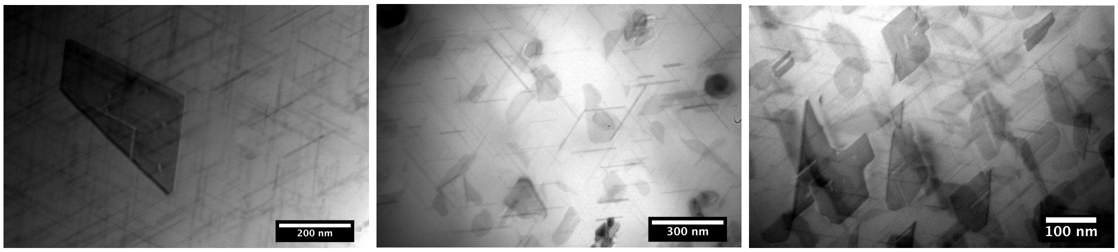

(a) (b) (c)

Figure 3.9: TEM bright-field micrographs from samples of (a) GMQ2 aged for 1000 hrs at 200°C, (b) WTQ2 aged for 1000 hrs at 200°C, and (c) CTQ aged for 72 hrs at 200°C. The images show the presence of the missing Q- and θ'-phases that were not contained within their respective 3-D reconstructions.

is shown in Figure 3.10. Rod-type Q-phase particles and globular Si nano-particles are clearly visible. The Q-phase hexagonal crystal structure and rod-like morphology was maintained with even a small addition of Cu to the alloy. In contrast, the transformation from hexagonal B'-phase with rod-like morphology to cubic β Mg_2Si with plate/cuboidal morphology occurred without this addition. This indicates that the Q-phase is stabilized at lower Cu content levels than previously assumed in both the literature and CALPHAD thermodynamic databases.

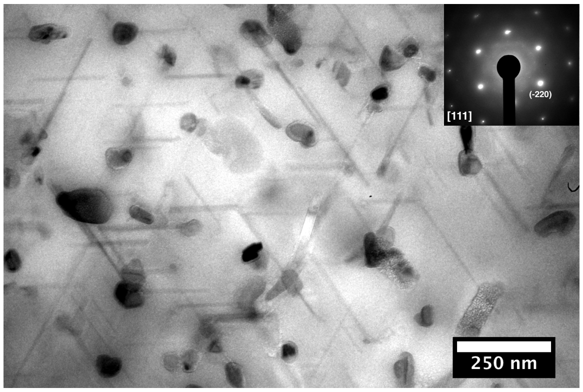

Figure 3.10: TEM micrograph of CM aged for 1000 hrs at 200°C tilted down the $\langle 100 \rangle_{\alpha\text{-}Al}$.

3.3.3 First-Principles Sub-lattice Assessment

The fully relaxed formation enthalpies for the Q-phase compound have been calculated with varying Cu and Mg concentrations. The calculations were performed using the crystal structure of the $Al_3Cu_2Mg_9Si_7$ Q-phase pictured in Figure 3.11, which was identified by Wolverton [17] as the most stable ground-state composition. The formation enthalpy for this composition of Q-phase is -0.154 eV/atom. The Cu atoms were removed from the Wolverton composition to obtain the B'-phase composition $Al_3Cu_0Mg_9Si_7$ and the enthalpy of formation was found to be -0.056 eV/atom. As a reference the Cu-free stable β-phase Mg_2Si compound enthalpy of formation (-0.162 eV/atom) is also plotted. The Wolverton composition was changed to the Arnberg composition ($Al_4Cu_2Mg_8Si_7$) by replacing a *Mg3* site atom with an Al atom. The enthalpy of formation for this composition was found to be -0.133 eV/atom. This composition is more similar in Al content to the measured Q-phase compounds than the $Al_3Cu_2Mg_9Si_7$ composition, though both are slightly richer in Si. Using the Arnberg composition, variations on the Cu and Mg content have been performed. Starting with all Cu atoms replaced by Mg the $Al_4Cu_0Mg_10Si_7$

compound has a formation enthalpy of -0.012 eV/atom. This is remarkably higher in energy than either of the Arnberg or Wolverton compositions and the Cu-free β-phase. The $Al_4Cu_1Mg_9Si_7$ compound with a Mg on the *Cu1* site has a formation enthalpy of -0.068 eV/atom, while the Cu rich $Al_4Cu_3Mg_7Si_7$ compound with Cu on a *Mg3* site is -0.107 eV/atom. All compounds that exhibit a change in Cu content with a corresponding Mg change from the Arnberg composition exhibit an increase in formation enthalpy. The fully relaxed formation enthalpies for these compounds is plotted in Figure 3.12(a) as a function of the fraction $x_{Cu}/(x_{Cu}+x_{Mg})$.

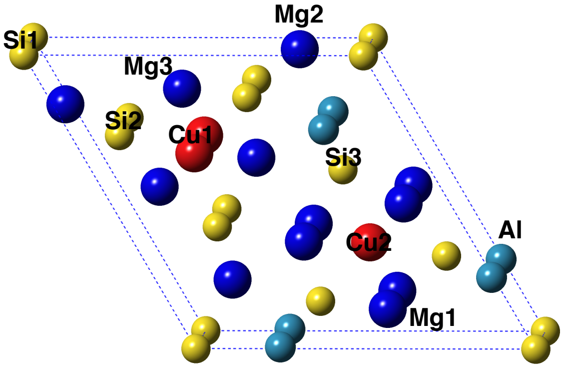

Figure 3.11: Schematic diagram of the crystal structure of Q-phase $Al_3Cu_2Mg_9Si_7$. There are 21 atoms and 9 distinct symmetry points per cell.

To fully determine the stability of these compounds one must compare the formation energies relative to the complete convex hull of all the ground-state Al-Mg-Si-Cu compounds. Using the formation enthalpies for all stable compounds in the quaternary system the distance from the convex hull was calculated for all previously mentioned Q-phase off-stoichiometric compounds. These distances are plotted in Figure 3.12(b) as a function of the fraction $x_{Cu}/(x_{Cu}+x_{Mg})$. A similar trend is observed as in Figure 3.12(a). As expected all off-stoichiometric compounds from the Wolverton composition lie off the convex hull

(hull distance of 0 eV/atom). It is found that the most stable off-stoichiometric compound is the Arberg composition ($Al_4Cu_2Mg_8Si_7$), followed by the Cu rich $Al_4Cu_3Mg_7Si_7$, the Cu-free B'-phase $Al_3Cu_0Mg_9Si_7$, the Cu-lean $Al_4Cu_1Mg_9Si_7$, and finally the Al-rich Cu-free $Al_4Cu_0Mg_10Si_7$ compound. Seeing as how the Cu-free B'-phase is an experimentally observed meta-stable compound, the DFT calculations would suggest that it is not-unreasonable to potentially observe those phases with similar hull distances such as the Cu-lean and Cu-rich Q-phase compounds as is in fact the case.

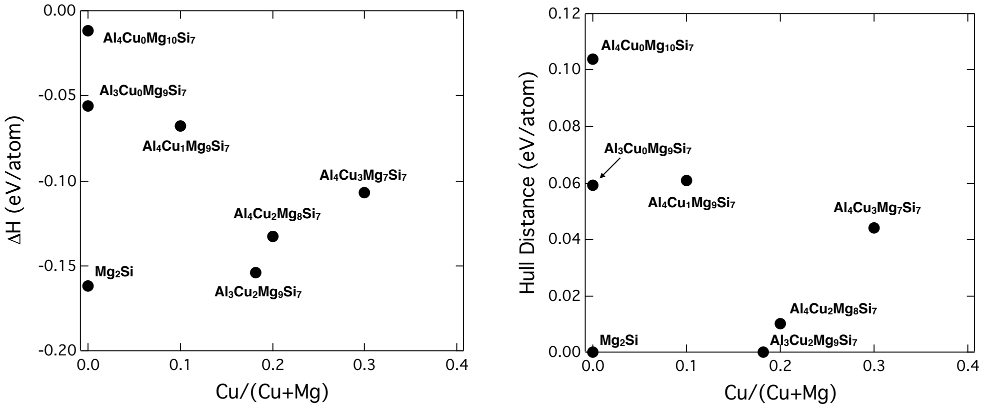

(a) (b)

Figure 3.12: (a) Fully relaxed formation enthalpies (eV/atom) and (b) the Hull distances for various off stoichiometric Q-phase compounds as a function of the Cu/(Cu+Mg) fraction.

These off stoichiometric Q-phase compounds can be further explored by calculation of the individual defect formation enthalpies for vacancy and anti-site substitution. Table 3.7 summarizes the defect formation enthalpies. The notation X_Y corresponds to a defect of type X on a Y site. Table 3.7 lists the lowest energy defect of type X for that of all Y sites.

Vacancy defect formation energy on a Cu site shows the lowest value among the 9 symmetry-distinct sites in the Q-phase, thus meaning that a vacancy can be formed most easily on a Cu site. This comes as no surprise considering the origins of the Q-phase crystal structure which was based on the Th_7S_{12} crystal structure. In modeling the Q-phase crystal after that of Th_7S_{12}, the Al, Mg, and Si atoms sit on the sub-lattice, while Cu occupies the interstitial sites. The low energy of the V_{Cu} vacancy is understandable based on the fact of the existence of the Cu-free B' ($Al_3Mg_9Si_7$) in the Al-Mg-Si system, which has the same crystal structure as the Q-phase without the Cu atoms [13, 32, 81].

It can be seen that by far the lowest energy native defect is the Al_{Mg3} with a formation energy of 0.11 eV/defect. This corresponds quite well with the reported Q-phase compositions which are all rich in Al compared to the ground-state $Al_3Cu_2Mg_9Si_7$. These defect energies suggest that under experimental conditions the Q-phase could be observed to substitute Al atoms at the Mg sites relatively easily. For example, a change from the $Al_3Cu_2Mg_9Si_7$ compound to that of the Arnberg $Al_4Cu_2Mg_8Si_7$ is the result of anti-site defects of Al_{Mg3}. The compound reported by Phragmen ($Al_5Cu_2Mg_8Si_7$), is actually that of the Arnberg compound with an Al_{Si} defect. Comparing the computed defect energies that result in the loss of a Si atom, the lowest is that of Al_{Si1}. This suggests that it is possible for compounds to be observed experimentally with off-stoichiometry with a lack of Mg and Si atoms. However, in the case of the observed Cu deficiency by substitution of Mg atoms, the energies of the computed defects can not explain this occurrence, since there are lower energy defects of the Mg_X and X_{Cu} type than the observed Mg_{Cu} defect that would be necessary to obtain these compounds. Structures resulting from multiple defects though would require a full treatment of calculations with interactions of defects.

It is important to note that only the ground-state energies have been considered in comparing the various configurations of the Q-phase. Any effects due to contributions from the entropy at T>0 to the formation energy have been ignored. Entropy has been shown to be

Table 3.7: First-principles defect formation enthalpies for vacancy and anti-site substitution in the Q-phase ($Al_3Cu_2Mg_9Si_7$).

Defect ΔH_f^d (eV/defect)									
V_{Al}	1.68	Al_{Cu1}	0.38	Cu_{Al}	0.80	Mg_{Al}	0.50	Si_{Al}	0.52
V_{Cu2}	0.44	Al_{Mg3}	0.11	Cu_{Mg2}	1.06	Mg_{Cu2}	1.09	Si_{Cu1}	0.46
V_{Mg2}	1.12	Al_{Si1}	0.55	Cu_{Si1}	0.88	Mg_{Si1}	1.64	Si_{Mg2}	1.04
V_{Si2}	1.31								

significant in the ordering of the θ- and θ'-phases in the Al-Cu binary system [8]. DFT calculations demonstrated that vibrational entropy considerations favored the tetragonal θ phase over the cubic θ'-phase for temperatures greater than 200°C, as was experimentally demonstrated by Silcock et al. [23]. The small difference (21 meV/atom) in the enthalpy of formation energies between the Wolverton calculated and Arnberg experimental compositions suggests that finite temperature energy terms are significant enough to produce changes in the stability of the Q-phase structure and composition [8, 92]. Entropic energy contributions should not be ruled out as having an insignificant effect, however calculations of phonon modes, electronic, and configurational entropy terms are beyond the scope of this work. It can be asserted though, that the ordering determined by the DFT calculations for the various compounds is significant due to the large differences in enthalpy of formations, which are below the error associated with the threshold of convergence of 1 meV/atom.

3.3.4 Thermo-Calc Database Assessment

A comparison between the experimentally determined phases in the alloy systems and those of the commercially available TCAL2 database was performed to assess thermodynamic modifications that would be necessary in correctly describe experimental observation. The TCAL2 database uses the Phragmen stoichiometric line compound $Al_5Cu_2Mg_8Si_6$ to describe the Q-phase and has no solubility description for composition variation. An isotherm was generated using the TCAL2 database for 0.8 at.% Si content and a range of Mg from 0-3 at.% and Cu from 0-1.5 at.% at 200°C. The isotherm is shown in Figure 3.13(a). As can be seen, due to the line compound description of the Q-phase there exists only a very small two phase region of FCC+Q. This two phase region is bounded by the three phase regions of: FCC+Q+Si, FCC+θ+Q, and FCC+Q+β. Due to the small nature of the two phase FCC+Q region, these three phase regions are very narrow. Figure 3.13(b) demonstrates the narrow three phase FCC+Q+Si region using a 3-D tie tetrahedron. Focusing in on the Al-rich corner of the phase diagram, Figure 3.13(c) is the isotherm over a range of Mg and Cu contents in at.%. The equilibrium phases identified for each alloy discussed in this chapter, as well as additional alloys explored as part of this project are plotted on the isotherm. Those alloys exhibiting the FCC+Q+θ+Si phases are plotted in red, the FCC+Q+Si phases in blue, and FCC+β+Si phases in green when aged at 200°C to near equilibrium conditions. The open squares correspond to high Si containing cast alloys and the closed circles correspond to low Si containing wrought alloys. The phase boundaries present in the isotherm in this rich Al corner are invariant over the range of Si content for the examined alloy systems.

It is clear that the TCAL2 isotherm phase boundaries at 200°C do not align with the experimentally observed equilibrium phases. This is primarily caused by the narrow Q-phase region discussed previously. The θ-phase region extends down to lower Cu levels than which has been identified by experiment. As observed previously the addition of small Cu amounts was actually found to stabilize the Q-phase while preventing β-phase

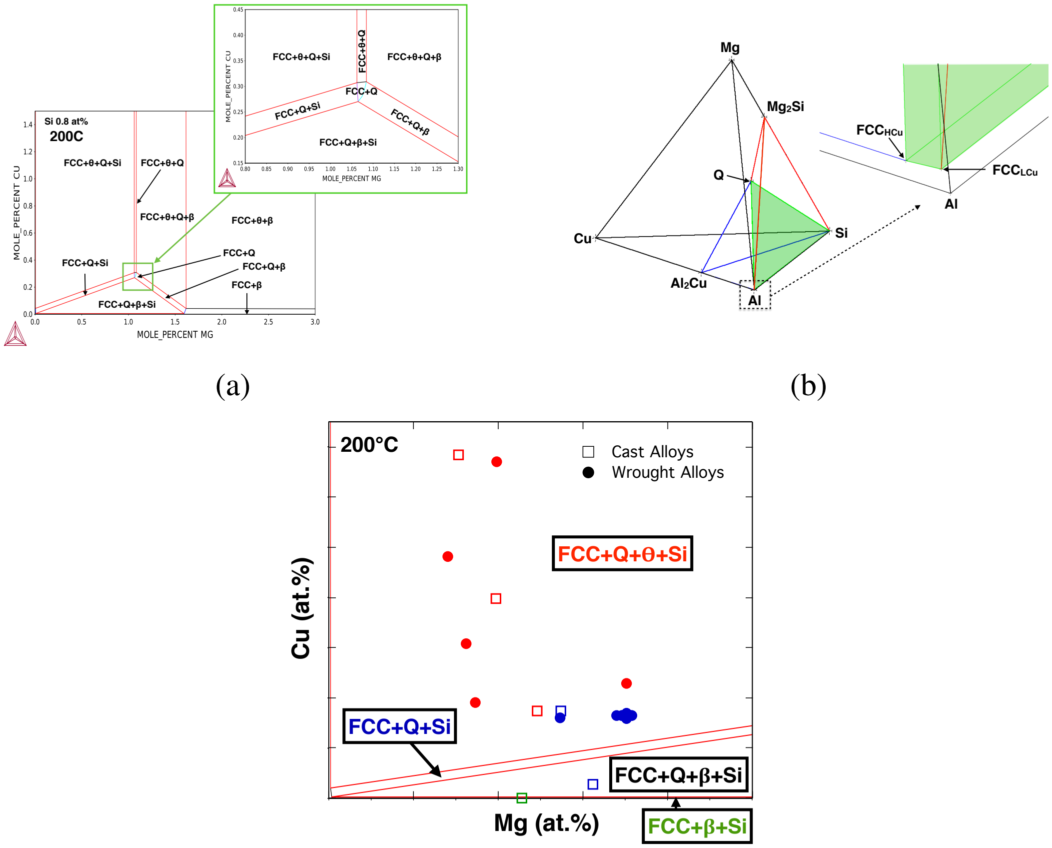

(a) (b)

(c)

Figure 3.13: Isotherms for the TCAL2 database. (a) Isotherm for 0.8 at.% Si and a range of Mg from 0-3 at.% and Cu from 0-1.5 at.% at 200°C. (b) Tie tetrahedron of the TCAL2 database with FCC+Q+Si region highlighted in green. (c) Isotherm over a range of Mg and Cu at 200°C. Experimentally determined equilibrium phases are plotted with FCC+Q+θ+Si phases in red, FCC+Q+Si in blue, and FCC+β+Si in green.

formation, though the TCAL2 database shows a large region of β Mg_2Si at low Cu levels. It is apparent that a new Q-phase thermodynamic description in necessary for modeling the Al-Cu-Mg-Si system.

The thermodynamic description of the Q-phase was remodeled in the QTDB using the CALPHAD method. The experimentally measured phase equilibria tielines were assessed and utilized in calibrating the Gibbs energy entropy and enthalpy terms. Select tieline data is presented in Table 3.8 for various Cu containing alloys. Of interest is the Cu solubility in the FCC matrix. It can be seen in Table 3.8 that the Cu solubility can reach as high at 0.21 at.%. This occurs in the WQ alloy (0.75 wt.% Cu) where no θ'-phase is present and the matrix has reached max solubility of Cu. Upon further Cu addition as in alloy WTQ2 (1.44 wt.% Cu) once θ'-phase nucleates the Cu content in the matrix is decreased again. Upon even further Cu addition to the alloy system as in alloy WTQ (3.1 wt.% Cu) the matrix starts to exhibit more Cu in the FCC matrix. In alloy WTQ this enhanced Cu FCC content can potentially be due to the increased time necessary for θ'-phase to achieve equilibrium phase fraction.

Table 3.8: Experimentally measured phase equilibria tielines for various alloys aged at 200°C.

Alloy	Aging Time	Phase	Al (at.%)	Si (at.%)	Mg (at.%)	Cu (at.%)
356	72 hr	B'	18.03	28.86	53.11	0
		FCC	99.80	0.048	0.156	0
CM	1000 hr	Q	20.14	29.00	46.13	4.72
		FCC	99.95	0.013	0.023	0.0087
WQ	72hr	Q	21.96	25.34	41.18	11.52
		FCC	99.71	0.090	0.020	0.18
WTQ2	1000hr	Q	17.66	27.56	42.79	11.43
		FCC	99.92	0.0032	0.023	0.049
WTQ	72hr	Q	20.08	27.51	40.64	11.77
		FCC	99.72	0.042	0.032	0.21

Based on the APT compositional results, a four sub-lattice model was chosen to describe the Q-phase allowing for Mg solubility on the Cu sub-lattice. The CALPHAD sub-lattice model is fundamentally different than the crystal structure or unit cell. The

CALPHAD model specifies a number of sites, in this case 4, the individual elements (one or more) that can sit on each of these sites, and the number of each site that results in a pseudo-stoichiometry. Unlike a unit cell there is no specific layout just an abstract number of sites with specified elements that can exist on each site. Two end members for the bounds of the Q-phase composition were chosen: $Al_4Cu_0Mg_{11}Si_{5.5}$ for the Cu free bound (the measured B' composition), and $Al_4Cu_3Mg_8Si_{5.5}$ for the max Cu solubility. The Si content was reduced slightly in this description to better agree with the APT compositions, while maintaining the four Al atoms of the Arnberg description. Note this is no longer a perfect 21 atom unit cell, but 20.5 atoms and that the thermodynamic database allows for partial atoms. The total Gibbs free energy of the Q-phase was thus described by a combination of these two end members where $G(Al_4Cu_0Mg_{11}Si_{5.5})$ and $G(Al_4Cu_3Mg_8Si_{5.5})$ are expressed as:

$$G = \Delta H - \Delta S * T + X_{Al}G_0(Al) + X_{Cu}G_0(Cu) + X_{Mg}G_0(Mg) + X_{Si}G_0(Si)$$

where ΔH is the enthalpy, ΔS is the entropy, X_i is the number of i atoms in the unit cell, and $G_0(i)$ is the energy for the element i. The enthalpy and entropy term for each end member has been fit to the experimental APT and TEM observations.

New isotherms were generated using the updated QTDB and compared to the experimental data. Figure 3.14(a) shows an isotherm for 0.8 at.% Si content and a range of Mg from 0-3 at.% and Cu from 0-1.5 at.% at 200°C. The two phase FCC+Q region has been expanded due to the Q-phase no longer being a stoihiometric compound, but instead varies with bulk content within the bounds of the two end members. Though, the Q-phase is inhibited from reaching the maximum and minimum composition bounds completely due to the presence of the θ and β phases. The lowest reachable Cu content within the Q-phase is 3.95 at.% and the upper attainable Cu content is limited to 12.21 at.%. Due to the increase in phase space with the two phase FCC+Q region, the three phases regions are also considerably expanded.

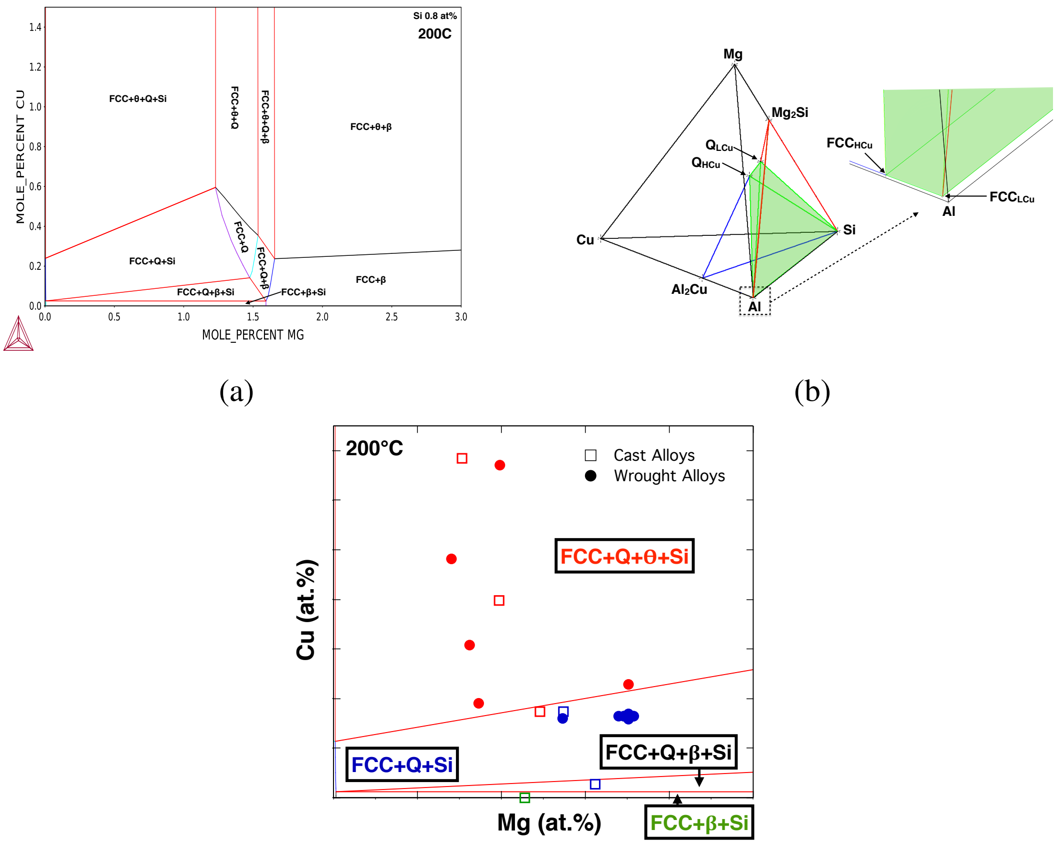

(a) (b)

(c)

Figure 3.14: Isotherms for the updated QTDB database. (a) Isotherm for 0.8 at.% Si and a range of Mg from 0-3 at.% and Cu from 0-1.5 at.% at 200°C. (b) Tie tetrahedron of the QTDB database with FCC+Q+Si region highlighted in green. (c) Isotherm over a range of Mg and Cu at 200°C. Experimentally determined equilibrium phases are plotted with FCC+Q+θ+Si phases in red, FCC+Q+Si in blue, and FCC+β+Si in green.

Of primary interest is the updated phase region of the FCC+Q+Si three phase field.

Figure 3.14(b) demonstrates the now larger FCC+Q+Si three phase region on a 3-D tie tetrahdron. This corresponds to a much larger alloy design space than previously assumed when considering the TCAL2 database for an alloy primarily strengthened using Q-phase precipitation hardening. Figure 3.14(c) is the isotherm at 200°C over a range of Mg and Cu contents in at.%. The equilibrium phases identified for each alloy discussed in this chapter, as well as additional alloys explored as part of this project, are plotted on the isotherm. Those alloys exhibiting the FCC+Q+θ+Si phases are plotted in red, the FCC+Q+Si phases in blue, and FCC+β+Si phases in green when aged at 200°C to near equilibrium conditions. The open squares correspond to high Si containing cast alloys and the closed circles correspond to low Si containing wrought alloys. It can clearly be seen that the new updated database phase regions match well with the experimentally determined equilibrium phases. The experimental and computed phase fractions for the ten alloys examined in the chapter are compared in Table 3.9, separated by cast and wrought and in increasing Cu content.

Table 3.9: Experimental and calculated phase fractions for precipitate phases at 200°C.

Alloy	Q-phase (f$_p$.%)		θ'-phase (f$_p$.%)		Si (f$_p$.%)		β-phase (f$_p$.%)	
	Exp.	Cal.	Exp.	Cal.	Exp.	Cal.	Exp.	Cal.
356 (1000 hr)	0	0	0	0	6.08	6.11	0.49	0.67
CM (1000 hr)	1.00	0.81	0	0	6.92	6.90	0	0.32
CQ (72 hr)	1.18	1.20	0	0	5.34	5.38	0	0
CTQ (72 hr)	0.66	0.72	3.52	3.18	4.98	4.99	0	0
WQ (72 hr)	1.28	1.55	0	0	0.30	0.15	0	0
WTQ3 (1000 hr)	0.76	0.82	0.75	0.13	0.75	0.74	0	0
GMQ2 (1000 hr)	1.60	1.69	0.39	0.04	0.29	0.32	0	0
WTQ2 (1000 hr)	0.71	0.77	1.46	0.86	0.95	0.95	0	0
WTQ1 (24 hr)	0.64	0.67	2.09	1.95	0.76	0.67	0	0
WTQ (72 hr)	0.9	0.94	3.1	2.99	0.89	0.91	0	0

The new QTDB correctly predicts 9 of the 10 alloy system equilibrium phases. The CM alloy (with very low Cu) is predicted to have some β-phase, though experiment showed only Q-phase rods. This is due to intentionally keeping the β-phase as the equilibrium phase at zero Cu during the database calibration. By doing so, the four phase FCC+Q+β+Si region sits above the three phase FCC+β+Si region, even though this region has not been experimentally observed. Further database calibration of the β-phase could result in a smaller four phase region, though it is beyond the scope of this work. The new QTDB accurately predicts the equilibrium phase fractions for all precipitate phases, with the largest error occurring near the Q and θ phase boundary. Far from the boundary the θ-phase is accurately predicted, i.e. the CTQ, WTQ1, and WTQ alloys, though closer to the boundary the database overestimates the θ-phase fraction. Further calibration of the θ-phase would be necessary to correct this.

To further assess this new database, two alloys were designed by QuesTek to test the phase boundary prediction at very high Mg levels, one with higher Cu (HQHCu) and one with lower Cu (HQLCu) levels. The alloys were designed to have a Q-phase fraction of 3.49% and 3.22%, respectively. These alloys underwent the standard homogenization treatment of 5 hr aging at 530°C and then artificially aged for 72 hrs at 200°C. 3DAPT was performed on the aged samples and the 3-D reconstructions are shown in Figure 3.15(a)-(b). The isoconcentration surfaces chosen for the Q-phase are shown in purple, with a 12 at.% Mg+Si surface chosen for the HQHCu alloy and a 10 at.% Mg+Si surface chosen for the HQLCu alloy. As can be seen in the APT reconstructions only Q-phase precipitates are observed for both alloys. TEM was performed to identify potentially low number density phases such as the θ'-phase that may have been missed by the small volume sampling of the APT. TEM bright-field micrographs for the two alloys are shown in Figure 3.15(c)-

(d). Both samples were tilted down the $\langle 100\rangle_{\alpha\text{-}Al}$ zone axis. The TEM micrographs for both samples only showed the presence of Q-phase rods like that of the APT analysis. As predicted by the updated QTDB database, from both APT and TEM data it was determined that only Q-phase precipitation occurred during aging for these two alloys at 200°C.

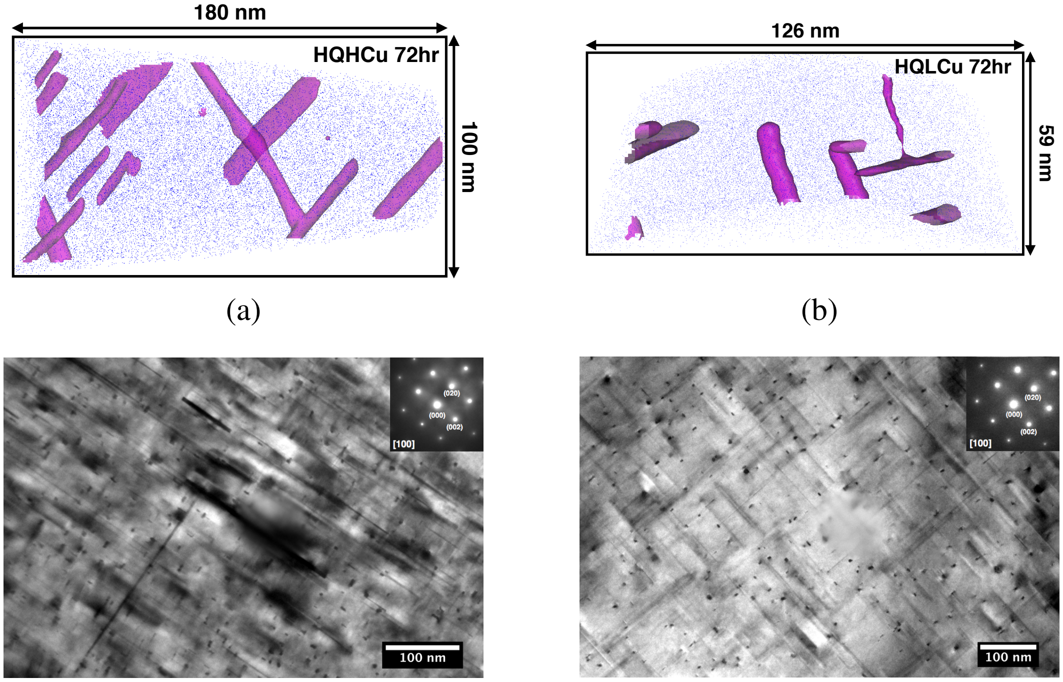

(a) (b)

(c) (d)

Figure 3.15: 3-D APT reconstructions for (a) HQHCu and (b) HQLCu alloys aged for 72 hrs at 200°C. Q-phase Mg+Si iso-surfaces are shown in purple. TEM bright-field micrographs for (c) HQHCu and (d) HQLCu tilted down the $\langle 100\rangle_{\alpha\text{-}Al}$ zone axis.

Volume fraction measurements of the Q-phase are compared to the predicted phase fractions for both the TCAL2 and QTDB databases in Table 3.10. The cast alloys did not contain the desired amount of Q-phase as measured by APT as was predicted by the QTDB database, though the predicted equilibrium phases are in much better agreement with the QTDB database than with the TCAL2 database. SEM was performed on these alloys to determine if homogenization was properly achieved. SEM images are shown in Figure 3.16 for both HQHCu and HQLCu after the standard homogenization/solution heat treatment of 530°C for 5 hrs. As can be seen, large dark and light particles are visible even after homogenization. These same particles are also seen in the as-cast alloys before homogenization (not shown). EDS analysis of these particles show that the dark phases are rich in Mg and Si with a range of compositions from particle to particle. The light particles have been found to be rich in Fe and Cu. These larger particles are formed during solidification of the alloy due to the slow air-cooled solidification process used by QuesTek during casting. These primary solidification phases are greatly reduced in the Cu-plate chilled sand-casts and non-existent in the Cu-mold button alloys. These phases reduce the overall amount of Mg, Si, and Cu available to Q-phase precipitation thus reducing the phase fraction as observed. Great care must be taken during the casting of high Mg and Cu containing alloys, as well as finding more optimum homogenization/solution heat treatments if the desired Q-phase fraction is to be achieved.

Table 3.10: Experimental and calculated phase fractions for HQHCu and HQLCu alloys aged at 200°C.

Alloy	QTDB			TCAL2			Experiment		
	Q (f_p.%)	θ (f_p.%)	β (f_p.%)	Q (f_p.%)	θ (f_p.%)	β (f_p.%)	Q (f_p.%)	θ (f_p.%)	β (f_p.%)
HQHCu	3.49	0	0	1.78	1.28	1.03	1.97	0	0
HQLCu	3.22	0	0	2.79	0.64	0	1.06	0	0

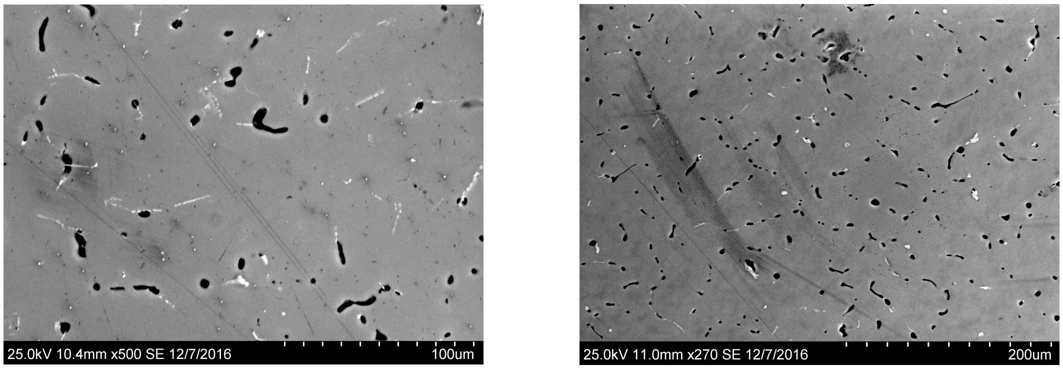

(a) (b)

Figure 3.16: SEM SE micrographs for (a) HQHCu and (b) HQLCu after homogenization/solution heat treatment.

3.4 Conclusions

The composition of the Q-phase and β-phase along with its precursors was explored in a series of both wrought and cast aluminum alloys using both 3DAPT and TEM. Rod-shaped Q-phase precipitates were observe in all alloys containing Cu when aged at 200°C, while the Cu free 356 alloy demonstrated β" and B'-phase rod-shaped precipitates eventually transforming to the equilibrium β-phase Mg_2Si plate/cuboids upon long term aging.

Equilibrium aging conditions were utilized to achieve accurate compositions while mitigating the matrix/precipitate overlap that can occur with finer particle dispersions when analyzed using the proxigram method. However, due to the long aging time necessary to achieve these particle sizes, the number density of these particles is small and therefore it becomes difficult to locate the particles within a typical 3-D APT reconstruction volume. TEM was required to determine the existence of particle phases of low number density not present in APT runs and to identify the crystallographic cross-sections of β-phase precursors. Chemical analysis of Q-phase particles with difference cross-sections (circular and lath) demonstrate that both types exhibited the same compositions. It is therefore suggested that cross-section morphology alone should not be used to distinguish particle phases as has been regularly found in literature.

The Cu:Mg sub-lattice proposed in this work is supported by the experimental APT compositional analysis performed on 10 different alloy systems. The Q-phase compositions observed varied from reported stoichiometries found in the literature, especially with regards to Cu and Mg contents. The replacement of Cu atoms with Mg atoms in the Q-phase structure was indicated in an alloy system with only a small amount of Cu addition. Furthermore, the similarity of the Q-phase to the β'-phase type C precursor (B') in the commonly used 356 alloy with no Cu was observed where the composition found using APT was that of the Q-phase stoichiometry replacing all the Cu with Mg.

First-principles studies of various Q-phase off stoichiometric compounds and the defect formation enthalpies for vacancy and anti-site substitution associated with the $Al_3Cu_2Mg_9Si_7$ crystal structure have been reported. DFT calculations are unable to reconcile the stability of any change with Cu variation from the Wolverton stoichiometry. Comparisons of the convex hull distance compared to the experimentally observed meta-stable B'-phase does potentially suggest the meta-stability of both Cu-lean and Cu-rich Q-phase compounds. Defect formation enthalpies are able to partially explain the occurrence of Al rich and Si lean compositions in experimental conditions.

The thermodynamic description of the Q-phase has been updated using the suggested Cu:Mg sub-lattice from APT compositional analysis. Cu and Mg solubility within the Q-phase composition opened up the FCC+Q+Si phase region and was found to agree well with the experimentally determined equilibrium phases at 200°C. The phase region was assessed at high Mg and Cu contents with two alloy designs. Both alloys demonstrated Q-phase precipitation in agreement with the updated database, though more controlled casting processes are necessary to achieve the desired phase fractions.

4 Rod and Plate Growth in Aluminum Alloy Systems

4.1 Background

The development of high-strength levels in the Al-Si-Mg-Cu sysem is achieved by a secondary hardening reaction. In the 2xxx, 6xxx, and 3xx.x systems, secondary hardening is accomplished by the precipitation of fine Q-phase and β'-phase rods and θ'-phase plates. Morphological changes occur in precipitate phases upon further aging near the end of a first-order phase transformation, known as Ostwald ripening or coarsening [93]. Due to the result of a large interfacial surface energy, relaxation of the system occurs and is characterized by an increase in the average size of the coarsening dispersion at near constant volume fraction. Decreasing of the interfacial energy in this way leads to the dissolution of small precipitates and the growth of large ones by the diffusive mass flow from shrinking to growing precipitates. This process of coarsening in a dilute binary mixture has been well developed by Lifshitz and Slyozov [94] and Wagner [95]. Their classical theory of coarsening, generally called LSW theory, treated an ensemble of particles and made quantitative predictions of the long time behavior of the average particle size, number density, and supersaturation by application of the Gibbs-Thomson equation relating the interface compositions to the curvature of the precipitates. According to LSW theory the rate equation and the average particle radius are given by the following equation:

$$\frac{dr}{dt} = K\frac{1}{r}\left(\frac{1}{\bar{r}} - \frac{1}{r}\right) \tag{4.1}$$

Integration of Equation 4.1 gives:

$$\overline{r}^3 - \overline{r}_0^3 = \frac{4}{9}K(t - t_0)$$

where dr/dt is the coarsening rate of a particle of radius r, $\overline{r}$ is the the average particle radius at time t, $\overline{r}_0$ is the average particle radius at time t_0 when coarsening begins, and K is the rate constant. The rate constant K is defined as

$$K = \frac{2Dc_\infty \sigma V_m^2}{RT}$$

where D is the diffusivity in the matrix, c_∞ is the solubility in the far-field matrix, σ is the interfacial energy of the particle/matrix, V_m is the molar volume of the precipitate phase, T is the absolute temperature, and R is the gas constant.

Since a fine particle dispersion is such a significant source of strength, the kinetics of coarsening are of great practical interest. Understanding the stability of these dispersions to coarsening is a major concern for the development of high-temperature alloys. As such, much work has been performed on the development and expansion of LSW theory to ternary systems [96, 97], multicomponent alloys [98, 99, 100, 101], and systems with non-spherical particles [102, 103]. Björklund et al. [96] considered the problem of coarsening of cementite in steel but restricted the model to a ternary system, dilute solutions, and fixed precipitate compositions that did not change with particle radius. Kuehmann and Voorhees [97] described a theory of coarsening (KV model) for a general, non-ideal, non-dilute ternary alloy taking into account the Gibbs-Thomson effect of curvature on precipitate composition but neglected off-diagonal diffusivity terms. Work by Umantsev and Olson [98] also removed the restriction of dilute solution thermodynamics and expanded the theory of coarsening to multicomponent coarsening, but neglected the effects of interfacial curvature. Morral and Purdy [99, 100] extended the results of Umantsev and Olson for coarsening of an n-component system to include the off-diagonal diffusion coefficients and predicted the temporal evolution of the particle radius. More recent work by Philippe and Voorhess [101] expanded on the KV model to a general theory of coarsening for a multicomponent alloy including the off-diagonal terms in the diffusion tensor. They also solved for the temporal evolution of the particle radius, number density, and precipitate composition. In the case of non-spherical precipitate coarsening, Speich and Oriani [102] considered the problem of coarsening of rod-like Cu precipitates in binary Fe-Cu alloys. They modified LSW theory for both non-sphericity of the diffusion field and reformulated the Gibbs-Thomson equation for nonspherical particles. A theory of coarsening for multicomponent M_2C carbide rod-shaped precipaites was developed by Lee et al. [103]. Lee used the approach of Björklund and incorporated the generalized Gibbs-Thomson equation solved by Johnson [104] for equilibrium rod-shaped particles. Lee solved for the temporal evolution of the radius and length of the rods with a coarsening rate depending of the aspect ratio of the rods.

In this work, both 3DAPT and TEM experiments have been performed to measure the particle size and change in composition as a function of aging time for a series of both wrought and cast alloys. Accurate rod radii from 3DAPT and particle lengths from TEM are used to determine the effects of aging temperature and time on particle coarsening. Particle size and matrix phase compositions are used in the Gibbs-Thomson equation to determine the critical radius of nucleation for Q-phase precipitation. *In-situ* TEM experiments exploring the coarsening of Q-phase particles show that the evolution of the volume of the rod-like particles follows the classical LSW $t^{\frac{1}{3}}$ power relation. The Lee coarsening model is then adapted for use in describing the evolution of the Q-phase rod particles as both a function of aging time and temperature. Experimental measurements and an extensive curation of archival literature data are used to calibrate the Lee model and is shown to describe the particle evolution well. APT and TEM observations of the θ'-phase nucleation and growth demonstrate a longer nucleation incubation time than the Q-phase followed by heterogeneous precipitation onto the Q-phase rods. Q-phase rods also act to inhibit the growth of the θ'-phase. The development of a coarsening model for θ'-phase platelets is performed using machine learning (ML). Using experimental particle size measurements and data from the literature as input, the ML code is found to describe the plate thickness and diameters well using the correct set of attributes and expanders.

4.2 Methodology

4.2.1 Experimental Methods

All wrought and cast alloys discussed in Chapter 3, as well as all alloys pictured in the ThermoCalc isotherms in Section 3.3.4 were investigated using 3DAPT and TEM. These alloys were aged after homogenization over a range of aging temperatures from 200°C to 450°C for 30 min to 1000 hours. All samples were water quenched after aging. Rod particle radii were primarily obtained from APT reconstructions when available, else they were measured from TEM micrographs. Rod radii were measured in the APT reconstruction via a projected Mg+Si 2-D concentration profile perpendicular to the primary rod growth direction $\langle 100\rangle_{\alpha\text{-}Al}$. All rods contained in the APT reconstruction for an alloy were measured. Figure 4.1(a) shows the placement of a 2-D concentration profile across one Q-phase rod found in alloy WQ aged for 24 hrs at 200°C, with a 7 at.% Mg-Si iso-surface used as a guide. An image is then taken perpendicular to the 2-D profile as shown in Figure 4.1(b) and an ellipse is fit to the cross-section profile. The area of the ellipse if converted to that of a circle and the equivalent circular radius is recorded. Similarly, θ'-phase plate thickness was measured using a Cu 2-D concentration profile. By utilizing this method the isoconcentration profiles chosen to visualize the rods and plates has no bearing on the radius and thickness measurements. Rod length and plate diameters were measured using TEM as discussed in Section 2.2.5 due to the rods and plates typically being to large to be contained in a single APT reconstruction volume.

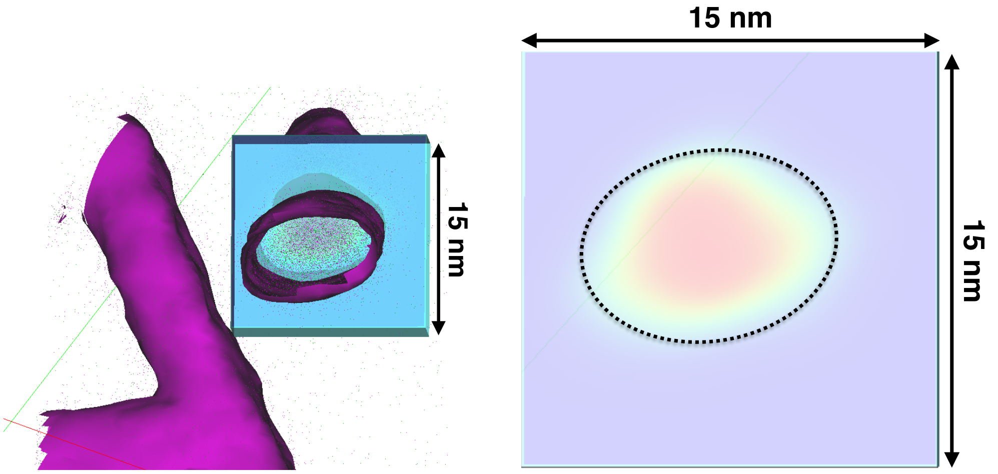

(a) (b)

Figure 4.1: Process for measuring the rod particle radius using a 3-D APT reconstruction. Alloy shown is WQ aged for 24 hrs at 200°C. (a) The 2-D Mg+Si profile is aligned perpendicular to the rod. (b) The profile is measured using an elliptical fit.

In-situ TEM was performed on an un-aged homogenized sample of alloy GMQ2. This experiment was performed at NU using a JEOL JEM-2100F FasTEM microscope and a Gatan double-tilt heating stage. The sample was aligned down the $\langle 100\rangle_{\alpha\text{-}Al}$ zone axis. The sample was held at 300°C to observe particle growth and coarsening. Image series were taken upon temperature holding and stitched together using the open-source image processing software Fiji. All images are time stamped so elapsed time between subsequent images is known.

4.2.2 Computational Methods

Modeling of the Lee coarsening model for application towards the Q-phase was performed in MATLAB. The model input parameters include: aging time, aging temperature, the matrix compositions, and the Q-phase precipitate compositions. Various other constants are needed and include solute diffusivities, molar volume, interfacial energy, and critical radius size. Diffusivities of solutes in Al at temperature are calculated using the following equation:

$$D = D_0 exp(-Q/RT)$$

Diffusion coefficients for Mg and Si were taken from Smithells Metal Reference Book [105], with the pre-exponential factors being: $D_0^{Mg} = 6.23 \times 10^{-6}\ m^2/s$ and $D_0^{Si} = 2.48 \times 10^{-4}\ m^2/s$, and the activation enthalpies being: $Q^{Mg} = 115\ kJ/mol$ and $Q^{Si} = 137\ kJ/mol$. Diffusion coefficients for Cu are taken as $D_0^{Cu} = 6.54 \times 10^{-5}\ m^2/s$ and $Q^{Cu} = 136\ kJ/mol$ from Fujikawa and Hirano [106]. Diffusion coefficients for Al are taken as $D_0^{Al} = 1.37 \times 10^{-5}\ m^2/s$ and $Q^{Al} = 124\ kJ/mol$ from Dais et al. [107]. The molar volume of the Q-phase is taken from the DFT Wolverton 21 atom unit cell with a volume of 0.3779 nm^3 corresponding to a molar volume of $1.084 \times 10^{-5}\ m^3/mol$. The interfacial energy of the Q-phase and the critical radius of nucleation were used as calibration constants. The calibration of the model will be discussed in more detail in Section 4.3.1.2.

Machine learning software MAGPIE was utilized in modeling the growth and coarsening of the θ'-phase plates. The diameter and the thickness of the θ' plates was modeled independently. Plate diameter and thickness as functions of aging time, temperature, and alloy composition where generated to accurately describe the growth and coarsening of θ' platelets. Details of the ML code including the function expanders chosen and regression techniques can be found in Appendix A.

4.3 Results and Discussion

4.3.1 Q-Phase Particle Evolution

Q-phase rod-like particle morphology evolution is observed at 200°C using both APT and TEM for alloy GMQ2. The Gibbs-Thomson equation is applied to determine a critical radius of precipitation. *In-situ* TEM is also used to track the particle evolution continuously in the GMQ2 alloy at 300°C and shown to follow classical LSW coarsening theory. The particle morphology of the Q-phase is also explored for a range of aging temperatures for a series of alloys, and seen to undergo re-orientation at temperatures $>$300°C. The rod shaped morphology evolution is then modeled using the Lee coarsening model.

4.3.1.1 APT and TEM Particle Measurements

An isothermal aging study was performed for the GMQ2 alloy at 200°C. Samples of GMQ2 were aged for 5 min, 15 min, 30 min, 1 hr, 5 hrs, 24 hrs, 100 hrs, and 1000 hrs. 3DAPT was performed for all samples and TEM was performed on all samples aged for 30 min or longer. APT reconstructions demonstrated no precipitation in the 5 min and 15 min samples. Solute cluster analysis performed on these samples did show potential clustering of Mg atoms with a average cluster radius of 0.94 nm for the 5 min sample and 0.93 nm for the 15 min sample. The cluster analysis did show a trend similar to a random distribution, as such the data is not included in further analysis of Q-phase evolution. Q-phase particle size data is shown in Figure 4.2(a). The aspect ratio of the rods (A_s) was calculated as $A_s = L/(2r)$, were length (L) was measured by TEM and radius (r) was measured via APT. The volume of the rod particles was calculated using the volume of a cylinder of radius (r) with semi-spherical caps with total length (L) such that volume $V = 2\pi r^3(A_s - 1/3)$.

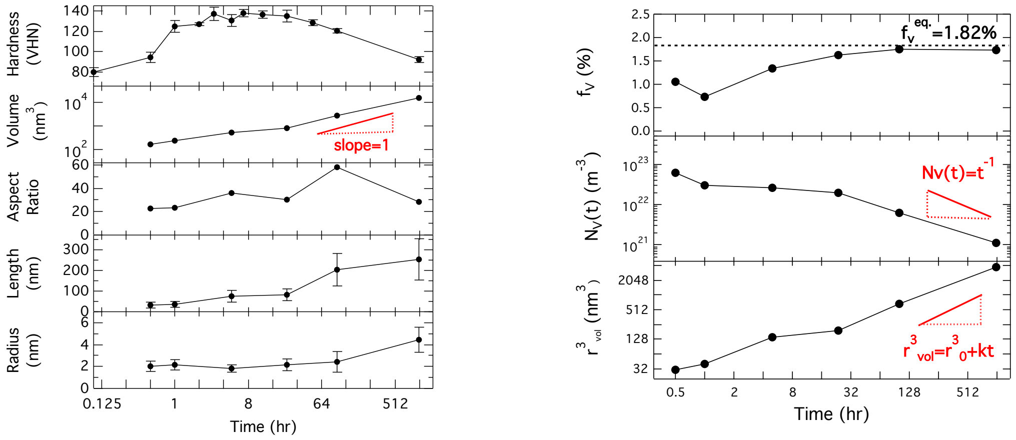

(a) (b)

Figure 4.2: Q-phase particle evolution data as measured from APT and TEM (a) Rod radius, length, aspect, volume, and hardness. (b) Rod equivalent volume radius cubed, number density, and volume fraction for isothermal aging study of alloy GMQ2 at 200°C.

As can be seen in Figure 4.2 the radius of the rod-particles is fairly constant from 30 min to 24 hrs of aging with the radius going from ∼1.36 nm to ∼1.78 nm, respectively. During this time period the length of the particles increases from ∼30 nm to ∼84 nm. The aspect ratio of the rods is seen to increase slightly from ∼23 to ∼34 while the volume increases steadily from 173 nm^3 to 815 nm^3. During this aging time the hardness of the material is seen to hit peak strength around 5 hrs of aging with an increase of ∼58 VHN. After 24 hrs of aging the radius and length of the particle continues to increase such that the volume is seen to increase and approach a slope of one on a log-log plot (linear trend) which is in agreement with the asymptotics of classical LSW theory. During the long-term aging time the aspect ratio is found to peak and approach that of ∼20 again as the rate of growth for the length slows compared to the rate of growth for the radius. Figure 4.2(b) shows the evolution of the equivalent volume radius (r_{vol}) cubed, the number density (N_V), and the volume fraction (f_V). The equivalent volume radius was calculated from the particle volume of the spherically capped cylinders and converted to the radius of a sphere with equivalent volume. The volume fraction of the Q-phase was determined using the precipitate, matrix, and bulk alloy compositions as discussed in Section 2.2.6. The volume fraction is seen to approach an equilibrium value of $\sim$1.74 % upon aging. The measured volume fraction is compared with the calculated equilibrium fraction of $\sim$1.82 % from the updated QTDB. The QTDB is found to slightly over predict the Q-phase volume fraction. Using the particle volumes and the volume fractions, the number density was calculated. As seen in the figure the equivalent volume radius is also shown to follow the temporal evolution of traditional LSW theory ($r^3 = r_0^3 + Kt$). At long aging times the number density is also seen to decrease at a rate that is consistent with classical LSW theory, where $N_V(t) = Ct^{-1}$ where C is a constant [101]. It is determined that the overall particle volume and evolution of the rod-type particles does follow that of the long-termed behavior previously used to describe spherical particles.

With the experimentally measured particle morphology and the matrix composition from the APT runs, the Gibbs-Thomson equation can be applied to determine the critical radius of nucleation for the Q-phase. This parameter is important for modeling the growth of the particles as a starting particle size is a necessary input into the physically based growth models. Assuming volume diffusion-limited coarsening with an unstable equilibrium trajectory, the equilibrium concentration c^{eq} as a function of particle radius is decribed by the dilute solution Gibbs-Thomson-Freundlich equation (typically termed the Gibbs-Thomson equation) given by [108, 109]:

$$c^{eq}(r) = c^{eq}(\infty) exp\left(\frac{2\sigma V_{atom}}{k_B T r}\right) \tag{4.2}$$

where σ is the interfacial energy, V_{atom} is the atomic volume, k_B the Boltzmann constant, T is the temperature, and r is the particle radius. By plotting the *log* of the matrix composition as a function of reciprocal particle size $1/r_{vol}$ in Figure 4.3, the composition trajectory is observed to follow a linear trend according to the Gibbs-Thomson effect as in Equation 4.2. Extrapolating the composition trajectory to infinite particle radius ($1/r_{vol} = 0$) can be used to predict the equilibrium compositions. The extrapolated FCC$_{\alpha\text{-}Al}$ matrix composition is compared to the equilibrium matrix composition in the QTDB (red) and TCAL2 (blue) databases in Figure 4.3. The extrapolated Cu composition is found to be slightly lower while the Mg and Si compositions are found to be slightly higher than the values found at 200°C as calculated for the GMQ2 alloy composition in the QTDB database. Due to the orders of magnitude difference between the various concentrations, the Cu is found to have the largest difference from the extrapolated concentration by 0.146 at.%. Between the TCAL2 and QTDB matrix concentrations compared to the extrapolated concentrations, the QTDB has improved on both the Cu and Mg concentrations with the differences going from 0.38 at.% to 0.14 at.% for Cu and 0.04 at.% to -0.01 at.% for Mg. The Si concentration difference became larger from the TCAL2 to the QTDB being -0.02 at.% to -0.04 at.%.

Extrapolation of the linear concentration fit for the matrix to the bulk alloy composition estimates the critical radius of nucleation. It is at this composition that no precipitates have formed since this composition represents a fully homogenized single phase matrix.

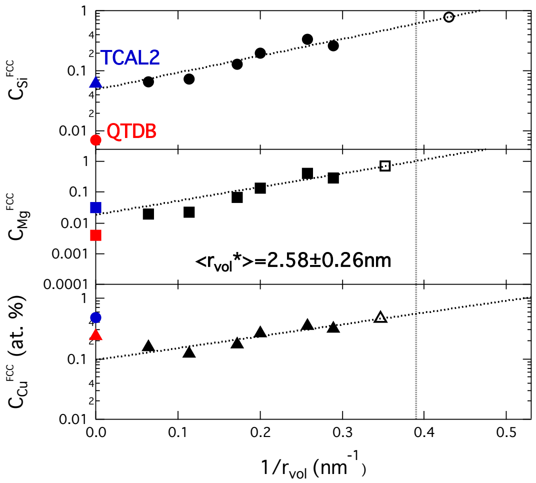

Figure 4.3: Elemental concentrations in the far field matrix as a function of reciprocal equivalent volume particle radius. Black points are the matrix compositions, the open points are the bulk alloy composition, and the red and blue points are the QTDB and TCAL2 equilibrium matrix compositions, respectively.

As can be seen in Figure 4.3 the extrapolation to the bulk compositions for Cu, Mg, and Si have been labeled using open points. The average radius for the three different elements is marked with a vertical dashed line. The critical equivalent sphere volume radius was found to be 2.58±0.26 nm. Though this is a spherical volume radius, it is possible that the Q-phase particle does not nucleate as a sphere, seeing how the θ-phase GP-zones are disk shaped upon nucleation [8] and that the GP-zones of the β-phase are believed to be needle-shaped [37, 110].

In-situ TEM was used to observe the aging of the Q-phase in alloy GMQ2 continuously for 10 min and 43 sec at 300°C of an unaged sample. 300°C was chosen to speed up the kinetics of coarsening. The sample was oriented down the $\langle 100\rangle_{\alpha\text{-}Al}$ zone axis. Two TEM micrographs are shown in Figure 4.4 where (a) is the start of the image sequence and (b) is the end of the image sequence. Two Q-phase particles that are common between the images are indicated to show the rapid growth. Data was collected from analyzing common precipitates between all TEM micrographs taken over the 10 min and 43 sec period. Particle morphology data is shown in Figure 4.4(c). As like the isothermal aging study performed previously, the radius of the rods is seen to increase very slowly over the aging period while the length continually grows. The measured rod radii and lengths are larger than their 200°C counterparts, indicative of the rapid coarsening rate at 300°C compared to 200°C. The volume of the particle is seen to double over the aging time and it increases at a linear rate. The equivalent volume radius (r_{vol}) cubed is also plotted to demonstrate the LSW trend in the volume as previously demonstrated at 200°C.

In addition to the isothermal study performed on the GMQ2 alloy at 200°C, the effect of higher aging temperatures was explored for a series of alloys. Baseline alloys 356 and AS7GU (356+0.5%Cu), alloy CTQ, and an additional alloy called Alloy1 were aged at 300°C for 200 hrs (after previously being held at 200°C for 4 hrs). Alloy1 is a cast alloy containing Q-phase with minimal θ-phase whose composition is not given here. TEM samples made from these alloys came from tensile specimen grips. Additionally, alloy WQ was aged at 250°C for 72 hrs and 300°C for 73 hrs, and GMQ2 was aged at 450°C for 1 hr. TEM images for all alloys were taken down the $\langle 110 \rangle_{\alpha\text{-}Al}$ zone axis, except for 356 and GMQ2. TEM micrographs for the high-temperature aging study are found in Figure 4.5 in order of increasing temperature and time.

Micrographs of WQ aged at 250°C and 300°C show Q-phase particles that are greatly different in size yet maintain a similar aspect ratio. The radius was found to be 8.5 nm and 17.7 nm and the length was found to be 376 nm and 964 nm, thus having aspect ratios of 23 and 28 at 250°C and 300°C, respectively. In the 300°C sample a Q-phase rod substantially larger than the average particle size is observed with a small zone of low number density

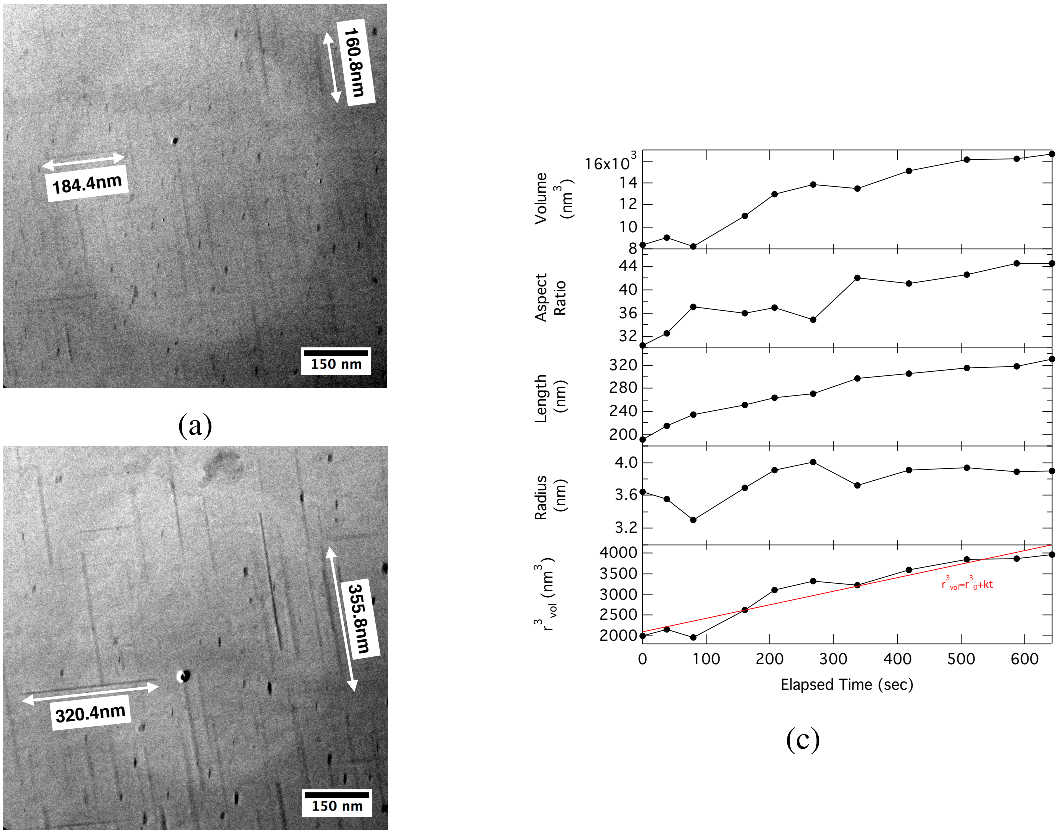

(a)

(b)

(c)

Figure 4.4: *In-situ* aging study on alloy GMQ2 aged at 300 °C (a) Image are the start of the study. (b) Image at the end of the study. (c) Data collected from the TEM image sequences.

surrounding it indicative of Ostwald ripening. Large rod shaped particles are observed in all alloy systems containing Q-phase aged at higher temperatures for long periods of time. After 200 hrs of aging at 300°C all Q-phase containing alloys, AS7GU, Alloy1, and CTQ demonstrate extremely large and misaligned rod-type particles with lengths $>1\mu m$ long, though the β-phase containing 356 alloy does not. Similarly large rod-particles are observed in the GMQ2 alloy aged at 450°C for only 1 hr. These rods are deemed to be Q-phase particles due to EDS analysis of the rods in both the Alloy1 and GMQ2 alloys demonstrating enhanced levels of Mg, Cu, and Si compared to the matrix. This re-orientation at higher aging temperatures is potentially due to a lower energy orientation, similar to that which has been observed for the θ-phase in Al-Cu binary alloys aged at 350°C [111]. It was observed that in Al-Cu binary alloys aged at 350°C θ plates are frequently observed at a different orientation from the classical θ'-phase. These re-oriented plates are theorized to nucleate independently of θ' and directly from the matrix. Much like in the high-temperature Al-Cu binary study, regular oriented precipitates are still observable in the TEM micrographs in Figure 4.5(d-f) though are much smaller than their miss-oriented counterparts.

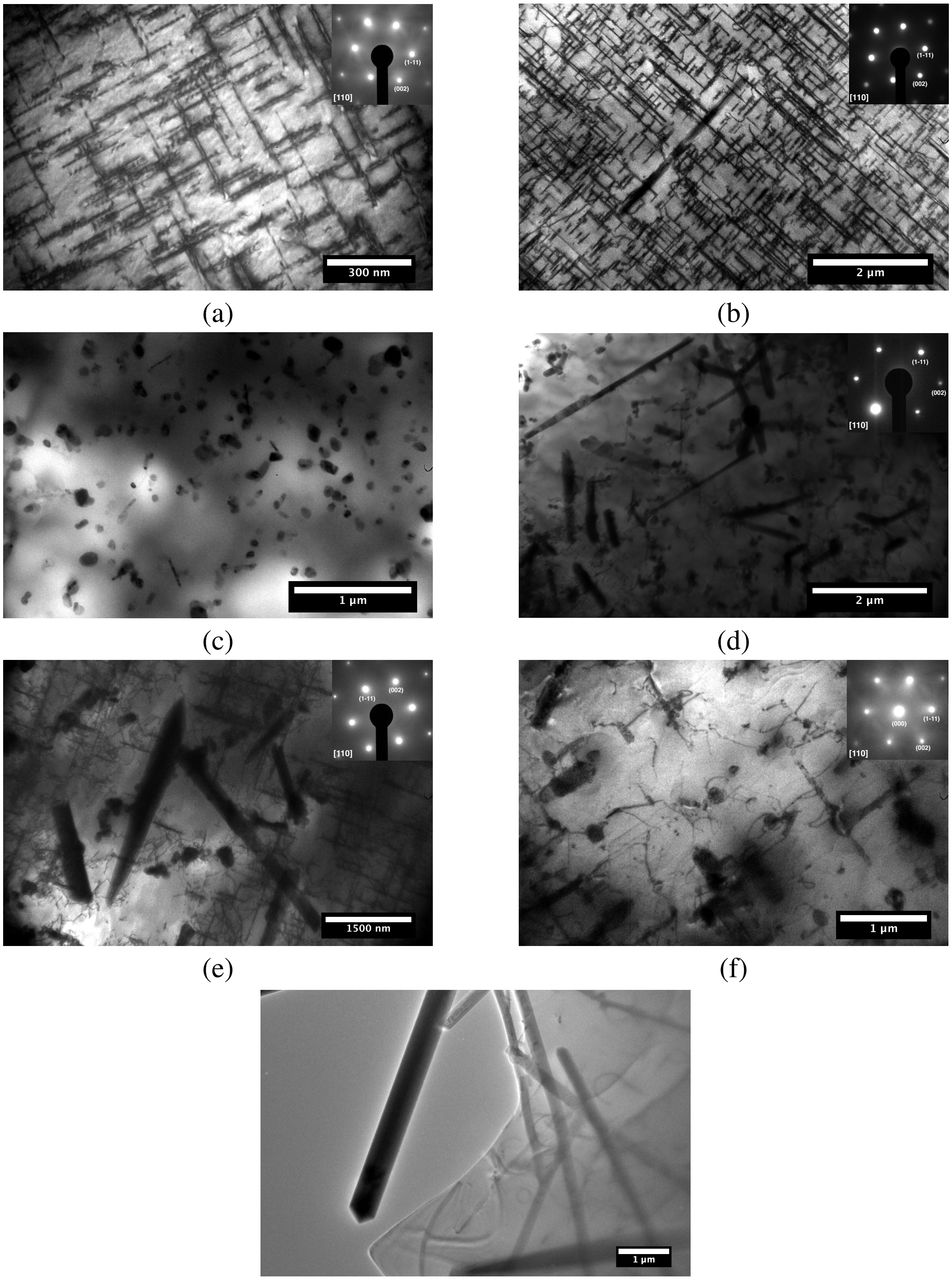

(a) (b) (c) (d) (e) (f) (g)

Figure 4.5: TEM micrographs of (a-b) WQ aged at 250°C for 72 hrs and 300°C for 73 hrs.(c-f) Alloys 356, AS7GU, Alloy1, and CTQ aged at 300°C for 200 hrs. (g) Alloy GMQ2 aged at 450°C for 1 hr.

4.3.1.2 Physical Growth Model

The coarsening theory developed by Lee et al. [103] for rod-like M_2C carbides in steels was chosen to model the rod-like Q-phase in the Al-Si-Mg-Cu system. The Lee model is presented in the following equations:

$$\overline{r}^3 - \overline{r}_0^3 = \frac{4}{9} K_r (t - t_0) \tag{4.3}$$

$$K_r = \frac{2\sigma_s V_m^\beta}{RTln(l/r)} \Phi^{-1} \tag{4.4}$$

$$\Phi = \sum_{i=2}^{n} \frac{X_i^\alpha}{D_i^\alpha} (k_i - 1)(k_i - k_1) \tag{4.5}$$

$$\overline{l}^3 - \overline{l}_0^3 = \frac{4}{9} K_l (t - t_0) \tag{4.6}$$

$$K_l = 8 A_s^3 K_r \tag{4.7}$$

where $\overline{r}/\overline{l}$ is the the average particle radius/length at time t, $\overline{r}_0/\overline{l}_0$ is the average particle radius/length at time t_0 when coarsening begins, K_r/K_l is the rate constant for the radius/length, σ_s is the interfacial energy of the side of a cylinder with hemispherical caps as shown in the Wulff plot in Figure 4.6 as from Lee, V_m^β is the molar volume of the precipitate phase β, X_i^α is the molar fraction of element i in the matrix phase at equilibrium, element $i = 1$ is the primary alloy element (in this work Al), D_i^α is the intrinsic diffusivity of element i in matrix phase α, k_i is the partitioning coefficient defined as X_i^β / X_i^α, and A_s is the equilibrium aspect ratio.

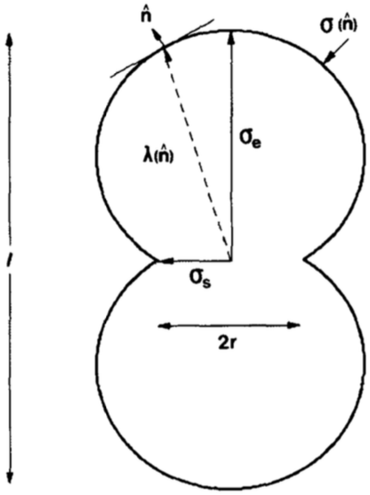

Figure 4.6: Wulff plot of a rod-type particle as from Lee [103]

The Φ term in Equation 4.5 is identical to that obtained by Umantsev and Olson [98] from the contribution for the entropy of mixing. In addition to the contribution from interactions between species, this term is the same rate constant as obtained by Philippe and Voorhees [101] for a diagonal diffusivity tensor. The Lee model could be expanded to include the total mobility tensor (M) by replacing Φ with $(\Delta\overline{C})^T M^{-1} \Delta\overline{C}$ from Philippe and Voorhees but would require the program to be linked with the thermodynamic mobility database and is beyond the scope of this work.

In application of the Lee model to the Q-phase particle, it was assumed that coarsening can be applied over all aging times, such that $t_0 = 0$. The model was found to work best when it was assumed that $\overline{r}_0 = \overline{l}_0$ at $t_0 = 0$, though it should be noted that the actual particle size can not attain this value due to the rapid growth rate of the length compared to the radius and the time delay in volume fraction increase. Since the model was to be used from the initiation of precipitation, the X_i^α term was changed to that of the fraction of element i in the matrix at the start of precipitation, and the partitioning ratios are the initial partitioning ratios (k_i) between the pre-aged matrix composition and the equilibrium Q-phase composition. All the initial matrix composition terms are determined from ThermoCalc equilibrium calculations at homogenization temperature to take into account Si eutectic formation that is inherently present for high Si containing alloys. Thus for wrought alloys the initial matrix composition is that of the bulk.

Calibration of the model was performed over all alloy measurements taken for the Q-phase in this work and for various Q-phase measurements found in literature for a total of 96 measurements for aging temperatures ranging from 175°C to 300°C. Calibration was performed for σ_s and r_0 with the equilibrium aspect ratio (A_s) taken to be 20, similar to that tended to by the Q-phase measured in this work. The mean average error (MAE) was minimized and the Pearson correlation coefficient (PCC) between the measured and predicted model values was found to be closest to one for an interfacial energy (IFE) of 3.1 J/m^2 and a critical radius of 2.1 nm. The chosen IFE is very large and un-physical considering the Q-phase has a coherent interface with the matrix due to the low misfit between the $\langle 11\bar{2}0\rangle_Q$ and $\langle 510\rangle_\alpha$ of $\sim$0.7% [38]. DFT calculations performed by Kyoungdoc Kim for this Q/α-Al interface have resulted in an interfacial energy of 0.52 J/m^2 which is in agreement with the experimentally observed misfit. The high IFE would also imply that the cap of the rod has a much larger IFE as implied by the Wulff plot. Though it may be large, the IFE of 3.1 J/m^2 is necessary to achieve the rapid growth of the radius at higher temperatures and the length. The calibrated critical radius of 2.1 nm is in good agreement with the extrapolated critical radius as determined from the Gibbs-Thomson plot for the GMQ2 alloy.

The LEE model results are plotted in Figure 4.7 as the measured radius and length vs the predicted radius and length. The radius output of the Lee model is found in Figure 4.7(a). The predicted radius is found to have a MAE of 1.52 nm and a PCC of 0.95,

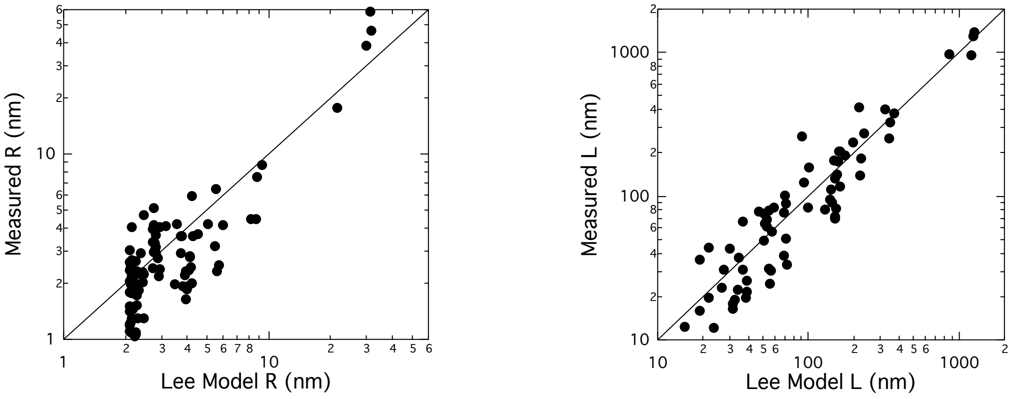

(a) (b)

Figure 4.7: Measured vs predicted (a) radius and (b) length for the Lee model.

thus indicating a high degree of correlation between experiment and the model. The model is unable to predict a radius less than the critical radius chosen. There is a fair amount of scatter between the measured radius and the model though this can partially be attributed to the difficulty in obtaining accurately measurements. The models ability to predict the large average radius as measured at high temperatures is a testament to the models success. The length output of the Lee model is found in Figure 4.7(b). The predicted length is found to have a MAE of 36.8 nm and a PCC of 0.98, indicating a very high degree of correlation between experiment and the model. With the extremely large length scales the MAE is quite small. The models ability to again predict the extremely large lengths >1 μm observed at higher temperatures is an indication of the models successful depiction of coarsening.

It should be noted that the Q-phase rod radius and length was also modeled using the machine learning code as will be discussed for the θ-phase. Due to the nature of machine learning the output model has no physical interpretation. It was found that for certain compositions and temperatures particle radii would shrink rather than grow and sometimes be non-existent. Unlike the machine learning code the physical model is continuous across all composition and temperature ranges as well as an increasing function with aging time.

4.3.2 θ'-Phase Particle Evolution

The evolution of the θ'-phase was observed in the presence of Q-phase. APT reconstructions for an isothermal aging study of the WTQ alloy demonstrates heterogeneous precipitation of the platelets on the Q-phase rods after an extended incubation time. In addition the θ'-plates are seen to be impeded by the rods leading to strange geometries. The θ'-phase growth and coarsening in then modeled using machine learning.

4.3.2.1 APT and TEM Particle Measurements

An isothermal aging study was performed on the Q-phase and θ'-phase containing WTQ alloy. This alloy after 72 hrs of aging is measured to have a phase fraction of 0.9% Q-phase and 3.1% θ'-phase and is an ideal alloy to observe the competition between the two phases. The low Si content allows for larger APT wire-specimens to be made and in general more data to be obtained. The WTQ alloy was aged at 200°C for 20 min, 1 hr, 24 hrs, and 72 hrs. APT was run on all samples and 3-D reconstructions are shown in Figure 4.8.

After 20 min of aging at 200°C the WTQ alloy only displayed Q-phase precipitation. A 7% Mg+Si iso-surface (purple) is used to visualize the Q-phase rods in Figure 4.8(a). The rod have a radius $\sim$2.44 nm and a length of $\sim$23.2 nm for an aspect ratio of 5.3. Upon further aging θ'-phase platelets were first observed in the 1 hr aged sample. Figure 4.8(b) shows a small volume subsection from the APT run to demonstrate the precipitation of the plates on the Q-phase. The top image shows the Q-phase rods using an 7% Mg+Si

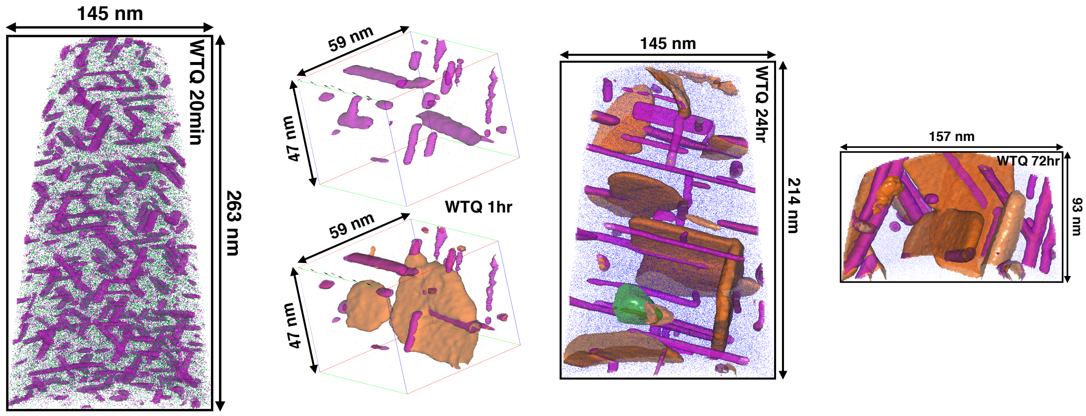

(a) (b) (c) (d)

Figure 4.8: 3-D APT reconstructions for alloy WTQ aged at 200°C for (a) 20 min, (b) 1 hr, (c) 24 hrs, and (d) 72 hrs.

iso-surface. The bottom image shows θ' platelets nucleating on the rods using a 5.5% Cu iso-surface. Previous reports of θ'-phase precipitation in the presence of Q-phase rods by Biswas et al. described the θ'-platelets as nucleating after Q-phase using both DSC analysis and APT reconstructions with the θ'-phase nucleating on the Q-phase which is consistent with the isothermal aging study on the θ' and Q-phase containing alloys in this work. All multi-phase alloys demonstrate θ' platelet formation after the precipitation of Q-phase rods and all plates have been found to be in contact with the Q-phase. This suggests that the θ'-phase forms via heterogeneous nucleation on the Q-phase rods after the rods have nucleated. In addition the Q-phase has already reached the equilibrium phase fraction of 0.9% while the θ'-phase at this aging time has nucleated only 0.88%, compared to the equilibrium phase fraction of 3.1%, suggesting a longer incubation time for the precipitation of the θ'-phase to occur.

Upon further aging of the WTQ alloy for 24 hrs as shown in Figure 4.8(c) the θ'-phase plates and the Q-phase rods have grown with the θ' volume fraction exceeding that of the Q-phase. At this aging time the θ' phase fraction is 3.06%, essentially that of the equilibrium phase fraction. In the 3-D reconstruction of the 24 hr sample the Q-phase is shown using a 8% Mg+Si iso-surface and the θ'-phase using a 7% Cu iso-surface. As can be seen the θ'-phase plates can be pinned by the Q-phase rods and other θ' plates, resulting is 90° angles and rectangular shapes. This is in contrast to the more disk-like precipitation seen at the earlier aging time at 1 hr and that found in Al-Cu binary alloys [112]. The sharp angles and rectangular shapes are also seen in TEM images for alloys containing both Q-phase rods and θ' plates as previously shown for example in the CTQ 72 hr micrograph in Chapter 3. Further aging of the sample for 72 hrs results in larger precipitates with θ'-phase plates continuing to be bound and engulfing Q-phase rods as shown in Figure 4.8(d) with the Q-phase iso-surface of 5% Mg+Si and the θ'-phase surface of 5% Cu.

4.3.2.2 Machine Learning Shape Model

The θ'-phase growth and coarsening was modeled using the machine learning software MAGPIE. Unlike the cylindrical rod with spherical caps the relevant flux equations and Gibbs-Thomson equation are not readily available for a disk. As such, using data collected as part of the APT and TEM results performed in ths work as well as data collected from the literature a ML model was generated to describe the diameters and lengths of the plates as function of aging time, temperature, and alloy composition. Details of the input data, function expanders, regression techniques, and ML code output models are presented in Appendix A.

The predicted results of the ML model are compared to the measured values in Figure 4.9. The thickness output is found in Figure 4.9(a). The predicted thickness is found to have a MAE of 0.691 nm and a PCC of 0.96 indicating a high degree of correlation between experiment and model. The model accurately predicts the large thicknesses observed at higher aging temperatures and times. The diameter output is found in Figure 4.9(b). The predicted diameter is found to have a MAE of 17.26 nm and a PCC of 0.937 indicating a good correlation between experiment and the ML model. On average the model slightly under predicts the plate diameter at higher temperatures and longer aging time but is found to fit very well for shorter diameters. Overall the ML model accurately describes the growth and coarsening observed for θ'-phase plates.

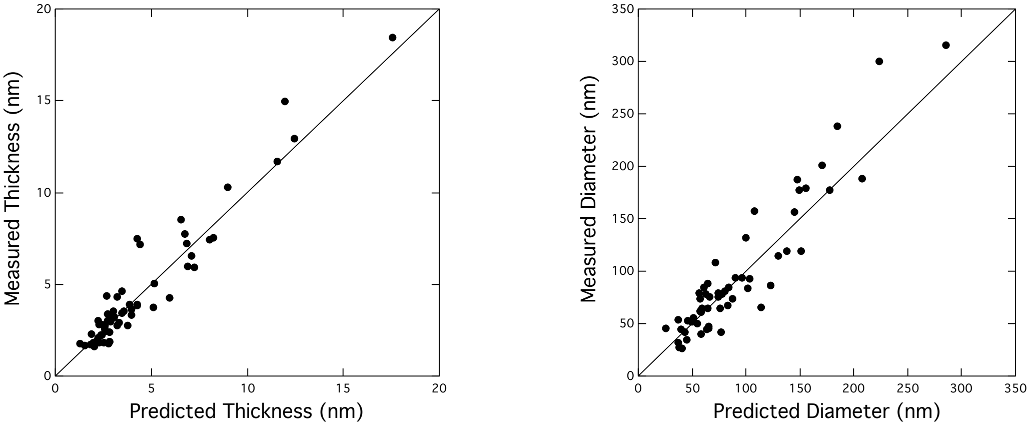

(a) (b)

Figure 4.9: Measured vs predicted (a) thickness and (b) diameter for the ML model.

4.4 Conclusions

The evolution of the Q-phase and θ'-phase was explored using APT and TEM analysis. Isothermal aging studies performed on the GMQ2 alloys demonstrate the slow rate of rod radius increase compared to the length. The radius and length increased in such a way that the volume of the particles increased linearly with time. Converting the particle volume to an equivalent spherical radius demonstrated that the volume increase followed the asymtotics of classical LSW theory as so did the number density decrease. *In-situ* TEM aging study performed as 300°C corroborated these results as observed continuously. The evolution of the matrix compositions was found to follow the Gibbs-Thomson linear trend as a function of the inverse volume radius and used to predict a critical radius of nucleation. At high aging temperatures ≥300°C the Q-phase was found to exhibit misalignment from the $\langle 100 \rangle_{\alpha\text{-}Al}$ observed at lower aging temperatures. The re-orienting of the rod particles is due to a lower energy orientation preferred at the higher temperature similar to that observed in Al-Cu binary alloys for the θ-phase aged at 350°C.

The Q-phase rod-like particle was modeled using the Lee et al. coarsening model. The model inputs were adapted to accurately depict particle evolution from nucleation through coarsening. Calibration of the model resulted in an interfacial energy much larger than physically possible and against experimental observations demonstrating a coherent orientation relationship with the α-Al matrix. The calibrated critical radius was found to be in agreement with the extrapolated critical radius from the Gibbs-Thomson plot for the GMQ2 alloy isothermal aging study. The model accurately describes the radius and length evolution over all aging temperatures and times.

θ'-phase interaction with the Q-phase was observed in the WTQ alloy using APT reconstructions. It was shown that the Q-phase precipitates first at an early aging time ~20 min. The θ'-phase was not observed until 1 hr of aging at 200°C. The θ' plates nucleated on Q-phase rods and exhibit a disk like morphology. θ' plates observed in all alloys as part of the study were found to exhibit heterogeneous nucleation on the rod particles when the Q-phase was present, contrary to the co-precipitation previously suggested in literature. In addition the Q-phase rods are shown to pin the growth of the θ' plates causing 90° interfaces and rectangular shapes in contrast to the disk-like morphology found in Al-Cu binary alloys.

After an extensive literature search for θ'-phase particle measurements the data collected was used as training data in a machine learning model. The machine learning model was used to create functions to predict the thickness and diameter separately as a function of aging time, temperature, and bulk alloy composition. The model was found to describe the evolution of the plate accurately, though no physical meaning is contained in such a model. The advantage of machine learning is the ability to create a function for a given property with only the existence of large enough data sets. The advantage of a physically based model is evident due to the potential break-down of machine learning fits outside the bounds of the training data set. The expansion of a general theory of coarsening from spheres to disks is of great interest and would require the relevant flux equations and Gibbs-Thomson capillary effect.

5 Strengthening in Aluminum Alloys

5.1 Background

High-strength Al alloys achieve their maximum strength through precipitation hardening predominantly involving rod and plate-shaped precipitates formed on rational $\{100\}_{\alpha\text{-}Al}$ and $\{111\}_{\alpha\text{-}Al}$ habit planes [36, 113, 114]. Established theories of precipitation strengthening treat random dispersions of spherical particles where a classical isothermal aging response is attributed to competing modes of shearing and bypassing of particles by dislocations. Strengthening due to dislocation bypassing or looping of dispersed particles is described using the Orowan equation [115, 116] to predict the critical resolved shear stress increment (ΔCRSS, $\Delta\tau$) which has the following form:

$$\Delta\tau = \frac{\beta G b}{2\pi M \lambda_r} ln\left(\frac{R}{r_0}\right) \tag{5.1}$$

where G is the shear modulus of the matrix, λ_r is the spacing between particles that have a regular distribution, β is the ratio of ΔCRSS of alloys containing randomly distributed particles and regular distributed particles, M is a constant relating the line tension of a dislocation, and R and r_0 are the outer and inner cutoff radius of the dislocation. Previous work by Nie, Muddle, and Polmear [117, 118, 119] explored the effects of precipitate shape and orientation for $\{100\}_{\alpha\text{-}Al}$ and $\{111\}_{\alpha\text{-}Al}$ plates, and $\langle 100\rangle_{\alpha\text{-}Al}$ infinite rods by modification of the Orowan equation. The primary contribution from their work is the development of the λ_r inter-particle spacing term re-derived for the appropriate orientation and shapes considered.

In addition to precipitation strengthening, Al alloys demonstrate considerable solid solution strengthening (SSS) from elements such as Mg, Cu, and Si. The hardening potential for SSS in Al is typically based on the Labusch weak-pinning model concentration power law [64, 120, 121, 122, 123] expressed as:

$$\sigma_{SSS} = \sum_j k_j C_j^{2/3} \tag{5.2}$$

where C_j is the concentration of a specific alloying element in solid solution and k_j is the corresponding scaling factor. Though scaling factors have been found that work well at room temperature, this form of SSS has no temperature dependence. Quantitative SSS predicitons based on the Labusch discription of dislocation-solute interaction have been developed for aluminum alloys by Leyson et al. [54, 124] to describe strengthening observed at cryogenic temperatures, but has been found to give a negligible SSS contribution at temperatures greater than room temperature contrary to previous studies.

In this work an age hardening model has been developed to describe the evolution of the yield strength as a function of aging time, temperature, and test temperature for aluminum alloys with rod and plate-type precipitates. The Orowan equation has been modified for finite rods oriented down the $\langle 100 \rangle_{\alpha\text{-}Al}$ as a function of both radius and length. In addition to the plate modified Orowan equation from Nie et al. a comparison between spheres, plates, and rods is performed based on two sets of assumptions. Orowan strengthening has been expanded to include test temperature dependence through incorporation of the particle growth models presented in Chapter 4 and temperature dependent matrix shear modulus.

Evolution of the volume fraction of the Q- and θ'-phases with respect to aging temperature and time is included through the use of the Shercliff process model [125]. Only the dislocation bypass mechanism has been considered for the rod and plate-type particles.

In addition to precipitation strengthening the developed strengthening model includes temperature dependence for base aluminum yield strength, SSS, and Si eutectic strength enhancements. The SSS has been incorporated for Mg, Si, and Cu additions to the aluminum system using the Feltham trough model [126, 127, 128, 129, 130, 131, 132]. The trough model has been shown to accurately describe SSS over a wide range of temperatures for many types of alloy systems including: Al-alloys, Ta-alloys, Nb-alloys, Cu-alloys (including brass), Ag-alloys, Mg-alloys, and Fe-alloys. The trough model has been calibrated for the Al-Mg binary system and traditional scaling factors have been considered for Cu and Si contributions. The Si eutectic contribution has been estimated using a rule of mixture (ROM) Reuss model for the Young's modulus [133] where the temperature dependence is incorporated in the Young's moduli of the matrix and Si phases.

The developed strengthening model is then compared with experiment yield and hardness measurements. The model has no variable calibration terms between different alloy systems and uses CALPHAD calculated phase equilibria and process variables as input parameters. The model is found to agree well with experiment particularly at long aging times and high temperatures. The model is then used in conjunction with CALPHAD to map the compositional space of interest to explore new regions for alloy development.

5.2 Methodology

5.2.1 Experimental Methods

Tensile and Vickers hardness tests were performed to collect both room temperature and high-temperature yield strength data. Tensile tests were performed by General Motors as described in Chapter 2. All tensile specimens were aged at 200°C for either 4 or 5 hrs to peak strength, then conditioned at the testing temperature for 200 hrs. This was done for each of the coarse, medium, and fine SDAS microstructure sections from the chill cast plates. All data presented in this work is from the fine SDAS microstucture. Hardness measurements were performed at Northwestern, General Motors, and QuesTek as described in Chapter 2. All hardness measurements were performed at room temperature after artificial aging. In addition to the experiments performed in this work, an extensive literature review was performed to gather strengthening data for β', Q, and θ'-phase containing alloys. In total 391 individual data points corresponding to unique compositions, aging times, and temperatures were gathered from experiment and literature.

5.2.2 Computational Methods

Input data for the developed strengthening model was generated using the QTDB with ThermoCalc 2015b or newer. For each of the 391 unique datapoints an equilibrium calculation was performed to determine the equilibrium α-Al FCC matrix composition, as well as the equilibrium phase fractions for the matrix, β, Q, θ, and Si phases. An additional equilibrium calculation was performed for each of the high Si containing cast alloys at the homogenization temperature to determine the initial matrix composition after homogenization due to the presence of Si eutectic present after casting. The Q-phase composition was input as a constant composition of 19.51 Al- 12.21 Cu- 41.45 Mg- 26.83 Si at.% for input into the Lee growth model unless otherwise specified. The strengthening model was programmed in MATLAB. The program was written to read the aging time, aging temperature, test temperature, bulk composition, initial matrix composition, equilibrium matrix composition, equilibrium phase fractions, and the measured yield strength to compare against as the input parameters. The model assumed that the β'-phase rods behaved like those of the Q-phase. The model used the β phase fraction to calculate any strengthening increment from the β'-phase rods at early aging time using the B' (Cu-free) composition measured by APT as discussed in Chapter 3 to determine growth kinetics from the Lee model. The model output included the particle sizes, current volume fractions, individual strength contributions from base strength (including Si eutectic), SSS, precipitation, and the total strength. In addition the model compares the predicted strength to the measured strength and outputs the mean average error (MAE) and the Pearson correlation coefficient (PCC) between the two.

Isotherm phase fields were calculated using the QTDB database with ThermoCalc 2015b to use as input into the strengthening model to create a strength map of the phase region. A grid of 20 by 20 equilibrium calculations across Mg and Cu concentrations was generated using a MATLAB script to generate and run ThermoCalc macro files. In this case the Q-phase composition was also input using the composition determined from ThermoCalc. No β'-phase strengthening was included in the maps, just θ' and Q-phase strengthening. The strength maps also include base strength and SSS contributions. The maps are created using MATLAB to plot contour lines of constant yield strength and the phase field boundaries are then overlayed as determined from the isotherm plots at the given aging temperature.

5.3 Results and Discussion

5.3.1 Shape and Orientation Dependence in Particle Strengthening

Nie, Muddle, and Polmear [117, 118, 119] explored variations of particle shape and orientation on the Orowan strengthening effect by deriving the appropriate inter-particle spacing (λ) using ration orientations for $\{100\}_{\alpha\text{-}Al}$ and $\{111\}_{\alpha\text{-}Al}$ plates as a function of diameter and thickness, and $\langle 100\rangle_{\alpha\text{-}Al}$ infinite rods as a function of diameter. To fully understand the strengthening effect of rods this work has derived an appropriate version of the Orowan equation for finite rods taking into account both rod diameter and length. It is important to consider for example two rods growing 90° from each other but existing in the same plane. As these two rods begin to lengthen the particles tips move toward each other, thereby changing the effective inter-particle spacing. As such it is the goal of this derivation to incorporate the lengthening effect, such that when L$\gg$r it approached the solution of Nie et al. for an infinite rod and such that when L$\approx$2r it approaches that of a sphere.

The derivation that is presented follows that of Nie et al. [117]. For $\langle 100\rangle_{\alpha\text{-}Al}$ oriented rods of uniform diameter D (2r) and length L the angle between the rod axis and the normal to the $\{111\}_{\alpha\text{-}Al}$ slip plane is 54.74°. If N_V and P represent the number density of precipiate rods per unit volume and the probability that a $\langle 100\rangle_{\alpha\text{-}Al}$ precipiate rod is intersected by a $\{111\}_{\alpha\text{-}Al}$ plane, respectively, then according to Fullman [134]:

$$N_A = N_V P = N_V L cos(54.74°) \quad \text{and} \tag{5.3}$$

$$f = N_A S_P = N_V L cos(54.74°) S_P = N_V V = N_V 2\pi r^3 \left(A_S - \frac{1}{3} \right) \tag{5.4}$$

where N_A is the number per unit area, f is the volume fraction of the precipitate phase, V is the volume of a single rod (taken as the volume for a cylinder with hemispherical caps), and S_P is the mean planar cross-sectional area of a precipitate rod intersected by a $\{111\}_{\alpha\text{-}Al}$ plane. Therefore $S_P = (\pi r^2 - (2/3)\pi r^3/L)/cos(54.74°) = 1.732\pi r^2(1 - D/(3L))$.

Assuming that the $\langle 100\rangle_{\alpha\text{-}Al}$ rods are distributed at the center of each surface of a cubic volume in the matrix phase, Figure 5.1(a), then the $\langle 100\rangle_{\alpha\text{-}Al}$ rods intersected by a $\{111\}_{\alpha\text{-}Al}$ slip plane will have a triangular distribution on that slip plane, Figure 5.1(b). The cross-section of the precipitate rods in the slip plane has an ellipsoid shape, with major axis of $D/cos(54.74°) = 1.732D$. Approximating this ellipsoidal area by a circle of diameter D_P, then $D_P = \sqrt{1.732}D$. Given the triangular distribution the mean planar center-to center distance (L_P) between the $\langle 100\rangle_{\alpha\text{-}Al}$ rods is given by:

$$L_P = \frac{1}{\sqrt{\frac{\sqrt{3}}{2}N_A}} = \frac{1.075}{\sqrt{N_A}} = \frac{1.075}{\sqrt{f/S_P}} = 1.075\sqrt{1.732\pi r^2\left(1 - \frac{D}{3L}\right)\frac{1}{f}} \tag{5.5}$$

and therefore, the mean planar end-to-end distance (i.e. effective inter-particle spacing), λ, between the precipitate rods is given by:

$$\lambda = L_P - D_P = 1.075D\sqrt{0.433\pi\left(1 - \frac{D}{3L}\right)\frac{1}{f}} - \sqrt{1.732}D \tag{5.6}$$

The mean particle spacing for infinite rod shaped particles (L≫r) with a $\{111\}_{\alpha\text{-}Al}$ slipe plane as derived by Nie et al. [117] is given by:

$$\lambda = L_P - D_P = 1.075D\sqrt{0.433\pi\frac{1}{f}} - \sqrt{1.732}D \tag{5.7}$$

It can easily be seen that for a given radius (r) and volume fraction (f) in the limit of

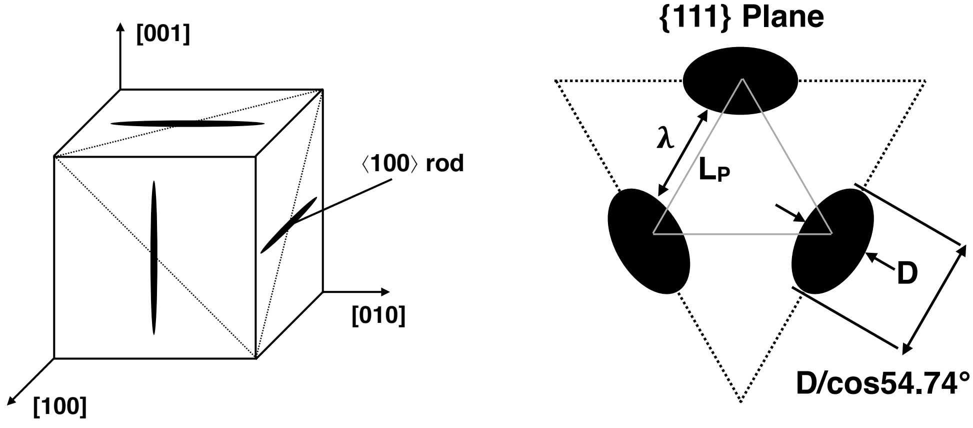

(a) (b)

Figure 5.1: (a) Distribution of the $\langle 100\rangle_{\alpha\text{-}Al}$ rods in a cubic volume of aluminum matrix phase. (b) Projection of the intersected rods on a $\{111\}_{\alpha\text{-}Al}$ plane of the matrix.

$l \to \infty$ that Equation 5.6 approaches that of Equation 5.7. The appropriate version for the mean particle spacing for spherical particles with a $\{111\}_{\alpha\text{-}Al}$ slip plane is given by [117]:

$$\lambda = (0.528\sqrt{\frac{2\pi}{3}} - \frac{\pi}{4})D \tag{5.8}$$

For a given radius (r) and volume fraction (f) in the limit of $L \to D$ Equation 5.6 is found to approach that of Equation 5.8 with a diameter $D_P = \sqrt{1.732}D$ as defined for the elliptical cross-section of the rod particles, though due to the differing definitions of the probability of the precipitates intersecting the slip plane they do no converge to the same point. The appropriate version for the mean particle spacing for $\{100\}_{\alpha\text{-}Al}$ plates with a $\{111\}_{\alpha\text{-}Al}$ slip plane is given by [119]:

$$\lambda = 0.931\sqrt{\frac{0.306\pi DT}{f}} - \frac{\pi D}{8} - 1.061T \tag{5.9}$$

where D is the diameter of the plates (assumed as circular disks) and T is the thickness of the plates. The additional term found in Equation 5.9 is due to the rectangular cross-section the disk forms in the $\{111\}_{\alpha\text{-}Al}$ plane, where both the diameter (D) and the thickness (T) can vary independently to change the particle spacing.

The effect of precipitate shape on particle spacing and Orowan strengthening is compared using two different set of assumptions: that for the complete control of shape, and for fixed radii/thickness. The Orowan equation used to calculate the precipitation strengthening is found in Equation 5.1. For this comparison the β ratio of random and regular distributions is taken to be one. The factor M is taken to be the geometric mean of the dislocation line tension of edge and screw dislocations $M = (1 - \nu)^{1/2}$ where $\nu = 1/3$ is the Poisson's ratio for aluminum. The inner cutoff radius r_i is taken to be the burgers vector $b = 0.286\ nm$ for aluminum. The outer cutoff radius R is taken as the harmonic mean between the effective average diameter (D_{eff}) of the precipitates and the mean particle spacing λ such that $R = (D_{eff}^{-1} + \lambda^{-1})^{-1}$. The harmonic mean has been shown using dislocation dynamic simulations to give the best fit in both situations when $\lambda \gg D_{eff}$ and $D_{eff} \gg \lambda$ [135, 136, 137]. For the case of spherical particles the effective particle diameter is the same as the particle diameter. For the case of rods the effective diameter is that of the approximation of the ellipsoidal area by a circle of diameter $D_{eff} = \sqrt{1.732}D$ where D is the true particle diameter. For a plate, due to the rectangular cross section in the slip plane, it is difficult to define the effective radius, though it has been shown using dislocation simulations of linear obstacles that the geometric mean of the diameter and thickness $D_{eff} = (DT)^{1/2}$ gives results that agree well with experiment [119, 137, 138]. The use of the geometric mean for D_{eff} and the harmonic mean for R implies that for plate obstacles with rectangular cross-sections in the slip plane R is close to λ when λ is much larger than the planar diameter D and that R is a function of both the planar diameter D and thickness T when D is much larger than λ.

The variation of precipitate shape on particle spacing λ and Orowan strength increment assuming complete control of particle morphology is presented in Figure 5.2. For this comparison it is assumed that the number density of the precipitates per unit volume N_V and the volume of each precipitate remains constant when the precipitate shape varies. Figure 5.2 has been plotted for a volume fraction of 2% and a constant particle volume arbitrarily defined as that of a cylinder with hemispherical caps of radius 2 nm and length 50 nm ($V \approx 611.56\ nm^3$). The particle spacing and the Orowan strengthening increment for the rods is plotted in blue, the plates in red and that of the sphere in green as a function of aspect ratio. The aspect ratio of the rod is defined $A_S = L/2r$ such that it is greater than one, while the aspect ratio of the plate is defined as $A_S = T/D$ such that it is less than one.

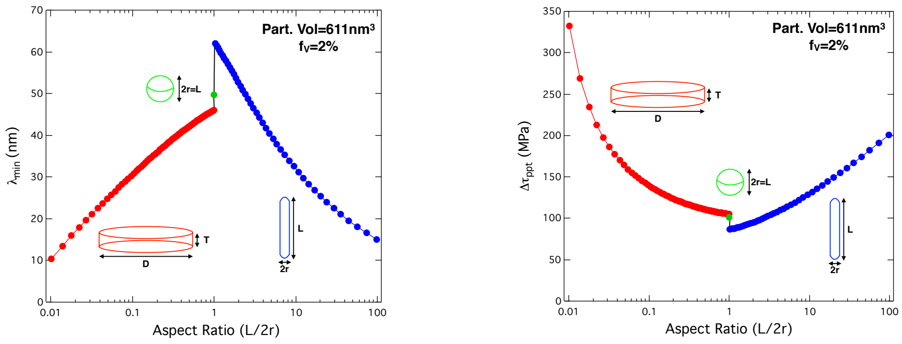

(a) (b)

Figure 5.2: Variation of (a) the mean particle spacing λ and (b) the theoretical Orowan strengthening increment (b) for rods (blue), plates (red), and spheres (green) as a function of aspect ratio for a volume fraction of 2% and constant particle volume.

As can be seen in Figure 5.2(a) the particle spacing for both the rods and plates decreases as the aspect ratios increase and decrease from one, respectively. Since the number density and particle volumes remain constant as the aspect ratio deviates from one the rod lengths and plate diameters of the particles increase and the particles approach one another. While the lengths/diameters increase the particle radius/thickness therefor decrease to maintain constant volume. As such Figure 5.2(b) demonstrates an increase in strength as the aspect ratio varies from one due to the thinning of the rods and plates compared to that of the sphere. The plate strength increment increases faster than that of a rod, with a difference of $\sim$130 MPa for an aspect ratio of 100 for a rod and 0.01 for a plate. As compared to the sphere, the particle spacing of the rods as the aspect ratio approaches one is larger than that of the sphere of equivalent volume. This is due to the larger effective planar diameter as defined previously and the different probability definitions making rods less likely to intersect a slip plane for the same radius as that of a sphere thus making the particle seperation lagger at small lengths. On the other hand the particle spacing for a plate is found to approach a value less than that of a sphere due to the definition of the in-plane particle diameters, the probability of intersection, and the additional term in the plate λ function. Assuming that complete control of the particle morphology is achievable the theoretical Orowan strength increment implies that the most potent strengthener is that of a very thin plate, followed by that of a rod with large aspect ratio, and finally spherical shaped particles. This is consistent with the results of Nie et al. [117, 118].

A second approach to considering the effect of shape on particle spacing and strengthening increment is by assuming there is no control over the particle morphology, but that the particle radius/thickness is nearly constant. This is similar to what is observed using the aging of Q-phase rods. The variation of particle spacing and Orowan strengthening increment for constant radius/thickness and constant volume fraction thus allowing the number density to vary is presented in Figure 5.3. Figure 5.3 has been plotted for a volume fraction of 2% and a constant diameter and thickness of both 4 and 8 nm. The particle spacing and the Orowan strengthening increment for the rods is again plotted in blue, the plates in red, and that of the sphere in green as a function of aspect ratio as previously defined. In addition the spacing and strengthening increment for an infinite rod as defined by Nie et al. is plotted in black and is placed at an aspect ratio of 100 for comparison.

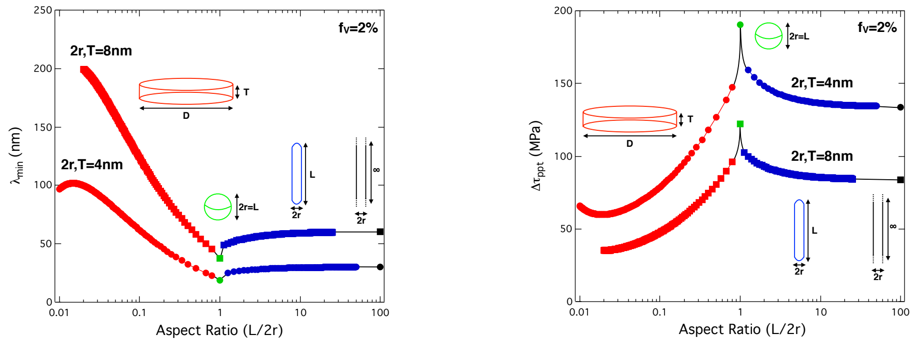

(a) (b)

Figure 5.3: Variation of (a) the mean particle spacing λ and (b) the theoretical Orowan strengthening increment for rods (blue), plates (red), spheres (green), and infinite rod (black) as a function of aspect ratio for a volume fraction of 2% and constant particle radius/thickness.

As can be seen in Figure 5.3(a) the particle spacing for the rods and plates increases as the aspect ratio deviates from one. Since the number density is no longer held constant as the particle length and diameter increase the particles take up more volume and thus the number density decreases. Though the particles are growing toward each other, the decrease in number density dominates and the average spacing between particles increases. This is consistent with classical dispersion coarsening. It should be noted that for the plate shape there is a critical aspect ratio, which is a function of plate thickness, such that due to the large plate diameters the plates begin to approach one another overcoming the loss in number density. As the length of the rod and aspect ratio become very large it is observed that the finite rod spacing approaches that of the infinite rod as mentioned previously. For a constant aspect ratio as the radius increases it is also seen that the particle spacing increases. This is again due to the large particle volume and lower number density. The particle spacing is more sensitive with respect to particle thickness for the plates than that of the diameter for both rods and spheres. The particle spacing is found to be larger for both rods and plates as the aspect ratio approaches one as expected from the definitions of effective planar particle diameter. Figure 5.3(b) demonstrates that as the aspect ratios vary from one the strengthening increment decreases for both rods and plates. The strengthening increment from spheres is found to be the greatest due to very high number density and small particle radius. As mentioned previously, the number density for the rods and plates decreases with variation of aspect ratio. The plate strength increment drops remarkable fast due to the rapid increase in volume with larger diameter, while the rod increment is comparably less due to the smaller increase in volume with length change. It is found that the strengthening increment is most sensitive to rod radius variation than that of plate thickness. The strengthening increment of the finite rod is shown to approach that of the infinite rod as defined by Nie et al. Assuming the particle morphology is not controllable and that particle morphology will vary with continued growth it is found that for a given radius the most potent strengthener is that of a sphere, followed by rods of short length, and plates of small diameter.

5.3.2 Shercliff Temperature Dependence

For precipitation strengthened alloys it is critical to model the initial precipitation kinetics from the supersaturated solid solution. The precipitation kinetics controls the rate at which the volume fraction of the precipitate phase approaches that of equilibrium and is a function of both time and aging temperature. In addition to controling the rate of precipitation it conversly affects the rate as which the solid solution strengthening decreases as precipitation occurs. In modeling the precipitation kinetics the process model developed by Shercliff and Ashby [125] has been utilized. Their model has been shown to accurately reproduce aging curves for alloys 6061+Cu, 6082, and Al-Cu binary alloys with appropriate calibration parameters for the precipitation phase. A summary of the Shercliff and Ashby model and the appropriate calibration parameters are presented for the Q and θ'-phases as used in this work.

The initial precipitation kinetics are defined in the manner of Shewmon [139] where the solute concentration in the matrix $\overline{c}(t)$ decays exponentially with time and the volume fraction $f(t)$ is directly proportional to the solute loss $c_i - \overline{c}(t)$ such that:

$$\frac{f(t)}{f_0} = \frac{c_i - \overline{c}(t)}{c_i - c_0} = 1 - exp(-t/\tau_1) \tag{5.10}$$

where f_0 is the final equilibrium volume fraction, c_i is the initial solute concentration, c_0 is the equilibrium solute concentration at the aging temperature, and τ_1 is a temperature-dependent time constant. The temperature-dependent time constant τ_1 has been defined by Shercliff and Ashby to be:

$$\tau_1 = K_1 P_p T exp(Q_A/RT) \tag{5.11}$$

where $K_1 = 0.5$ is a constant defined such that the equilibrium volume fraction and solute concentration approach their equilibrium values and is found to be a fraction of the time to reach peak strength, P_p is the peak temperature-corrected time, and Q_A is the activation energy of volume diffusion between particles. The peak temperature-corrected time P_p has been shown to be independent of aging temperature at peak aging time and is defined as:

$$P_p = (t_p/T)exp(-Q_A/RT) = constant \tag{5.12}$$

where t_p is the peak aging time for aging temperature T. As such, an appropriate plot of $ln(t_p/T)$ vs $1/T$ gives the activation energy Q_A.

The appropriate calibration terms of P_p and Q_A for the Q and θ'-phases have been taken from Shercliff and Ashby for alloys 6061+Cu and 6082. The peak temperature-corrected time for the Q-phase rods was taken to be $P_p = 2.5e{-}15\ sec/K$ and the activation energy was taken as $Q_A = 145\ kJ/mol$. The peak temperature-corrected time for the θ'-phase plates was taken to be $P_p = 5.5e - 14\ sec/K$ and the activation energy was taken as $Q_A = 130\ kJ/mol$. These values indicate the the precipitation kinetics for the θ'-phase should proceed slower than the Q-phase rods as identified by APT analysis as indicated in Chapter 4 by the longer incubation time for precipitation to occur. The peak temperature-corrected time P_p chosen for the θ'-phase for the Al-Si-Mg-Cu system is smaller than the values identified by Shercliff and Ashby for Al-Cu binary alloys. They found that for binary alloys with Cu ranging from 2.0 wt.% to 4.5 wt.% that P_p ranged from $28.5e - 13\ sec/K$ to $4.0e - 13\ sec/K$. Using these values causes the precipitation to occur much slower than observed in the quaternary system. This is possibly due to the heterogeneous nucleation that the θ'-phase exhibits in the quaternary system because of the presence of the Q-phase rods. Heterogeneous nucleation reduces the activation energy of nucleation compared to homogeneous nucleation and thus speeds up the precipitation kinetics. A more robust calibration of the Shercliff and Ashby model parameters can be undertaken by performing a hardness aging study for a range of aging temperatures.

5.3.3 Feltham Trough Solid Solution Strengthening

In Al alloys with alloying additions solid solution strengthening is a major contribution of strength particularly from elements such as Mg, Cu, and Si. As described previously, the classical Labusch power law (Equation 5.2) typically found in literature to capture SSS is independent of temperature. The original Labusch model [121, 122] is limited due to the low temperatures over which it is applicable. In this work the Feltham trough model [126, 127, 128, 129, 130, 131, 132] which is applicable to a wide range of alloy systems, concentrations, and temperatures has been applied to the predict SSS from Mg, Cu, and Si additions. The Feltham trough model is described in detail and the calibration procedure performed for the Al-Mg binary system is shown.

The trough model as originally visualized by Feltham [126] describes yielding as a consequence of the breakaway of an edge-dislocation segment from a short row of closely spaced solute-atoms which act as pinning points as shown in Figure 5.4. When the dislocation eventually breaks away it then traverses through a "trough" until it encounters more solute pinning atoms. The mean spacing between neighboring solute atoms is taken to be $b/c^{1/2}$ where b is the burgers vector and c is the concentration. Under an applied shear stress τ the maximum displacement nb, where n is the number of atomic spacings advanced of a dislocation segment of length $L = AB$ as shown in Figure 5.4, must allow for the formation of an arc (ACB) from the short-range stress field of the initial pinning points to extend the length L to a bulge ACB and permit re-pinning after reaching the saddle-point configuration. At yield, the activation energy-of-formation of the bulge ACB is found to be:

$$W(\tau) = mkT; \quad m \approx 25, \quad \tau = \tau_y \tag{5.13}$$

The energy-of-formation of the bulge may also be expressed in the relation:

$$W = W_0(x^{-1/2} - x^{1/2}); \quad W_0 = n(Uc^{*1/2}Gb^3)^{1/2}, \quad x = \tau/\tau_0 \tag{5.14}$$

where τ_0 is the CRSS as $T \rightarrow 0K$, W_0 is the work by τ_0 to move the dislocation after breakaway, U is the mean binding energy between solute and dislocation, and c^* is an effective concentration $c^* = c + c_0$ where c_0 allows semi-empirically for a solute-free "ground state" of the crystal strength. Approximating $W \approx W_0 ln(\tau_0/\tau)$ which is generally found applicable in practice [132] it can be shown that:

$$\tau = \tau_0 exp(-mkT/W_0), \quad \tau_0 \equiv 4Uc^{*1/2}/nb^3 \tag{5.15}$$

At any given temperature, the CRSS $\tau(c^*, T)$ thus depends on τ_0 and W_0 which are both functions of c^*, n, and U.

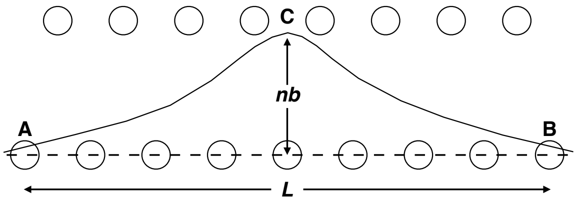

Figure 5.4: Movement of a dislocation segment between solute pinning points (circles).

An example working through the calibration process of the Fletham trough model is given for the Al-Mg binary system. Yield strength data for the Al-Mg system over temperatures ranging from 4 K to 298 K with Mg concentrations of 0.5 at.%, 1.08 at.%, 2.08 at.%, 3.11 at.%, and 4.11 at.% was obtained from Jobba et al. [140]. Firstly, because we are interested in the strengthening increment from SSS the base strength of pure Al (also measured by Jobba et al.) was subtracted out of the yield strength data for each temperature. In addition, the effective concentration c^* was taken as the true concentration of Mg setting $c_0 = 0$ eliminating the intrinsic alloy strength. The increment of yield strength σ_{SSS} is then plotted on a log-lin plot versus temperature in Kelvin and shown in Figure 5.5. The σ_{SSS} is found to follow a linear trind on the log-lin plot and the data is found to comply with Equation 5.15. The experimental data in Figure 5.5 yield W_0 on using Equation 5.15 in the form $d\,ln\,\sigma_{SSS}/d\,T = -mk/W_0$ (a.k.a the slope of the line on the semi-log plot), and σ_0 as the intercepts made on the stress axis by extrapolation. The σ_0 is converted to CRSS using the common relation $\sigma_y = 3\tau_y$ for FCC polycrystals. W_0 is found to be approximatly constant with an average value of 1.92 eV.

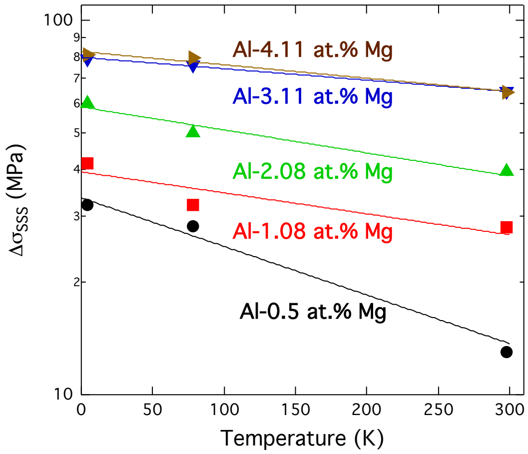

Figure 5.5: The temperature dependence of the yield-stress increment due to Mg SSS for various Mg concentrations in an Al-Mg binary alloy.

Knowing τ_0, W_0, and c^*, one can obtain n and U using the following relations which are readily obtainable from Equations 5.14 and 5.15:

$$n^3 = \frac{W_0^2}{\tau_0} \frac{4G}{(Gb^3)^2} \tag{5.16}$$

and

$$U = \frac{W_0^2}{Gb^3 n^2 c^{*1/2}} \tag{5.17}$$

where the young's modulus G is taken to be a constant 27.6 Gpa, such that $Gb^3 = 4.03\ eV$. Values for n and U are plot in Figure 5.6. Continuous functions of n and U are obtained by power-law fits in the manner of Feltham [130]. The equations obtained are as follows:

$$n = 5.8723c^{-0.156} \quad \text{and} \quad U = 0.0265c^{-0.188} \tag{5.18}$$

where the powers obtained are similar to those found by Feltham [130] for alloys of Cu-Zn with power of -0.17 and -0.19, respectively. Using the functions of $n(c)$, $U(c)$, and the constant W_0 the CRSS due to SSS can be obtained using Equation 5.15.

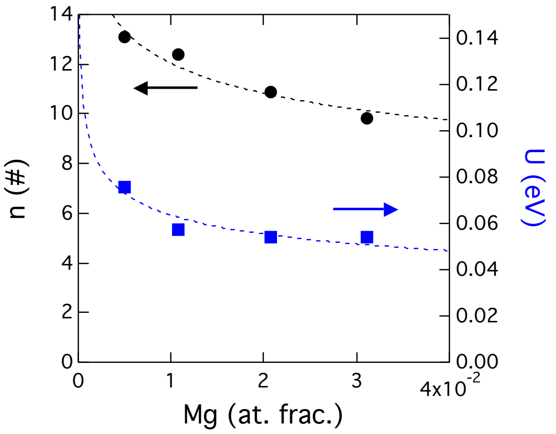

Figure 5.6: The concentration dependence of n and U as calculated using Equations 5.16 and 5.17.

Figure 5.7 plots the measured yield strength of the Al-Mg binary system as measured by Jobba et al. versus the predicted yield strength as obtained using the Feltham model. The yield strength increment due to SSS was added to the pure aluminum base strength as fit as a function of temperature from Jobba et al. to obtain the total yield strength. The calibrated Feltham trough model is found to accurately describe the yield strength due to Mg SSS strengthening with a MAE of 4.88 MPa and a PCC of 0.97.

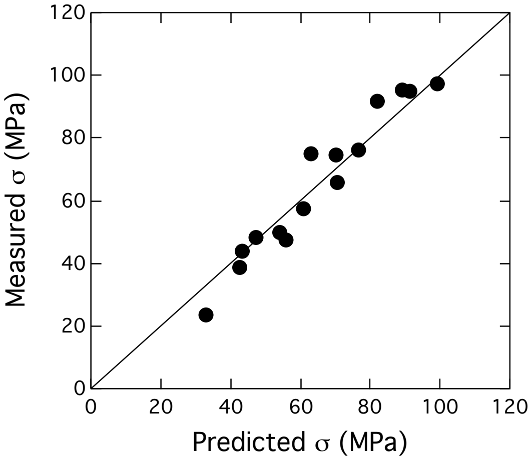

Figure 5.7: Measured versus predicted yield strength using the Feltham trough model for the Al-Mg binary system.

The lack of Al-Cu and Al-Si binary solid solution strengthening yield strength data in the literature has prevented the calibration of the Feltham trough model to these systems. The Feltham model can still be applied assuming that the classical Freidel potency/scaling factors k_j for Mg, Si, and Cu hold. The potency factors for the three elements have been reported by Mhyr et al. [64]. The potency factors in units of $MPa/wt.\%^{2/3}$ for Mg is given as 29.0, for Cu 46.4, and for Si 66.3. Since the Feltham model is defined such the the concentration is in at.% the scaling factors have been converted to at.% using their atomic weight such that in units of $MPa/at.\%^{2/3}$ the factor for Mg is ∼27.05, for Cu is

$\sim$81.45, and for Si $\sim$68.08. Scaling of the SSS increment terms using the scaling factors was determined to overestimate the amount of strengthening from both Cu and Si. This is consistant with cyrogenic tenisle test studies performed by Podkuyko and Pustovalov [141] in which they found that a SSS Al-Cu binary alloy with 1 at.% Cu provided slightly less SSS than a similar Al-Mg binary alloy with 1.4 at.% Mg, implying that the potency factors available may be incorrect and that Cu SSS behaves more like that of Mg than suggested. The best result was obtained assuming that Cu and Si both contributed equally as much as Mg on an at.% concentration bases.

To incorporate the effect of concentration evolution during precipitation the Shercliff model was used to calculate the concentrations in the matrix as they approached that of the equilibrium concentration values. The following equations were defined to capture the concentration evolution in the matrix:

$$C = C_i - (C_i - C_{eq}) \frac{\overline{f}_Q}{f_Q^{eq}} \quad \text{for Mg and Si} \tag{5.19}$$

and

$$C = C_i - (C_i - C_{eq}) \frac{\overline{f}_Q + \overline{f}_\theta}{f_Q^{eq.} + f_{\theta'}^{eq.}} \quad \text{for Cu} \tag{5.20}$$

where C is the instantaneous concentration in the matrix, C_i is the initial concentration in the matrix before aging, C_{eq} is the equilibrium concentration in the matrix, $\overline{f}_{Q,\theta'}$ are the instantaneous volume fractions of the Q and θ'-phases as calculated using the Shercliff model, and $f_{Q,\theta'}^{eq.}$ are the equilibrium volume fractions. The θ'-phase only effects the concentration of Cu in the matrix since it is a binary compound. It can be seen from these equations that as the volume fraction approaches that of the equilibrium value $\overline{f}/f^{eq.} \rightarrow 1$ and thus the concentrations approach their equilibrium values $C \rightarrow C_{eq}$. Incorporating the Fletham model and the Shercliff model allows the SSS increment to be calculated as a function of both aging time, aging temperature, and alloy composition.

5.3.4 Combined Strength of Aluminum

In order to model the yield strength of Al alloys consisting of both rod and plate type precipitates, the following contributions have been considered: precipitation hardening for both rods τ_{rods} and plates τ_{plates}, solid-solution strengthening σ_{SSS}, and intrinsic resistance to shear for pure Al σ_0. Contributions due to grain boundary strengthening have been deemed insignificant due to the large grain sizes caused during the homogenization/solution heat treatment and long artificial aging times. The base/intrinsic strength of Al is taken from a fit to the data from Jobba et al [140] and is shown in Figure 5.8. It can be seen that a linear line fits the data well, such that $\sigma_0 = -0.0196T + 16.489$ where T is in K.

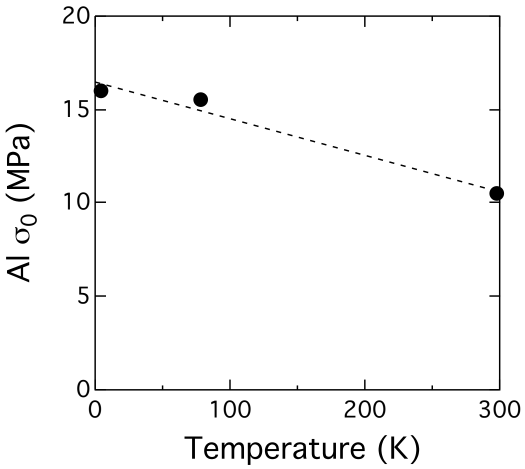

Figure 5.8: Yield strength as a function of testing temperature for pure Al.

In addition to the base yield strength of aluminum it is important to include the temperature dependence of the shear modulus G of the matrix which is assumed to be that of pure aluminum. The shear modulus is an important factor in the precipitation strengthening Orowan Equation 5.1. The fit of the elastic modulus E as a function of temperature is taken from Taleff et al. [142] and given as: $E(T) = 77,630 - 12.98T - 0.03084T^2$ where E is in MPa and T is in K. The shear modulus G is then defined as $G = E/2(1+\nu)$. In addition to defining the shear modulus it is important to consider the β term in the Orowan equation which relates random distributions to regular distributions. β is taken as 0.8 if the stress field of the dislocation is considered for rod type particles since they act as point or spherical obstacles in the slip plane [143]. For plate type particles β is found to be close to 0.78 [137]. As the obstacle strength of the Q-phase rods and θ'-phase plates to dislocation movements should be of the same order of magnitude, the quadratic superposition approximation which is considered to be a good approximation for obstacle of similar strength [144, 145, 146] is used to find the total precipitation strengthening such that: $\tau_{ppt}^2 = \tau_{rods}^2 + \tau_{plates}^2$. The total superposition law for the yield strength is given as:

$$\sigma_y = \sigma_0 + \sigma_{SSS} + M(\tau_{rods}^2 + \tau_{plates}^2)^{1/2} \tag{5.21}$$

where $M = 3.06$ is the Taylor factor describing the proportionality between yield strength and critical resolved shear stress typically taken between 3 and 3.1 for polycrystalline FCC alloys [119, 147, 148].

5.3.5 Comparison Between Theory and Experiment

The total strength model yield strength predictions are compared to hardness and tensile yield strength tests performed as part of this project and from alloy data gathered from literature. All non-process input parameters for the yield strength model are calculated from ThermoCalc equilibrium simulations using the QTDB with the measured bulk alloy compositions. The input parameters from ThermoCalc include: initial matrix composition as calculated at the homogenization temperature of the alloys, equilibrium matrix compositions calculated at the aging temperature, and phase fractions of the Q-phase, θ-phase, β-phase, and Si (eutectic). β-phase is treated as that of Q-phase (only one β containing alloy) since they both take on a rod morphology at early aging time. The model calculates the phase fraction for the Q and θ'-phases, the particle sizes, the individual precipitation strengthening increments, the solid solution strengthening, and the intrinsic strength for each aging time and temperature. The strength model relies heavily on the database used, but experimental parameters can be used if known. The model calculates the MAE and the PCC between the measured and predicted yield strengths. It should be noted that the primary strengths of this model are that there are no calibration parameters between different alloy systems i.e. no adjustment of base strength for each alloy independently or modifying the rate of precipitation kinetics between alloy systems, as well as the ability to predict strength as elevated testing temperatures.

The reliance on the thermodynamic databases for the input parameters has its weaknesses. One such weakness its the inability of the database to distinguish from primary and secondary precipitation. It is known that in high-Cu containing alloys that the θ-phase forms during solidification and is seen in this work for some alloy systems. During homogenization/solution heat treatments the θ-phase is seen to dissolve back into solution extremely slowly. As such there is considerably less θ'-phase secondary hardening in these alloys as the database would suggest if the total phase fraction is taken from the equilibrium calculations. The model will thus tend to over-predict θ' strengthening at higher Cu levels. The alloy systems considered using the strengthening model have been limited to alloys containing <2 at.% Cu. This same limitation is present in high-Mg containing alloys. β is also know to form during solidification and requires very high solution heat treatments to bring back into solution, typically high enough to cause incipient melting. The residual primary β-phase limits the phase fraction attainable by the Q-phase. In addition the model is not capable of modeling the morphological transition the occurs between β' and β leading to over predicted strengths for β-phase containing alloys. The alloy systems considered using the strengthening model have been limited to alloys containing <1.1 at.% Mg (to include alloy 6061+Cu).

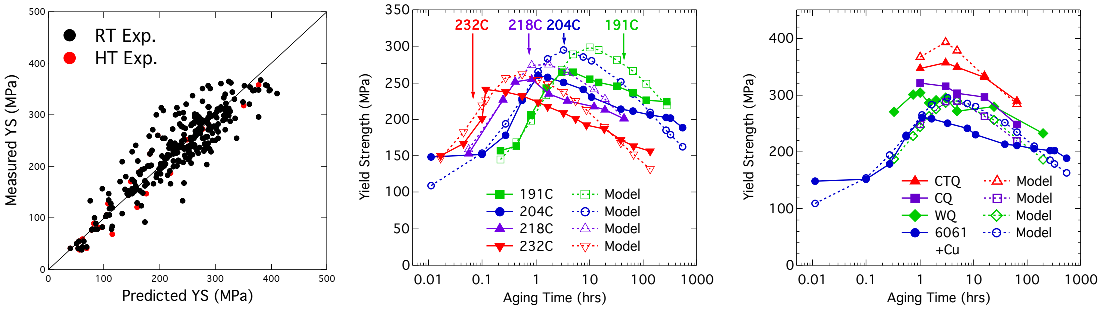

(a) (b) (c)

Figure 5.9: Comparison between experiment and predicted yield strength. (a) All experimental data versus predicted strength. (b) Data from Andersen [149] for alloy 6061+Cu compared to the model for four aging temperatures. (c) Comparison of four different alloys, two wrought and two cast with Q-phase and θ'-phase strengthening.

Figure 5.9 compares the experiential yield strengths to the predicted yield strengths from the strengthening model. Figure 5.9(a) plots the measured versus predicted yield strengths for 268 strength data points collected as part of this project and from the literature. This includes both alloys tested at room temperature (RT) and higher temperatures (HT). The MAE over the whole data set is 26.04 MPa and a PCC of 0.90. This implies there is a strong degree of correlation between the experimental results and the calculated yield strengths. Figure 5.9(b) presents data from the aging study performed by Anderson [149] for alloy 6061+Cu for a range of different aging temperatures with yield strength measurements performed at RT. The chemical composition for Anderson's commercial alloy 6061+Cu is taken as Al- 0.6 Si- 1 Mg- 0.25 Cu- 0.25 Cr wt.% as given by Song [150]. Thermodynamic equilibrium calculations using QTDB shows this composition to contain Q-phase at all aging temperatures of interest. Figure 5.9(b) demonstrates that as aging temperature increases the peak strength of the alloy drops and this is accurately accounted for in the strengthening model due to the slight decrease in the equilibrium phase fraction of the Q-phase with increasing temperature. Though the peak strength from the model is overestimated for all aging times. This can be attributed to the overestimation of the equilibrium phase fractions from the QTDB for the given composition, or perhaps an incorrect alloy composition. It can also be seen from experiment that the peak strength it attained at higher aging temperatures for shorter aging periods. This is also accurately captured by the strengthening model, though the model kinetics lag that of the experiment for all aging temperatures. Further calibration of the Shercliff kinetic parameters could lead to a more accurate peak aging times.

Figure 5.9(c) compares the experimental yield strength and the model predicted strength for four different alloy systems. The four systems chosen are: wrought Q-phase containing alloy 6061+Cu from Anderson aged at 204°C, wrought Q-phase containing alloy WQ aged at 200°C, cast Q-phase containing alloy CQ aged at 200°C, and cast Q and θ'-phase containing alloys CTQ aged at 200°C. The strength model shows the correct trends for the given alloy systems. Experimentally the peak strength for both WQ and CQ alloys is very similar and this is predicted in the model. Though the alloy 6061+Cu is lower in peak strength the model predicts a peak strength similar to alloys WQ and CQ due to the volume fraction from the equilibrium calculations being similar. All three Q-phase containing alloys demonstrate peak strength around 1 hr of aging though the model predicts peak strength around ~4-5 hrs of aging. Alloy CTQ demonstrates the largest peak strength and this is consistent with the model predictions, though the model slightly over estimates the peak strength. The peak aging time for CTQ is found to be the same between experiment and model prediction with the addition of θ'-phase strengthening. The total model shows trends consistent between various alloys for multiple aging times and temperatures without the need for calibration for individual alloy systems.

5.3.6 Model Predictions at High Temperature

High-temperature yield strength performance is crucial for good performance in the cylinder head applications of this project. The ability for strength model predictions at high testing temperatures are thus critical for the design of future alloys using ICME to minimize time consuming and expensive experiments. Figure 5.10 compares the experimental yield strength for the high-temperature tensile specimens measured at temperature versus the predicted yield strengths from the model. All tensile specimens were aged for 4 hrs at 200°C followed by conditioning at the test temperature for 200 hrs. The current growth model does not account for 2-step aging treatments. The sample tested at 150°C was modeled assuming that the 150°C tempering had little effect on the precipitate morphology after the 200°C peak age. For samples tempered greater than 200°C the peak age treatment (4 hrs at 200°C) was ignored and the particle morphology was calculated using just the 200 hr temper. This is a reasonable approximation due to the faster coarsening kinetics at high temperature and the long amount of aging time compared to the peak age treatment.

Figure 5.10(a) compares the measured tensile strength versus the predicted high-

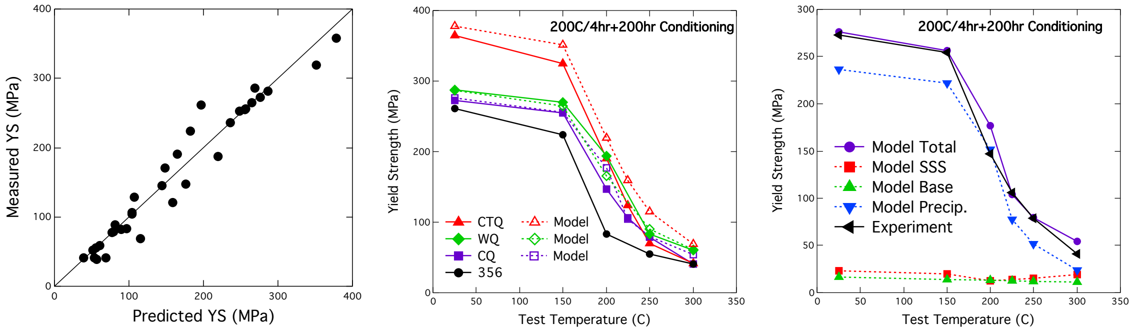

(a) (b) (c)

Figure 5.10: (a) Comparison between experiment and predicted yield strength for the high-temperature tensile tests. (b) Tensile yield strength for alloys CTQ, WQ, CQ, and 356 for aging and testing temperatures ranging from RT to 300°C. (c) Individual strengthening contributions for the CQ alloy as a function of temperature.

temperature yield strength from the model for six different alloys: 356.2, AS7GU, Alloy1 from Chapter 4, CTQ, CQ, and WQ. The raw yield strength data for these six HT alloys in addition to a very high Si containing eutectic Q-phase alloy is given in Appendix B. The MAE for these HT alloys is 18.6 MPa and a PCC of 0.97 between the experiment and model prediction. There is a near perfect correlation between the model and the experiment. Figure 5.10(b) demonstrates the temperature dependence on the yield strength for four different alloys: CTQ, WQ, CQ, and 356. Each alloy was tempered for 200 hrs at 25°C, 200°C, 225°C, 250°C, and 300°C. The yield strength model shows good agreement with the yield strength data over all aging and testing temperatures for the Q-phase and θ'-phase strengthened alloys. The model captures the trend of decreasing strength with temperature very precisely with similar drops in strength between each tempering condition. The yield strength model also correctly captures the correct ordering of alloy strength, with CTQ alloy having the greatest RT strength, followed by alloys WQ and CQ. The model is seen to slightly over predict the strength of the CTQ alloy and is most likely due to an overestimation of θ' phase fraction from the database. Like the experimental data, the predicted yield strengths converge at high tempering temperatures though in the case of CTQ and CQ the model over predicts the strength at 300°C slightly. It is important to note that the β strengthened 356 alloy is lower in YS over all aging temperatures than the Q-phase strengthened alloys demonstrating the benefit of the Q-phase for high-temperature applications. Figure 5.10(c) shows the individual contributions from precipitation strengthening, SSS, and intrinsic strength for the CQ alloy. The total alloy strength is dominated by the Orowan strengthening contribution and leads to the distinctive drop in strength with temperature. The SSS strength contribution is small due to the small amount of solubility in the matrix after precipitation, but is found to have a minimum. This minimum occurs due to the dissolution of the Q-phase at higher aging temperatures thus introducing more solute into the matrix. The intrinsic strength is very low but decreases slightly with temperature. The yield strength model is found to accurately predict strength at all aging temperatures and over a wide range of Al-Si-Mg-Cu alloy compositions. There are limitations with respect to β-phase strengthened alloys (i.e. 356.2) due to the morphological change upon aging and is beyond the scope of this work.

5.3.7 Aluminum Alloy Strength Mapping with CALPHAD

An advantage of a global strengthening model is the ability to explore the composition space for the optimization of alloy properties. The developed strength model can easily be adapted to work with CALPHAD databases to quickly map out composition regions of interest. The strength as a function of aging condition can then be mapped and trends can be identified for optimizing alloy development without the need of numerous experiments over the composition space.

ThermoCalc equilibrium calculations were performed over a range of compositions in a low 1.0 at.% Si aluminum rich corner of the phase diagram with Mg ranging from 0-1 at.% and Cu ranging from 0-1.5 at.% at 200°C and 300°C. The composition and the Q-phase was also taken into account as predicted by the QTDB database and used as input into the rod growth model. The strengthening model then calculated the total strength at each point for aging temperatures of 200°C and 300°C for various aging/tempering times. Figure 5.11 shows the predicted strengthening maps with contours of constant total yield strength for aging at 5 hrs, 200 hrs, and 1000 hrs at 200°C and 300°C, with predicted tensile tests being taken at RT, 200°C, and 300°C. The phase boundaries for the FCC+θ+Q+Si, FCC+Q+Si, and FCC+Q+Mg_2Si+Si regions have been plotted as from the isotherm at the given aging temperature.

Figure 5.11 suggests that regardless of the aging time and temperature the strength of the alloy can be increased by larger Cu and Mg additions. By comparing the figures in a single column, the effect of aging time is deduced. With longer aging times the strength decreases for any given composition, as is expected. The yield strength contours in the θ-phase containing region are found to become more horizontal with longer aging time are high Cu contents, implying that additional Mg becomes less beneficial. Comparing the first two columns the effect of testing temperature is shown. With no additional tempering between, unlike the high-temperature tensile tests performed previously, a slight drop of $\sim$25 MPa due to the testing temperature is noted across all compositions for any given aging time. A much larger drop in strength is obtained when the aging temperature and testing temperature are 300°C. At 300°C it is found that in the θ containing region for a given Mg content there is an optimal Cu level to attain a higher yield strength due to the "C" shaped curve. At 200°C it is found that for any given Mg content Cu additions result in

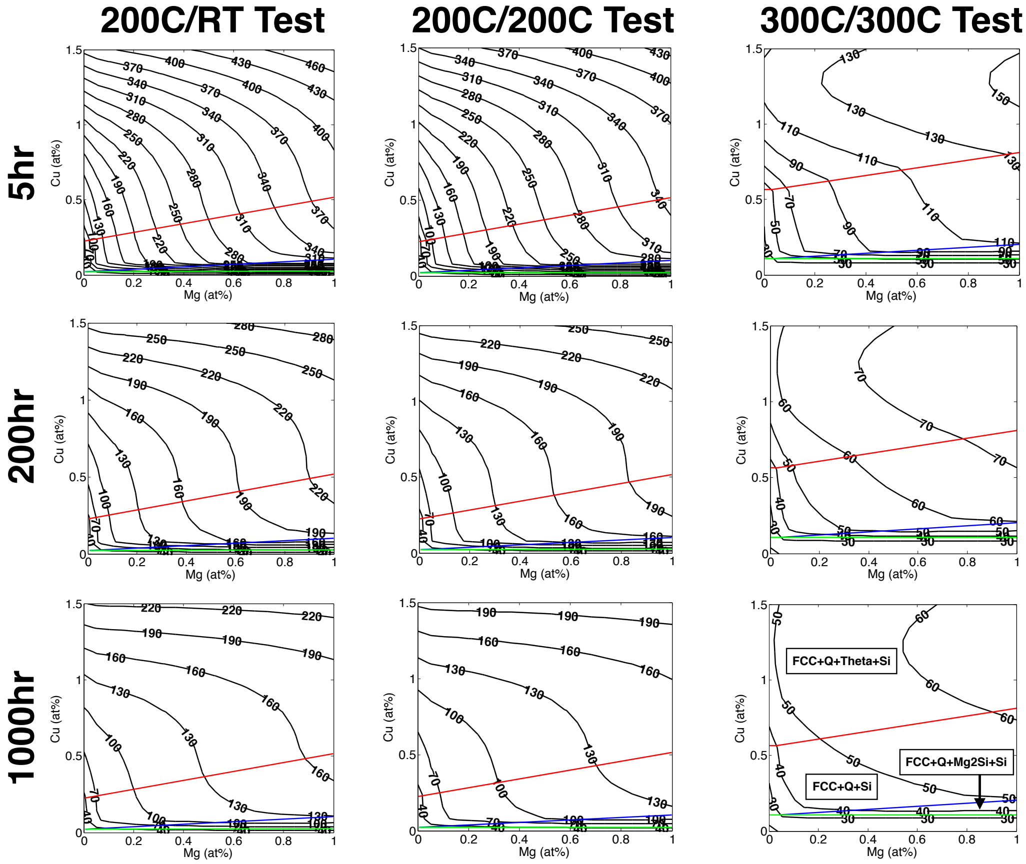

Figure 5.11: Total tensile yield strength maps over the Al- 1.0 Si- (0-1.0) Mg- (0-1.5) Cu at.% composition region.

higher yield strengths with lower returns on strength coming near the θ/Q phase boundary were the strength contours become more vertical. At long aging times at 300°C the total yield strength begins to converge across the entire composition space as is also observed in the experimental tensile results for the different alloy systems. Exploring the composition space in this way can allow for such trends to be identified and enable more informed decisions to be made that can speed up the alloy design process.

5.4 Conclusions

A general tensile yield strength model was developed by modeling shape dependent Orowan contributions, temperature dependent solid-solution strengthening, and intrinsic aluminum strength. A version of the Orowan equation for rationally oriented rod-like particles was created by deriving the particle spacing of rods in the slip plane as a function of both rod length and radius. Comparisons between the derived rod spacing and strength were compared to those for spheres and plates. It was shown that for a given particle volume a thin plate morphology contributed the most strength, followed by a thin rod, and finally a sphere. Using a different set of assumptions, for a given particle radius/thickness it was found that a sphere was the most potent strengthener, followed by a short rod, and a small diameter plate. The optimization of precipitation morphology can be undertaken to achieve desired strength.

The effect of temperature dependence on the kinetics of precipitation were incorporated using the Shercliff process model. Calibration parameters were taken from Shercliff et al. for rod and plate precipitation. Further aging study experiments can be performed to calibrate the model to achieve peak aging time with varying temperature to be more consistent with what is experimentally observed.

Solid solution strengthening was incorporated using the Feltham trough model. Using data collected from Jobba et al. the Feltham model was calibrated and shown to describe the SSS from Mg in Al-Mg binary alloys well. The addition of the Shercliff model to the Feltham model incorporates the temperature kinetic effects not only on strength increment but on the rate as which SSS reaches the equilibrium value.

The overall strengthening model describes the yield stress for many alloy systems with a fair amount of success. The overall trends with aging temperature on the kinetics and peak strength are captured by the model. The model excels in predicting the at temperature high-temperature tensile yield strength for a number of alloy systems. By incorporating the yield strength model with CALPHAD the model can be used to map strength over a wide range of compositions. This has numerous applications, from optimizing the design of alloys, predicting the effect of heat-treatment cycles, the strength effect of welds, and optimization of process parameters. Continuing work on the strengthening model can be performed to calibrate the various kinetic parameters and include Si eutectic contributions to strength. In addition, experimental tensile data for SSS increment with Cu and Si additions is lacking. SSS data for Cu and Si with respect to concentration and test temperature would enable a more detailed modeling of the overall SSS effect in these Al alloy systems.

6 Elemental Partitioning to the Q-phase

6.1 Background

Al-Si-Mg-Cu alloys show strong secondary hardening upon precipitation of the Q-phase. The Q-phase is also thermodynamically stable unlike the rod-like β'-phase which exhibits a transformation to the plate-like β-phase upon aging, thus resulting it higher yield strengths at longer aging times and higher aging temperatures. It is therefore of great interest to control Q-phase precipitation microstructure and particle morphology in these alloy systems to further optimize the Q-phase precipitate dispersion for maximum strength.

Though the Q-phase has been shown to be a potent strengthener at higher aging-temperatures the rapid growth of the rod particles, as well as θ'-plates, as discussed in Chapters 4 and 5 lead to major losses in yield strength and essentially converge at 300°C regardless of precipitate dispersion utilized i.e. Q, θ, and β-phases and volume fraction. It is of great interest then to control the precipitate dispersion microstructure such that at higher aging temperatures a fine particle dispersion can be maintained. One such way of modifying particle nucleation and growth is via solute partitioning. Studying solute partitioning is very important because solutes can influence the nucleation rate of precipitation thereby potentially leading to a finer particle dispersion, change interfacial stability via interfacial segregation thereby influencing particle morphology, and by modifying the coarsening rate of the precipitate phase.

Rapid precipitation due to fast diffusing elements can lead to a fine particle dispersion and higher strengths in Al alloys. For example, Ag additions, which has a relatively fast inter diffusion in aluminum, to Al-Mg-Cu alloys have demonstrated increased hardening rates and magnitude of strengthening [114, 151, 152]. On the other hand a slow coarsening rate is desirable for small particle sizes upon aging at higher temperatures. A close look at the coarsening rate defined by Lee et al. in Chapter 4 reveals that the total coarsening resistance is analogous to series-type electrical resistance and is controlled by the slowest moving element such that the rate controlling constant is:

$$D_i X_i^{\alpha} / \left(X_i^{\beta} \right)^2 \tag{6.1}$$

where D_i is the inter diffusion of element i in the α matrix and X_i is the concentration of element i in the α matrix and precipitate phase β. It is therefore desirable for a slow diffusing element to be energetically favorable to partition to the Q-phase to lower the coarsening rate. Relative diffusion coefficients of solute elements in aluminum are shown in Figure 6.1 as calculated at 300°C using the pre-exponential diffusivity factors and activations enthalpies as found in literature [105, 106, 107, 153, 154, 155, 156, 157, 158, 159, 160, 161]. The diffusion coefficients are arranged in order of periodic table column with individual periods connected. Elements in columns 3-10 show the slowest diffusivities and would be preferred for enhanced coarsening resistance. The element Sc which is commonly used in aerospace alloys is known to form coherent Al_3Sc precipitates that are stable against coarsening up to 350°C [162, 163] is easily captured in this representation.

Studies of Zn additions to alloy W319 using APT by Biswas et al. [31] have demonstrated significant partitioning of Zn to the Q-phase. This is currently the only known study to observe partitioning of any element to the Q-phase. This study expands the search

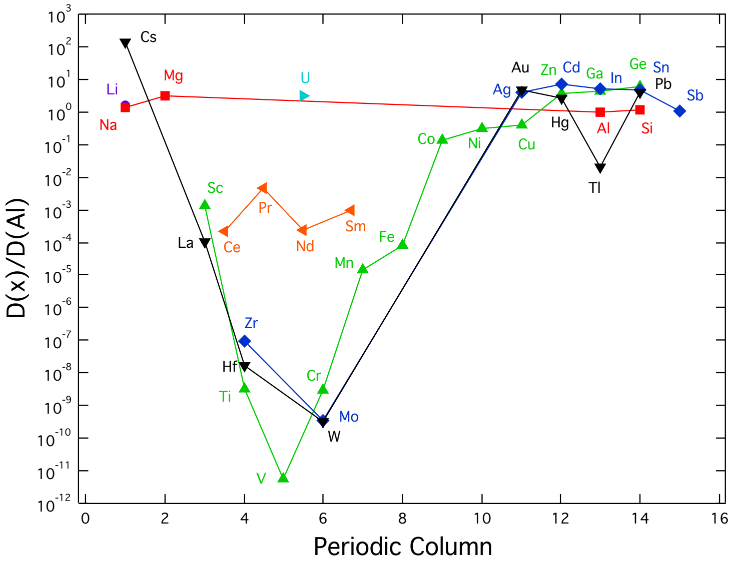

Figure 6.1: Calculated relative diffusivities at 300°C of element solutes in Al.

for solute partitioning elements to the Q-phase using DFT calculations. Solute-partitioning energies are calculated to find potentially energetically favorable elements and APT experiments of Q-phase containing alloys with these additions are used to validate the DFT calculations for 6 different elements (Zn, Ni, Mn, Ti, V, and Zr). The partitioning element effect on the theoretical coarsening rate is explored. The misfit strains for the $(11\bar{2}0)_Q||(510)_{\alpha\text{-}Al}$ interface using the DFT predicted and experimentally observed atomic-interfacial structure between the Q-phase precipitate and α-Al matrix are estimated for each of the partitioning elements.

6.2 Methodology

6.2.1 Computational Methods

First-principles DFT calculations to explore various solute-partitioning energies to the Q-phase and the lowest energy termination of the $(11\bar{2}0)_Q||(510)_{\alpha\text{-}Al}$ interface were performed by Kyoungdoc Kim using VASP as discussed in Section 2.1.3. Solute partitioning calculations were performed using a $4 \times 4 \times 4$ supercell containing 256 atoms for the α-Al matrix and a $1 \times 2 \times 3$ supercell containing 126 atoms for the Q-phase to converge energy differences to within ~0.03 eV/solute. For interfacial energy calculations a super cell of 94 and 188 atoms was used and the k-point density and supercell size were enough for convergence of the energy difference to within less than 0.15 J/m^2. Calculation of the energies for the Q$||\alpha$-Al coherent interface is determined from the total energy of a generated interface supercell and the pure bulk phases and the interfacial surface area. Details for the interfacial energy DFT calculation are not presented here.

The solute partitioning energy E_p is defined as the difference in the formation energy of the solute in the Q-phase and the formation energy of the solute in the α-Al matrix. The solute partitioning energies are calculated using the following equation:

$$\begin{aligned} E_p &= \Delta H(solute \rightarrow Q) - \Delta H(solute \rightarrow \alpha\text{-}Al) \\ &= E(solute \rightarrow Q) - E(Q) - E(solute \rightarrow \alpha\text{-}Al) + E(\alpha\text{-}Al) + \mu(x) - \mu(Al) \end{aligned} \tag{6.2}$$

where $E(solute \rightarrow Q)$ and $E(solute \rightarrow \alpha\text{-}Al)$ are the energies of the Q-phase and α-Al matrix supercells each containing one solute atom, $E(Q)$ and $E(\alpha\text{-}Al)$ are the energies of pristine supercells of Q-phase and α-Al without substitution, $\mu(x)$ refers to the chemical potential of the atom $x(= Al, Cu, Mg, Si)$ in Q which is displaced by the solute atom, and

$\mu(Al)$ is the chemical potential of an Al atom. $\mu(Al)$ is determined assuming local equilibrium between Q-phase and α-Al, resulting in the equality: $\mu(Al\ in\ Q) = E(\alpha\text{-}Al)/N$ where $N = 256$ is the number of atoms in the α-Al supercell. The other chemical potentials are based on the experimental reference phases α-Al, θ', Si, and Q. A negative value of the solute partitioning energy E_p indicates that it is energetically favorable for the solute atom to enter the Q-phase over the α-Al matrix, while conversely a positive value indicates it is energetically favorable for the solute to stay in the α-Al matrix.

6.2.2 Experimental Methods

A series of eight wrought button alloys were made using input from DFT for suggested partitioning elements. The eight alloys were based on alloy WQ with enhanced Mg. Table 6.1 shows the bulk compositions obtained using spark atomic emission spectroscopy (OES). All alloys were homogenized at 530°C for 5 hrs and water quenched. APT wire specimens were prepared as discussed in Section 2.2.6 for the wrought alloys. APT was performed in LEAP mode and analyzed using IVAS 3.6, see Section 2.2.6 for details. The isoconcentration surface used to define the Al-matrix/Q-precipitate interface was determined via projected 2-D concentration profiles of Mg+Si content perpendicular to the primary particle growth direction. The surface was chosen such that it accurately enclosed the projected 2-D concentration profile. This corresponded to a 7-8 Mg+Si at.% concentration surface. The WQ+Ba and WQ+Sr sample additions were not identified in the APT run mass spectra due to their very low alloying contents and their results are not presented.

Table 6.1: Bulk alloy chemical compositions as determined by OES.

Alloy	Si (wt.%)	Mg	Cu	Fe	Mn	Zn	Addition
WQ	0.76	0.79	0.79	0.15	0.10	0.06	0
WQ+Zn	0.65	0.63	0.79	0.19	0.09	0.27	0
WQ+Ni	0.77	0.64	0.77	0.21	0.09	0.07	0.11
WQ+Mn	0.60	0.64	0.77	0.18	0.31	0.07	0
WQ+Ti	0.53	0.61	0.77	0.18	0.09	0.07	0.09
WQ+V	0.56	0.63	0.74	0.17	0.09	0.06	0.15
WQ+Zr	0.57	0.63	0.75	0.18	0.09	0.07	0.19
WQ+Ba	0.73	0.62	0.77	0.14	0.09	0.06	0*
WQ+Sr	0.83	0.62	0.77	0.14	0.09	0.06	0.02*

6.3 Results and Discussion

6.3.1 First-principles Partitioning Calculations

The study of solute-partitioning to precipitation phases is of great interest due to the potential for controlling particle morphology and coarsening resistance. DFT and APT studies performed previously have demonstrated that Si atoms prefer partitioning into the Cu sub-lattice in Al_2Cu (θ') precipitates over partitioning into α-Al, and this was supported by a strong thermodynamic driving force as predicted by DFT calculations [112, 164]. The study of Zn additions in alloy W319 by Biswas et al. [31] found that Zn partitioned to the Q-phase, though the DFT results presented in the paper found that Zn incorporation into all sub-lattices of the Q-phase was energetically unfavorable. As such it was argued that the partitioning must be due to a kinetic effect trapping the Zn in the Q-phase during precipitation. Zn partitioning to the Q-phase was reassessed as part of this project.

DFT partitioning energies (E_p) to the Q-phase for solutes of Zn, Ag, Au, Ni, Co, V, Cr, Mo, Zr, W, Mn, Ti, Sr, Ba, Ga, Ge, Sn, and Sb are given in Figure 6.2. Solute partitioning energies for each element was calculated for each of the nine symmetry distinct substitutional sites as shown previously in Chapter 3 Figure 3.11. The adopted sign convention is that a negative partitioning energy indicates that solute partitioning to the Q-phase is energetically favorable.

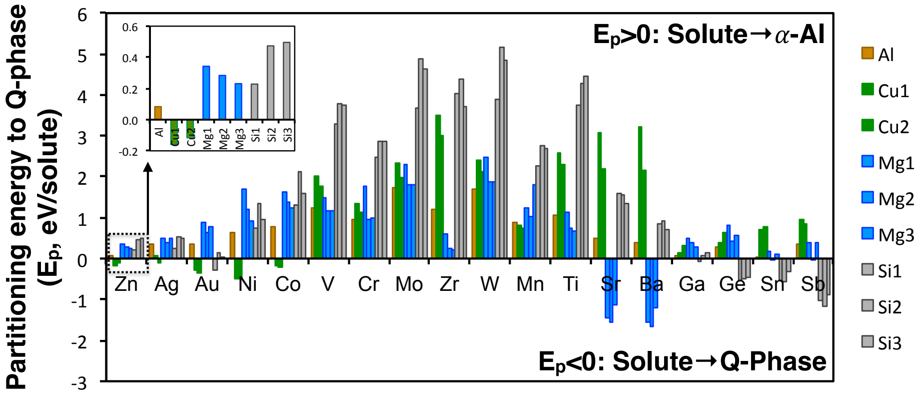

Figure 6.2: First-principles calculated partitioning energies of various solutes to Q-phase. A negative (or positive) value indicates the solute prefers locating into a sub-lattice of the Q-phase (or α-Al).

Our DFT calculations indicate that Zn is indeed energetically favorable to partition to the Q-phase, in particular to the Cu sub-lattice of the Q-phase. This discrepancy between Biswas et al. and this work may be due to the different relaxation schemes utilized in the DFT calculations. In this project all structures were relaxed with respect to all cell-internal and -external degrees of freedom. In the previous work only the position of atoms were optimized under fixed experimental lattices [31]. The results obtained as part of this project therefore suggest that the partitioning of Zn to the Q-phase can be explained by thermodynamic effects similar to the partitioning of Si to θ'-phase precipitates.

The DFT results for the various solute elements indicate that Zn, Ag, Au, Ni, Co, Sr, Ba, Ga, Ge, Sn, and Sb partition to the Q-phase. The solute element partitioning energies are summarized on the periodic table in Figure 6.3 where the highlights indicate a favorable partitioning to either the Cu (orange), Mg (purple), or Si (green) sub-lattice of the Q-phase and those found to be unfavorable (gray). Presentation of the partitioning energies on the periodic table highlight that each solute element shows a preference to sites which have similar electronic structure and atomic radius. It is found that Zn, Ag, Au, Ni, and Co prefer Cu sub-lattice sites and indeed are situated around Cu on the periodic table. The same is found for Ga, Ge, Sn, and Sb preferring the Si sub-lattice sites and Sr and Ba preferring the Mg sub-lattice sites. In addition Mg has the largest atomic radius among the elements (Al, Cu, Si) in the Q-phase and it can be seen that the larger elements of Sr, Ba, Sn, and Sb tend towards these sites as well.

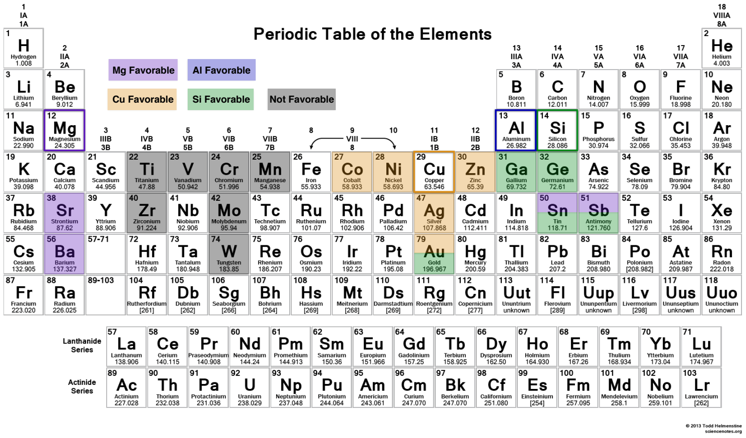

Figure 6.3: Summary of the solute partitioning energies on the periodic table. Highlights give partitioning energy sub-lattice preference.

6.3.2 APT Composition Analysis

In order to validate the DFT predictions, APT experiments were performed. APT analysis was performed on all nine alloys listed in Table 6.1. In addition to Si, Mg, and

Cu, all of the minor alloy additions were detected in the mass spectra except Ba and Sr. The three primary isotopes of Zn were detected in both the singly and doubly charged state ($^{64}\mathrm{Zn}^{1+,2+}$, $^{65}\mathrm{Zn}^{1+,2+}$, $^{66}\mathrm{Zn}^{1+,2+}$). The isotopes of Ni ($^{58}\mathrm{Ni}^{1+}$, $^{60}\mathrm{Ni}^{1+}$) were found only in the singly charged state. Evaporation of Mn was found to occur in both the singly ($^{55}\mathrm{Mn}^{1+}$) and doubly ($^{55}\mathrm{Mn}^{2+}$) charged states. The five most abundant isotopes of Ti ($^{46}\mathrm{Ti}^{2+}$, $^{47}\mathrm{Ti}^{2+}$, $^{48}\mathrm{Ti}^{2+}$, $^{49}\mathrm{Ti}^{2+}$, $^{50}\mathrm{Ti}^{2+}$) were found only in the double charged state, two of which overlap the two singly charged isotope peaks of Mg ($^{24}\mathrm{Mg}^{1+}$, $^{25}\mathrm{Mg}^{1+}$). The Ti and Mg overlap accounts for 78.9% of the Ti abundance. In the APT analysis of alloy WQ+Ti the two overlap peaks are assigned to Mg due to the overwhelming amount of Mg compared to Ti, and thus scaling of the Ti concentration is performed with relation to the 3 non-overlapping Ti isotopes. The isotope of V was found only in the doubly charged state ($^{51}\mathrm{V}^{2+}$). The five most abundant isotopes of Zr were found to evaporate in both the singly and double charged states ($^{90}\mathrm{Zr}^{1+,2+}$, $^{91}\mathrm{Zr}^{1+,2+}$, $^{92}\mathrm{Zr}^{1+,2+}$, $^{94}\mathrm{Zr}^{1+,2+}$, $^{96}\mathrm{Zr}^{1+,2+}$). Thus the APT mass spectrum was able to confirm and identify all the elements of interest in the alloy series.

Rod-like Q-phase precipitates were found in all samples aged for 24 hours at 200°C. Figure 6.4 shows the 3-D reconstructions with Al atoms displayed in blue to demonstrate tip shape and Q-phase particles outlined utilizing a 7% Mg+Si isoconcentration surfaces determined using the 2-D concentration profile method outlined previously. The WQ+Mn alloy reconstruction also contained an Fe-Mn intermetallic which is outlined using a 5% Mn iso-surface in yellow. All samples were found to contain ∼1.3-1.5% phase fraction of Q-phase. The proxigram method was used to analyze the composition of the Q-phase precipitates for the WQ, WQ+Zn, WQ+Mn, and WQ+Ti alloys, which had proxigrams with reliable plateau sections for averaging concentrations. The average composition of the Q-phase precipitates as found from the proxigram in Figure 6.5(a) in the WQ alloy was found to be 41.18 Mg- 25.34 Si- 21.96 Al- 11.52 Cu at.%.

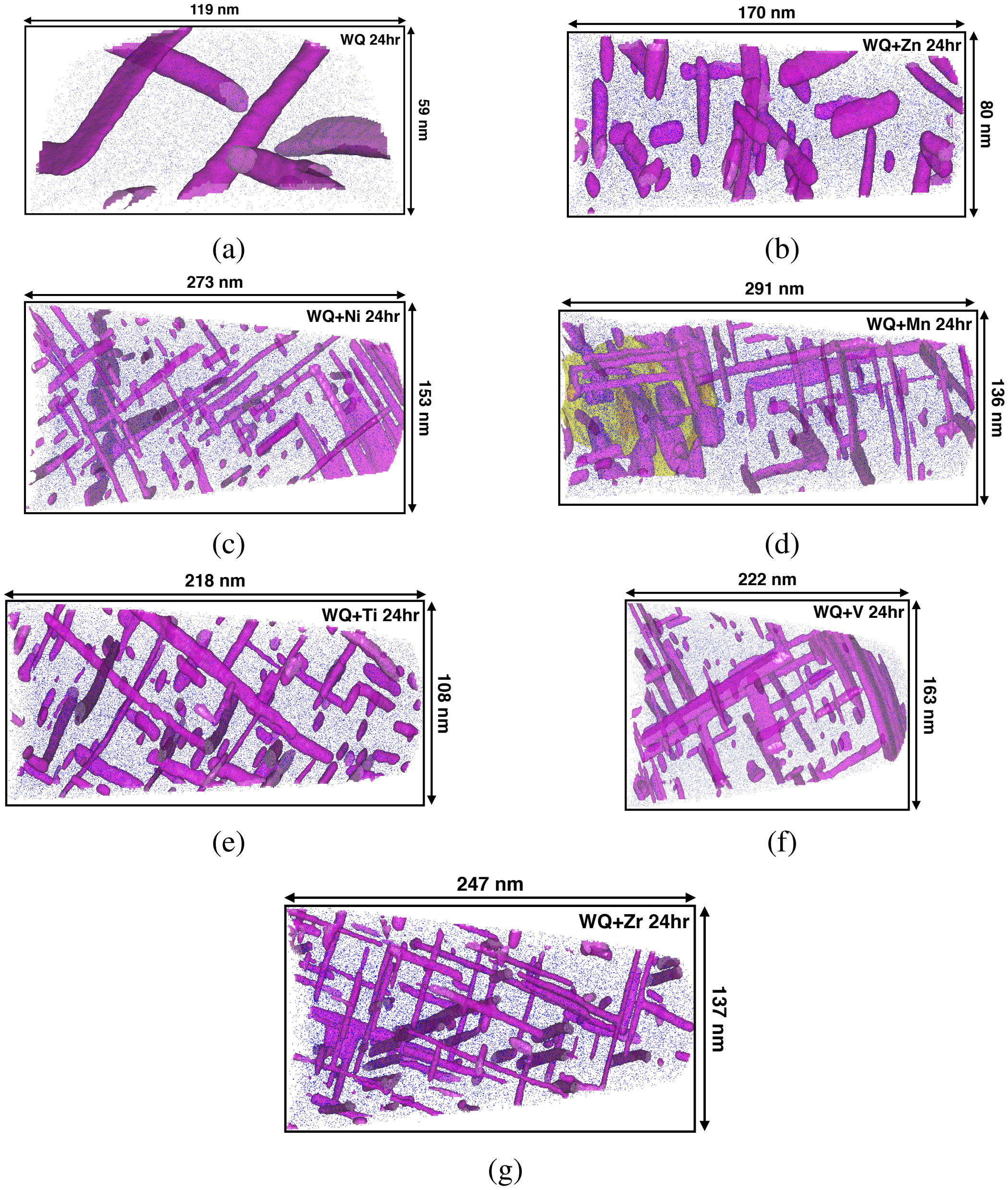

(a) (b) (c) (d) (e) (f) (g)

Figure 6.4: 3DAPT reconstructions for the WQ addition alloys aged at 200°C for 24 hrs. Al atoms shown in blue, Q-phase outlined using 7% Mg+Si iso-surfaces, and Fe-Mn intermetallic particle shown in yellow with a Mn iso-surface (a) WQ, (b) WQ+Zn, (c) WQ+Ni, (d) WQ+Mn, (e) WQ+Ti, (f) WQ+V and (g) WQ+Zr.

APT analysis of the six Q-phase containing wrought Al alloys with DFT motivated alloying additions show varying degrees of partitioning. The APT analyses provide experimental evidence of Zn, Ni, Ti, V, and Zr partitioning to the Q-phase precipitates after aging at 200°C for 24 hours. The proxigram used in the compositional analysis of the Q-phase precipitates observed in the WQ+Zn sample is shown in Figure 6.5(b). The spatial composition profile of the Al matrix is on the left (negative distance) while that of the Q-phase is situated on the right (positive distance) of the isoconcentration surface location (zero distance). There is considerable partitioning of Zn to the Q-phase observed in this alloy consistent with the favorable partitioning energies as calculated by DFT. The average chemical composition of the Q-phase precipitates is: 37.67 Mg- 25.83 Si- 25.48 Al- 10.59 Cu- 0.43 Zn at.%. The observed partitioning ratio between the Q-phase particles and the α-Al matrix is 4.2. Zn partitioning to the Q-phase as explored previously by Biswas et al. was used as a control to validate the APT compositional evaluations performed. Biswas found that after aging the commonly used commercial W319 alloy, which contains 0.13 wt.% Zn, at various aging times and temperatures that there was observable Zn concentration within the Q-phase precipitates. It was reported that the solubility of Zn in the Q-phase decreased from 1.08 at.% at 165°C for 8 hrs to 0.074 at.% at 260°C for 4 hrs with increasing aging temperature. Our reported Zn solubility of 0.42 at.% at 200°C follows their reported trend and falls within the Zn compositions reported at 190°C and 260°C.

WQ+Ni alloy samples demonstrated Ni partitioning to the Q-phase as shown in the proxigram in Figure 6.5(c). The concentration of the Ni content within the Q-phase was around 0.065 at.% and due to the low measured solubility of the Ni content within the α-Al matrix ($\sim$0.0022 at.%) the partitioning ratio was found to be about 28.4. Like Zn, first-principles calculations of the Ni partitioning energies indicate that there exists a ther-

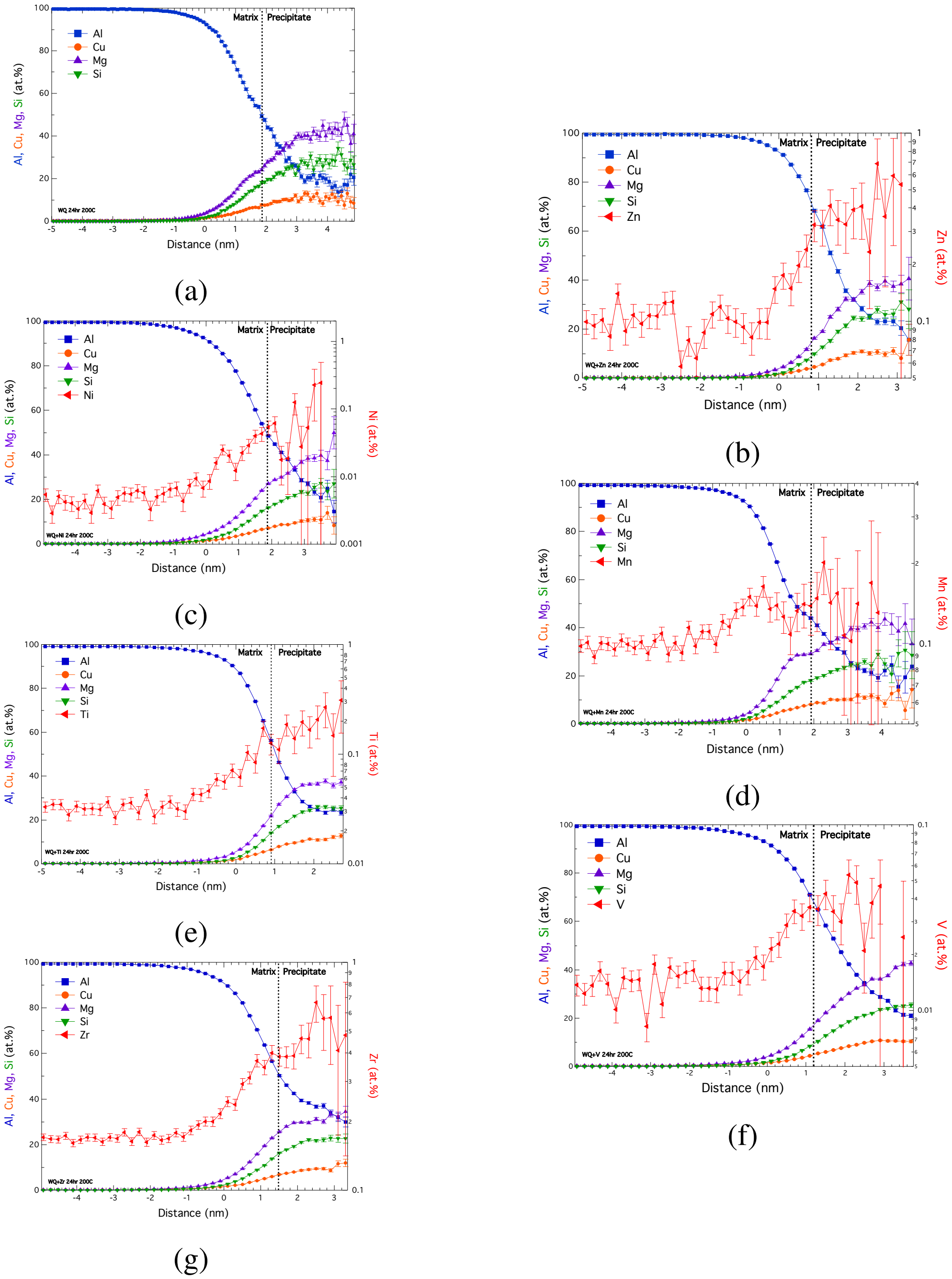

(a)

(b)

(c)

(d)

(e)

(f)

(g)

Figure 6.5: Proximity histograms of the Q-phase particles found in (a) WQ, (b) WQ+Zn, (c) WQ+Ni, (d) WQ+Mn, (e) WQ+Ti, (f) WQ+V, and (g) WQ+Zr.

modynamic driving force for Ni partitioning to the Q-phase. The WQ+Mn alloy samples did not demonstrate any remarkable partitioning of Mn to the Q-phase. The average Q-phase composition was found to be: 41.50 Mg- 26.04 Si- 21.46 Al- 11.00 Cu at.%, very similar to those found in the WQ+Zn sample. There was perceivable localized segregation of Mn at the α-Al/Q-phase interface as evident by the enhanced Mn concentration around 0 nm in the proxigram in Figure 6.5(d). The interface concentration of Mn was found to be around 0.14 at.% Mn compared to that of the matrix 0.006 at.% Mn when taken far from the precipitates. The majority of the Mn alloy addition was found in α-Fe ($Al_{15}Si_2(Fe,Mn)_3$) due to Fe impurities from the casting process. This is in agreement with our first-principles calculations, in that Mn was not found to partition to the Q-phase. It should be noted that large particles of Q-phase were found to nucleate on the α-Fe particle suggesting heterogeneous nucleation. These large Q-phase particles were found to contain similar compositions as their smaller counterparts.

Contrary to the first-principles calculated partitioning energies of this study, it was experimentally observed that Ti, V, and Zr all partitioned to the Q-phase precipitates. Figure 6.5(e) shows the proxigram used in the compositional analysis of the Q-phase precipitates found in the WQ+Ti alloy sample. The proxigram only employs the Ti content for those mass peaks that do not overlap with that of Mg, thus the concentration shown is lower than the true Ti content. The average Q-phase composition after Ti/Mg overlap modification was: 37.62 Mg- 26.00 Si- 23.86 Al- 11.44 Cu- 1.07 Ti at.%. The partitioning ratio for Ti was found to be 10.9, with a Ti matrix composition around 0.099 at.%. Note the overall Ti composition found in the APT run was higher than that measured by OES, potentially due to macro-segregation within the alloy. Compositional analysis of the WQ+V alloy samples utilized the proxigram shown in Figure 6.5(f). V is shown to partition to the Q-phase with a content of 0.037 at.%. Due to the low measured matrix solubility of V, the partitioning ratio between the Q-phase particles and the α-Al matrix is 3.5. It should be noted that V is also known to partition to Fe intermetallics like $Al_{12}(Fe,V)_3Si$ [165], leading to the overall low bulk V content observed in the APT run. The proxigram used in the compositional analysis of the Q-phase for the WQ+Zr alloy sample is shown in Figure 6.5(g). Partitioning of Zr to the Q-phase precipitates was observed. The average chemical composition of Zr in the Q-phase was found to be about 0.42 at.%, which corresponds to a partitioning ratio of about 2.9.

APT composition data for the partitioning alloys is summarized in Table 6.2. Alloys are presented with increasing measured partitioning ratio ($k_{Q/FCC}$) at 200°C. Experimentally measured compositions for both the Q-phase and FCC matrix are presented. Note that compositions of the Q-phase are listed for the WQ+Ni, WQ+V, and WQ+Zr alloys with Al overlap present as can be seen in their respective proxigrams.

The presence of Ti, V, and Zr partitioning to the Q-phase is contrasting to that of Ni and Zn. Both Ni and Zn are relatively fast diffusers in the α-Al matrix, comparable to that of Mg, Cu, Si, and the self-diffusion of Al (see Figure 6.1). Contrarily, Ti, V, and Zr diffuse order of magnitudes slower. Both Ni and Zn are also similar in atomic radii, 149 pm and 142 pm respectively, to that of Cu (145 pm) which is the element they are most energetically favorable to substitute. Ti (176 pm), Zr (206 pm), and V (171 pm) are situated between Al (143 pm), Cu (145 pm), Mg (220 pm) and Si (210 pm) making them easier to fit into the Mg and Si sites than the Al and Cu ones though still energetically unfavorable according to DFT. It is possible that due to the slow diffusivity of Ti, Zr, and V that the elements become trapped in the Q-phase leading to a non-equilibrium partitioning like effect. It is also important to consider the approximations of the DFT calculations performed, such

Table 6.2: Experimentally measured phase compositions for partitioning alloys aged at 200°C for 24 hrs.

Alloy	$k_{Q/FCC}$	Phase	Al (at.%)	Si (at.%)	Mg (at.%)	Cu (at.%)	Addition
WQ	-	Q	19.14	27.98	41.49	11.39	-
		FCC	99.73	0.07	0.02	0.18	-
WQ+Mn	<1	Q	21.46	26.04	41.50	11.00	-
		FCC	99.69	0.03	0.13	0.14	0.0055
WQ+Zr	2.9	Q	19.09	27.60	43.34	9.55	0.42
		FCC	99.57	0.06	0.10	0.13	0.15
WQ+V	3.5	Q	22.62	24.89	41.86	10.60	0.037
		FCC	99.71	0.04	0.09	0.15	0.01
WQ+Zn	4.2	Q	25.48	25.83	37.67	10.59	0.43
		FCC	99.61	0.05	0.09	0.15	0.10
WQ+Ti	10.9	Q	23.86	26.00	37.62	11.44	1.07
		FCC	99.60	0.05	0.09	0.16	0.10
WQ+Ni	28.4	Q	27.26	23.97	38.03	10.68	0.065
		FCC	99.72	0.06	0.08	0.14	0.002

as non-interacting solutes and 0K non-finite temperature. These additional effects could change the calculated partitioning energies, motivating the need for a finite-temperature DFT study. As well as in first-principles, uncertainties exist in the APT study. The low alloying content of the elemental additions lead to large compositional error within the Q-phase precipitates. Larger alloy additions and longer aging times could reduce the noise associated with small atomic counts in the proxigram analysis for these elements.

The impact of partitioning additions to the Q-phase are summarized in Figure 6.6. Figure 6.6(a) plots the normalized diffusivity for all partitioning elements including Al, Cu, Mg, and Si in the Q-phase at 300°C versus the measured partitioning ratios via APT after aging at 200°C. Elements that lie above the $ln(D_X/D_{Al}) = 0$ line diffuse faster than the self diffusion of Al, while those below are slower. Elements that lie to the right of the $ln(k_{Q/FCC}) = 0$ line partition to the Q-phase and those to the left do not. The exact partitioning ratio for Mn was not fully measured due to the large error that was generated in the proxigram because of its low content in the Q-phase. As such, the partitioning ratio for Mn should be less than 1 ($ln < 0$). Ideal candidates for decreasing the coarsening rate of the Q-phase are located in the bottom right of Figure 6.6(a), i.e. they are both slow diffusers and partition to the Q-phase. In this region the elements of Cu, Ni, Zr, Ti, and V can be found.

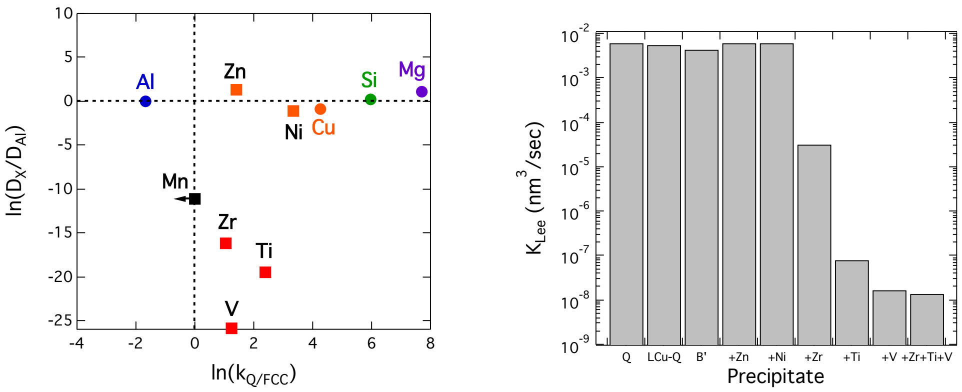

(a) (b)

Figure 6.6: (a) Normalized diffusivity at 300°C versus measured partitioning ratios at 200°C for elements in the Q-phase. (b) Theoretical Lee model coarsening rate for Q-phase compositions with partitioning additions at 300°C.

The impact of the partitioning elements on the Q-phase coarsening rate can be calculated using Equations 4.4 and 4.5 from Chapter 4. A standardized equilibrium FCC$_{\alpha\text{-}Al}$ matrix composition has been assumed for this coarsening rate calculation and is taken as the APT measured matrix composition from the GMQ2 1000 hr aged alloy. The equilibrium matrix composition of the elemental additions are taken as the APT measured matrix composition from their respective alloys aged at 200°C. Using the IFE, molar volume, and equilibrium aspect ratio defined in Chapter 4, the Lee coarsening constant has been calculated at 300°C. The coarsening rate for the GMQ2 alloy Q-phase baseline composition, the CM alloy low-Cu Q-phase composition, the 356 B'-phase Cu-free composition, as well as the baseline Q-phase composition (GMQ2 1000 hr) with additions of Zn, Ni, Zr, Ti, V, and a combination of Zr, Ti, and V are summarized in Figure 6.6(b).

It can be seen in Figure 6.6(b) that for the Cu variation within the Q-phase the coarsening rate is found to decrease with decreasing Cu content. This may seem counter intuitive due to Cu being the slowest native diffuser in the Q-phase composition, thus implying that a reduction in Cu content should lead to an increase in coarsening rate. However, if one examines Equation 6.1 it can be shown that increasing the content of a phase within the precipitate, regardless of its diffusivity constant, can also decrease the overall coarsening rate. Because a decrease in Cu corresponds to a similar increase in Mg content in the Q-phase, the increase of the Mg partitioning dominates the loss of slow Cu diffusion.

The additions of Zn and Ni to the base Q-phase composition are found to have little effect on the coarsening resistance of the Q-phase at 300°C. This is because the diffusivity of Zn and Ni are only marginally different from the diffusivities of Al, Cu, Mg, and Si already present within the Q-phase. However, additions of Zr, Ti, and V have a very large effect in reducing the Q-phase coarsening rate. Zr partitioning resulting in about a 0.4 at.% solubility in the Q-phase results in a 2 order of magnitude drop in coarsening rate. Ti partitioning resulting in about a 1 at.% solubility in the Q-phase is able to drop the coarsening rate by 5 orders of magnitude. Due to the extremely slow diffusivity of V in aluminum, a relatively small addition of V to the Q-phase (measured at only 0.037 at.%) can reduce the coarsening rate of the Q-phase by 5 orders of magnitude and being about 5 times slower than that of the Ti addition. To see the effect of multiple elemental additions on the Q-phase coarsening rate, the combination of the three slowest diffusors (Zr, Ti, and V) was calculated. The overall coarsening rate for the 3 element combination is found to be only marginally smaller than that of the V addition alone. From these coarsening rate calculations it is strongly suggested that further work be performed on Zr, Ti, and V containing alloys for their potential in high-temperature environments.

6.3.3 Misfit Strains

Interfacial energy and misfit strains between a precipitate phase and the matrix are critical to understanding the morphology of the particles as they grow and coarsen. Even though the Q-phase is a potent strengthening phase and found in most commercial alloys the interfacial energy and misfits have not been investigated extensively. As stated previously, it is known that the Q-phase has a common habit plane of $\{510\}_{\alpha\text{-}Al}$, and its orientation relationship with the α-Al matrix is denoted as $[0001]_Q||[001]_{\alpha\text{-}Al}$ and $(11\bar{2}0)_Q||(510)_{\alpha\text{-}Al}$. The creation of a orthohexagonal unit cell from the hexagonal unit cell of the Q-phase with a $(11\bar{2}0)_Q||(510)_{\alpha\text{-}Al}$ orientation is used to explore the interfacial energy using DFT and the misfit strains. The orthohexagonal cell is shown in Figure 6.7 with the HRTEM insets from Fiawoo et al. [38]. The HRTEM micrographs from Fiawoo et al. demonstrate a facet parallel to the $\{510\}_{\alpha\text{-}Al}$ for a Q-phase rod cross-section, with the Cu sub-lattice designated using red and the Si network designated using yellow. The orthohexagonal lattice parameters are defined as shown in Figure 6.7 with a_Q being from one Cu termination to the other along the a-axis, b_Q defined as the long axis from Cu to Cu atom spanning two hexagonal unit cells, and c_Q being out of plane and equal to the thickness of the unit cell shown in Figure 3.11 of Chapter 3.

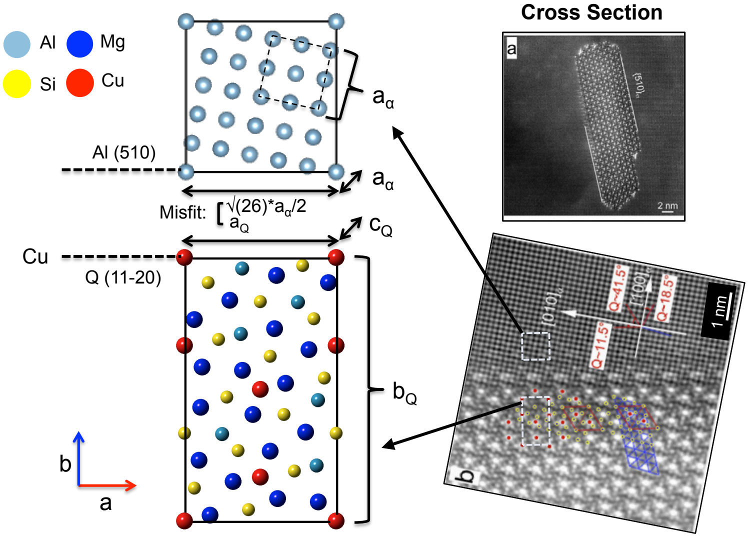

Figure 6.7: Orientation of a Q-phase cross section with a $\{510\}_{\alpha\text{-}Al}$ facet. The orthohexagonal unit cell is shown with a $(11\bar{2}0)_Q||(510)_{\alpha\text{-}Al}$ orientation to the α-Al matrix cell. HRTEM micrographs from Fiawoo et al. [38].

Using an orthohexagonal unit cell like that shown in Figure 6.7, DFT interfacial energy calculations were performed by Kyoungdoc Kim using various termination sites and configurations along the a-axis of the figure. It was found that a Cu-terminated interface for the orthohexagonal Q-phase cell with an α-Al mismatch with 6 Al atoms along the interface resulted in the lowest interfacial energy. The interfacial energy was found to be 0.52 J/m^2. The Cu termination is consistent with experimental evidence showing that Cu seggregation was detected at the Q$||\alpha$-Al interface using energy-filtered TEM by Matsuda et al. [166]. Calculation of the interfacial energy of the hemispherical cap of the Q-phase using DFT is not possible due to the unknown orientation between the cap and the FCC matrix.

The principal misfit strains are defined using the orthohexagonal lattice parameters

(a_Q, b_Q, and c_Q) starting with the Wolverton [17] $Al_3Cu_2Mg_9Si_7$ primitive cell and the lattice parameter of FCC aluminum (a_α). The strain between the $[11\overline{2}0]_Q||[510]_{\alpha\text{-}Al}$ directions is denoted as ϵ_a, the strain between $[0001]_Q||[001]_{\alpha\text{-}Al}$ is denoted as ϵ_c, and between the b_Q lattice parameter and two $[510]_{\alpha\text{-}Al}$ lattice parameters is denoted as ϵ_b, where no optimization of multiple b-axis lattices were considered. The principal misfit strains are defined as

$$\epsilon_a = \frac{2}{\sqrt{26}}\frac{a_Q}{a_\alpha} - 1, \quad \epsilon_b = \frac{1}{\sqrt{26}}\frac{b_Q}{a_\alpha} - 1, \quad \text{and} \quad \epsilon_c = \frac{c_Q}{a_\alpha} - 1 \tag{6.3}$$

The repeat distance along the $\langle 510\rangle_{\alpha\text{-}Al}$ directions of the α-Al matrix is equal to $\frac{\sqrt{26}}{2}a_\alpha =$ 10.298 Å where a_α is the lattice parameter of FCC aluminum. This is very similar to the lattice parameter as calculated using DFT for the relaxed $Al_3Cu_2Mg_9Si_7$ unit cell of 10.417 Å thus resulting in a misfit strain (ϵ_a) of 1.16%. Along the $[0001]_Q||[001]_{\alpha\text{-}Al}$ direction the misfit strain between the two primitive unit cells (ϵ_c) is -0.83%. Thus the $(11\overline{2}0)_Q||(510)_{\alpha\text{-}Al}$ is very coherent and consistent with the small interfacial energy calculated using DFT. The misfit strain between the b_Q lattice and two $(510)_{\alpha\text{-}Al}$ lattices (ϵ_b) is approximately -12.39%. This is a very large misfit corresponding to an incoherent plane between the rod hemispherical cap face and is expected due to the rapid growth in the $[100]_{\alpha\text{-}Al}$ direction.

Starting from the Wolverton $Al_3Cu_2Mg_9Si_7$ Q-phase composition the misfit strains corresponding to partitioning element substitutions on the most energetically favorable Q-phase sub-lattice are presented in Table 6.3. Those elements that were deemed energetically unfavorable where not explored.

The misfit strains are examined using two different desired Q-phase morphologies: long and skinny (large aspect ratios) versus squat and fat (short aspect ratios). To achieve longer Q-phase rods (and thus potentially smaller radii for a given particle volume it is

Table 6.3: Principal misfit strains for partitioning elements to the Q-phase.

Addition	Site	ϵ_a	ϵ_b	ϵ_c
Base	None	1.16	-12.39	-0.83
Zn	Cu1	1.07	-12.47	0.87
Zn	Cu2	1.30	-12.26	0.64
Ni	Cu1	1.24	-12.32	-1.68
Ni	Cu2	1.03	-12.50	-1.49
Co	Cu1	1.07	-12.47	-1.24
Co	Cu2	0.94	-12.58	-1.21
Sb	Si1	2.18	-11.50	1.11
Sb	Si2	1.08	-11.85	1.16
Sb	Si3	2.23	-11.70	1.41
Sn	Si1	2.70	-11.05	-0.42
Sn	Si2	2.38	-11.48	-0.10
Sn	Si3	2.47	-11.37	0.27
Ge	Si1	1.51	-12.09	-0.74
Ge	Si2	1.51	-12.11	-0.62
Ge	Si3	1.49	-12.14	-0.55
Ba	Mg1	3.46	-8.88	1.68
Ba	Mg2	3.03	-11.81	2.13
Ba	Mg3	3.76	-8.48	1.93
Sr	Mg1	2.15	-9.64	0.72
Sr	Mg2	2.38	-12.03	1.21
Sr	Mg3	2.34	-9.82	0.82

desirable to have very small ϵ_a and ϵ_c misfit magnitudes and a large ϵ_b misfit magnitude compared to the base composition. To achieve a smaller aspect ratio and have smaller lengths and larger radii for a given particle volume it is desirable to have a smaller ϵ_b misfit magnitude and larger ϵ_a and ϵ_c misfit magnitudes from the base condition. Zn partitioning is found to reduce only one of the ϵ_a and ϵ_c misfits while the other increases, and only Zn on the $Cu1$ site increases the misfit in the b direction. Depending on which of the Cu sites Zn swaps in practice it can have an effect towards either higher or lower aspect ratios. Ni and Co are found to decrease ϵ_a but increase ϵ_c considerably while increasing ϵ_b in all but the Ni on $Cu1$ case. The loss of c-misfit coherency along with the b-misfit makes determining aspect ratio trend changes difficult.

Si sub-lattice substitution for elements of Sb, Sn, and Ge all result in smaller ϵ_b misfit magnitudes. Sb partitioning to any Si site is found to increase the ϵ_a and ϵ_c misfits, which would results in smaller aspect ratios. Partitioning of Sn and Ge are found to increase ϵ_a misfits and decrease ϵ_c misfit magnitudes again making it difficult to determine the potential change in morphology. Mg sub-lattice substitution by Ba and Sr are found to decrease the magnitude of the ϵ_b misfit. Ba, like Sb before, is found to increase both the ϵ_a and ϵ_c misfits resulting in potentially smaller aspect ratios. Sr partitioning is found to increase the magnitude of the ϵ_a misfit, but the ϵ_c misfit depends on the sub-lattice site. Calculated misfit strains can potentially be used to determine which additions can be included in an alloy design for the desired particle morphology. Further experimental work on identifying morphological changes with these additions should be undertaken.

6.4 Conclusions

Partitioning of elements to the Q-phase was explored using both DFT calculations and APT experiments. DFT calculations performed by Kyoungdoc Kim determined energetically favorable partitioning energies toward the Q-phase for solutes of Zn, Ag, Au, Ni, Co, Sr, Ba, Ga, Ge, Sn, and Sb. It was found that elements with similar electronic structure and atomic radius to those of Cu, Si, and Mg are more likely to partition to the respective Q-phase sub-lattices. Motivated by the DFT results, various wrought alloys were made based on the alloy WQ with additions of Zn, Ni, Mn, Ti, V, Zr, Ba, and Sr. Though the additions of Ba and Sr where not detectable in the OES and APT composition analysis.

It was determined that elements of Zn, Ni, Ti, V, and Zr all partitioned to the Q-phase with varying concentrations. Experimental results for Zn, Ni, and Mn were found to be consistent with the DFT predictions while the experimental evidence of partitioning for Ti, V, and Zr contrasted the results of DFT calculations. Interestingly these three elements (Ti, V, and Zr) are considerably slower diffusers in Al and could have potentially become trapped in the Q-phase. Though all DFT calculations were performed at 0K, finite temperature calculations would result in more accurate partitioning energies. Calculated coarsening rates for Q-phase composition variation in addition to elemental additions at 300°C suggest that Zr, Ti, and V have potential in reducing the coarsening rate of the Q-phase for high-temperature applications. Further experimental work on these solute additions with longer aging times resulting in larger particles and more accurate compositions as well as alloys with larger additions are of great interest.

Misfit strains based on the orthohexagonal Q-phase lattice and the $(11\overline{2}0)_Q||(510)_{\alpha\text{-}Al}$ interface were determined using DFT calculated lattice parameters. Site swapping of Sb and Ba were found to influence all three principal misfit strains to result in small aspect ratio particles. The implications of Ni, Co, Zn, Sn, Ge, and Sr partitioning varied on the exact sub-lattice site and inversely effected the magnitudes of ϵ_a and ϵ_c misfits. DFT calculations for elements found to experimentally partition have not been performed. Experimental evidence of particle morphology change has yet to be determined.

7 Summary and Future Work

This work has provided detailed insight into the Al-Si-Mg-Cu quaternary system through exploring the composition design space using lab-scale castings, expanding the knowledge of Q-phase composition and evolution, while enabling the modeling of key properties for designing future Al alloys for high temperature applications. Advanced experiential techniques such as TEM (*in-situ* and high-resolution) and 3DAPT were used to examine precipitation in a series of wrought and cast alloy systems. Phase identification, compositional analysis, particle morphology measurements, and phase fraction calculations were performed over a series of aging times and temperatures. The Q-phase compositions were experimentally found to vary with changing bulk alloy Cu content and suggests a Cu:Mg sub-lattice where Mg atoms can replace Cu. DFT calculations were unable to reconcile these experimental findings, suggesting that any change with Cu content from the Wolverton [17] and Arnberg [18] compositions is energetically unfavorable. However, the lowest calculated vacancy and defect formation enthalpies for Al and Si atoms on the Q-phase sub-lattices demonstrates the potential for the change in composition from the Wolverton ground state to various literature reported compositions including compositions found in this work with finite temperature effects. The thermodynamic description of the Q-phase was updated using the experimentally determined Cu variation in the Q-phase precipitates and was found to drastically improve the predictive capabilities of equilibrium calculations with respect to stable phases at 200°C and composition of the Q-phase.

Using the temporal evolution of the matrix composition and particle morphology during Q-phase rod precipitation it was found that classical spherical particle based theories like the Gibbs-Thomson effect and LSW coarsening theory were maintained during aging of Q-phase containing alloy systems. An LSW based coarsening model developed by Lee et al. [103] was utilized in modeling the growth and coarsening of the Q-phase and was found to agree well with experimentally measured particle sizes using appropriate input parameters. Due to the lack of plate shaped particle flux equations, a machine learning model was developed for θ'-phase growth and coarsening using training data gathered from the literature and as measured from alloys examined as part of this project. The machine learning model was found to describe the evolution of the plates well as a function of aging time, temperature, and bulk alloy composition.

The strengthening of both rod and plate-like precipitates in Al alloys was explored using a modified Orowan strengthening equation. The critically important particle spacing term for rationally oriented particles in the $\{111\}_{\alpha\text{-}Al}$ slip plane is a function of particle morphology. This term was derived for finite rods oriented with a $\langle 100\rangle_{\alpha\text{-}Al}$ primary growth direction. Comparison of particle morphology on particle spacing and strength were examined using two conditions: constant particle volume and constant particle radius. The most potent strengthening shape was found to vary depending on the condition chosen.

A yield strengthening model was developed using the shape dependent Orowan equation and particle coarsening laws defined previously for the rod-like Q-phase and plate-like θ'-phase. The temperature effect of precipitation kinetics was captured using the Shercliff and Ashby process model [125] and found to accurately capture the correct trends with regard to variation in aging temperature. The temperature effect of solid solution strengthening was implemented into the total strengthening model using the Feltham trough model [126] which was calibrated using literature data for an Al-Mg binary alloy. The

Feltham model was found to accurately describe the solid solution strengthening increment with composition and testing temperature for Mg. The total strengthening model was assembled in MATLAB where the only input parameters are the alloy composition aging time, temperature, testing temperature, and various matrix and precipitate volume fractions and compositions which are determined using CALPHAD calculations. The model has no variable calibration terms between alloy systems and uses only one set of initial calibration terms for the individual models of particle morphology and kinetic effects. The model was found to accurately describe the yield strength behaviors as a function of aging and test temperatures for over 35+ alloy systems. The model is found to agree extremely well with high-temperature long aged yield strength tensile experiments with 200 hrs of conditioning at testing temperature. Using the model in connection with CALPHAD simulations the ability to map out the yield strength over a wide range of alloy compositions is shown and will enable rapid development of new alloys with minimal experimentation.

It was determined that both Q-phase rod and θ'-phase plate containing alloys demonstrated very little strength enhancement at high temperature testing compared to baseline alloys. Yield strength predictions suggest that only minimal improvement can be obtained by further increasing phase fraction. It is therefore of great interest to determine partitioning elements to these phases to decrease the coarsening rate and therefore improve strength at these temperatures. DFT calculations were performed for a variety of elemental additions and alloys were cast using likely DFT partitioning candidates. It was experimentally determined that partitioning did occur to the Q-phase for elements of Zn, Ni, Ti, V, and Zr. The DFT predictions were found to agree for those elements that diffused relatively quickly in the α-Al matrix (Zn, Ni, Mn) while slow diffusing elements that were measured in the Q-phase were predicted to be unfavorable via DFT (Ti, V, Zr). Calculated coarsening rate constants for the Q-phase with these additions demonstrated the potential for a dramatically reduced coarsening rate in high-temperature applications. The impact of the partitioning elements on the misfit strain of the Q-phase and α-Al matrix were determined using DFT relaxed Q-phase unit cells. Implications for partitioning on particle morphology change was found to depend on the exact sub-lattice site preferred.

Although this work has provided new insight into the precipitation and aging of the Q-phase and modeling of its strengthening effect, exploration of the partitioning element effects on the Q-phase has only been preliminary analyzed. Finite temperature DFT calculations can lead to improved predictions that can potentially agree with experimental observations. The impact of these elements on the Q-phase coarsening rate should be experimentally explored over a range of aging temperatures and times. In addition, the maximum solubility of these elements in the Q-phase can be examined using APT for varying amounts of addition to the bulk alloy system. The CALPHAD thermodynamic databases can be updated to include these alloying additions as well as other phases that occur when they are present. For instance Ti and V have been found in Fe containing inter-metallics after solidification. The impact of these elements on the growth and coarsening of the Q-phase can be easily applied using the Lee coarsening model if the concentration within the precipitate is known since the diffusion coefficients for the majority of the elements in α-Al is already known.

Highly resistant coarsening precipitates will be necessary to improve the yield strength of Al alloys at high testing temperature. Perhaps these partitioning additions will prevent the large particle sizes that result in large drops in strength that are currently observed. In addition to the effect of these elements on the Q-phase it is of great interest to explore their effect on the θ'-phase platelets as well. The θ'-phase has the advantage of large obtainable phase fractions in the Al system with little to no additional competing phases in the Cu rich phase region unlike the Q-phase. Determining potential partitioning to the θ'-phase as well as its impact on the coarsening rate can potentially lead to the achievement of high strength levels at high aging temperatures. With the incorporation of these elements in the CALPHAD thermodynamic databases and the strengthening models the ability to design alloys with specified coarsening rates for high-temperature applications can be achieved.

References

[1] S. C. Davis, S. E. Williams, and R. G. Boundy, *Transportation and Energy Data Book*. Center for Transportation Analysis Energy and Transportation Science Division, 35 ed., 2016.

[2] A. Guinier, "Structure of Age-Hardened Aluminum-Copper Alloys," *Nature*, vol. 142, pp. 569–570, 1938.

[3] G. D. Preston, "Structure of Age-Hardened Aluminum-Copper Alloys," *Nature*, vol. 142, p. 570, 1938.

[4] S. Esmaeili, M. W. Z. D. Vaumousse, W. J. Poole, A. Cerezo, and D. J. Lloyd, "A study on the early-stage decomposition in the Al-Mg-Si-Cu alloy AA6111 by electrical resistivity and three-dimensional atom probe," *Philosophical Magazine*, vol. 87, pp. 3797–3816, 2007.

[5] F. J. H. Ehlers, S. Wenner, S. J. Andersen, C. D. Marioara, W. Lefebvre, C. B. Boothroyd, and R. Holmestad, "Phase stabilization principle and precipitate-host lattice influences for Al-Mg-Si-Cu alloy precipitates," *Journal of Materials Science*, vol. 49, pp. 6413–6426, 2014.

[6] G. Sha and A. Cerezo, "Early-stage precipitation in Al-Zn-Mg-Cu alloy (7050)," *Acta Materialia*, vol. 52, pp. 4503–4516, 2004.

[7] J. M. Silcock, "The θ' structure in aluminium copper alloys," *Acta Crystallography*, vol. 9, p. 680, 1956.

[8] C. Wolverton and V. Ozoliņš, "Entropically Favored Ordering: The Metallurgy of Al_2Cu Revisited," *Physical Review Letters*, vol. 86, pp. 5518–5521, 2001.

[9] P. H. Hasting, A. G. Frøseth, S. J. Andersen, R. Vissers, J. C. Walmsley, C. D. Marioara, F. Danoix, W. Lefebvre, and R. Holmestad, "Composition of β" precipitates in Al-Mg-Si alloys by atom probe tomography and first principles calculations," *Journal of Applied Physics*, vol. 106, p. 123527, 2009.

[10] P. H. Ninive, A. Strandlie, S. Gulbrandsen-Dahl, W. Lefebvre, C. D. Marioara, S. J. Andersen, J. Friis, R. Holmestad, and O. M. Løvvik, "Detailed atomistic insight into the β" phase in Al-Mg-Si alloys," *Acta Materialia*, vol. 69, pp. 126–134, 2014.

[11] P. M. Derlet, S. J. Andersen, C. D. Marioara, and A. G. Frøseth, "A first-principles study of the β"-phase in Al-Mg-Si alloys," *Journal of Physics: Condensed Matter*, vol. 14, pp. 4011–4024, 2002.

[12] S. J. Andersen, H. W. Zanderbergen, J. Jansen, C. Træholt, U. Tundal, and O. Resio, "The crystal structure of the β" phase in Al-Mg-Si alloys," *Acta Materialia*, vol. 46, pp. 3283–3298, 1998.

[13] C. Ravi and C. Wolverton, "First-principles study of crystal structure and stability of Al-Mg-Si-(Cu) precipitates," *Acta Materialia*, vol. 52, pp. 4213–4227, 2004.

[14] R. Vissers, M. A. van Huis, J. Jansen, H. W. Zanderbergen, C. D. Marioara, and S. J. Andersen, "The crystal structure of the β' phase in Al-Mg-Si alloys," *Acta Materialia*, vol. 55, pp. 3815–3823, 2007.

[15] L. F. Mondolfo, *Aluminum alloys: structure and properties*. Boston: Butterworth, 1979.

[16] S. P. Ringer and K. Hono, "Microstructural Evolution and Age Hardening in Aluminum Alloys: Atom Probe Field-Ion Microscopy and Transmission Electron Microscopy Studies," *Materials Characterization*, vol. 44, pp. 101–131, 2000.

[17] C. Wolverton, "Crystal Structure and Stability of Complex Precipitate Phases in Al-Cu-Mg-(Si) and Al-Zn-Mg Alloys," *Acta Materialia*, vol. 49, pp. 3129–3142, 2001.

[18] L. Arnberg and B. Aurivillius, "The crystal structure of aluminum-copper-magnesium-silicon [AlxCu2Mg12-xSi7, (h-AlCuMgSi)]," *Acta Chemica Scandinavica, Series A*, vol. 34, pp. 1–5, 1980.

[19] G. Phragmen, "The phases occurring in alloys of aluminum with copper, magnesium, manganese, iron, and silicon," *Journal of the Institute of Metals*, vol. 77, pp. 489–552, 1950.

[20] S. Kirklin, J. E. Saal, B. Meredig, A. Thompson, J. W. Doak, M. Aykol, S. Rühl, and C. Wolverton, "The Open Quantum Materials Database (OQMD): assessing the accuracy of DFT formation energies," *NPJ Computational Materials*, vol. 1, p. 15010, 2015.

[21] J. E. Saal, S. Kirklin, M. Aykol, B. Meredig, and C. Wolverton, "Materials Design and Discovery with High-Throughput Density Functional Theory: The Open Quantum Materials Database (OQMD)," *JOM*, vol. 65, pp. 1501–1509, 2013.

[22] A. Wilm, "Physikalisch-metallurgische Untersuchungen über magnesiumhaltige Aluminiumlegierungen," *Metallurgie*, vol. 8, pp. 225–227, 1911.

[23] J. M. Silcock, T. S. Heal, and H. K. Hardy *Journal of the Institute of Metals*, vol. 82, p. 239, 1953.

[24] L. Bourgeois, C. Dwyer, M. Weyland, J.-F. Nie, and B. C. Muddle, “Structure and energetics of the coherent interface between the θ’ precipitate phase and aluminium in Al-Cu,” *Acta Materialia*, vol. 59, pp. 7043–7050, 2011.

[25] M. H. Jacobs, “The structure of the metastable precipitates formed during ageing of an Al-Mg-Si alloy,” *Philisophical Magazine*, vol. 26A, pp. 1–13, 1972.

[26] J. P. Lynch, L. M. Brown, and M. H. Jacobs, “Microanalysis of Age-Hardening Precipitates in Aluminium Alloys,” *Acta Metallurgica*, vol. 30, pp. 1389–1395, 1982.

[27] K. Matsuda, S. Tada, and S. Ikeno, “The Morphology of Precipitates in an Al-1 wt%Mg_2Si Alloy,” *Journal of Electron Microscopy*, vol. 42, pp. 1–6, 1993.

[28] H. Perlitz and A. Westgren, “The cystal structure of Al_2CuMg,” *Arkiv för kemi, mineralogi och geologi*, vol. 16B, pp. 1–5, 1943.

[29] S. P. Ringer, T. Sakurai, and I. J. Polmear, “Origins of Hardening in Aged Al-Cu-Mg-(Ag) Alloys,” *Acta Metallurgica*, vol. 9, pp. 3731–3744, 1997.

[30] S. P. Ringer, K. Hono, I. J. Polmear, and T. Sakurai, “Precipitation processes during the early stages of aging in Al-Cu-Mg alloys,” *Applied Surface Science*, vol. 94/95, pp. 253–260, 1996.

[31] A. Biswas, D. J. Siegel, and D. N. Seidman, “Compositional evolution of Q-phase precipitates in an aluminum alloy,” *Acta Materialia*, vol. 75, pp. 322–336, 2014.

[32] D. J. Chakrabarti and D. E. Laughlin, “Phase relations and precipitation in Al-Mg-Si alloys with Cu additions,” *Progress in materials Science*, vol. 49, pp. 389–410, 2004.

[33] I. Dutta, C. P. Harper, and G. Dutta, “Role of Al2O3 particulate reinforcements on precipitation in 2014 Al-matrix composites,” *Metallurgical and Materials Transactions A*, vol. 25A, pp. 1591–1602, 1994.

[34] A. Perovic, D. D. Perovic, G. C. Weatherly, and D. J. Lloyd, “Precipitation in aluminum alloys AA6111 and AA6016,” *Scripta Materialia*, vol. 41, pp. 703–708, 1999.

[35] G. C. Weatherly, A. Perovic, N. K. Mukhopadhyay, D. J. Lloyd, and D. D. Perovic, “The precipitation of the Q phase in an AA6111 Alloy,” *Metallurgical and Materials Transactions A*, vol. 32A, pp. 213–218, 2001.

[36] S. C. Weakley-Bolin, W. Donlon, C. Wolverton, J. W. Jones, and J. E. Allison, “Modeling the age-hardening behavior of Al-Si-Cu alloys,” *Metallurgical and Materials Transactions A*, vol. 35A, pp. 2407–2418, 2004.

[37] X. Wang, W. J. Poole, S. Esmaeili, D. J. Lloyd, and J. D. Embury, “Precipitation Strengthening of the Aluminum Alloy AA6111,” *Metallurgical and Materials Transactions A*, vol. 34, pp. 2913–2924, 2003.

[38] M. Fiawoo, X. Gao, L. Bourgeois, N. Parson, X. Q. Zhang, M. Couper, and J. F. Nie, “Formation of multiple orientation relationships of Q precipitates in Al-Mg-Si-Cu alloys,” *Scripta Materialia*, vol. 88, pp. 53–56, 2014.

[39] F. J. Feikus, “Optimization of Al-Si cast alloys for cylinder head applications,” *AFS Transaction*, vol. 106, pp. 225–231, 1998.

[40] C. C. Engler-Pinto Jr., J. V. Lasecki, and J. M. Boileau, “A Comparative Investigation on the High Temperature Fatigue of Three Cast Aluminum Alloys,” Tech. Rep. 2004-1-1029, SAE International, 2004.

[41] D. M. Stefanescu, “Casting,” in *ASM Handbook*, vol. 15, ASM International, 9 ed., 1998.

[42] Q. G. Wang, D. Apelian, and J. R. Griffiths, “Microstructural Effects on the Fatigue Properties of Aluminum Castings,” in *Advances in Aluminum Casting Technology* (M. Tiryakioglu and J. Campbell, eds.), pp. 217–223, ASM International, 1998.

[43] Q. G. Wang, “Microstructural Effects on the Tensile and Fracture Behavior of Aluminum Casting Alloys A356/357,” *Metallurgical and Materials Transations A*, vol. 34A, pp. 2887–2899, 2003.

[44] C. S. Smith, *A Search for Structure*. The MIT Press, 1981.

[45] M. Cohen, “Unknowables in the essence of materials science and engineering,” *Materials Science and Engineering*, vol. 25, pp. 3–4, 1976.

[46] G. B. Olson, “Computational Design of Hierarchically Structured Materials,” *Science*, vol. 277, pp. 1237–1242, 1997.

[47] B. Sundman, B. Jansson, and J. O. Anderson, “The Thermo-Calc databank system,” *Calphad*, vol. 9, pp. 153–190, 1985.

[48] E. Scheil, “Bemerkungen zur schichtkristallbildung,” *Zeitschrift fur Metallkunde*, vol. 34, pp. 70–72, 1942.

[49] G. H. Gulliver, "The quantitative effect of rapid cooling upon the constitution of binary alloys," *Journal of the Institute of Metals*, vol. 9, pp. 120–157, 1913.

[50] Z. Mao, D. N. Seidman, and C. Wolverton, "First-principles phase stability, magnetic properties and solubility in aluminum-rare-earth (Al-RE) alloys and compounds," *Acta Materialia*, vol. 59, pp. 3659–3666, 2011.

[51] C. Wolverton and V. Ozoliņš, "First-principles aluminum database: Energetics of binary Al alloys and compounds," *Physical Review B*, vol. 73, p. 144104, 2006.

[52] J. E. Saal and C. Wolverton, "Solute-vacancy binding of the rare earths in magnesium from first principles," *Acta Materialia*, vol. 60, pp. 5151–5159, 2012.

[53] J. A. Yasi, L. G. Hector Jr., and D. R. Trinkle, "First-principles data for solid-solution strengthening of magnesium: From geometry and chemistry to properties," *Acta Materialia*, vol. 58, pp. 5704–5713, 2010.

[54] G. P. M. Leyson, W. A. Curtin, L. G. Hector Jr., and C. F. Woodward, "Quantitative prediction of solute strengthening in aluminium alloys," *Nature*, vol. 9, pp. 750–755, 2010.

[55] G. Kresse and J. Furthmüller, "Efficient iterative schemes for ab initio total-energy calculations using a plane-wave basis set," *Physical Review B*, vol. 54, pp. 11169–11186, 1996.

[56] G. Kresse and . Furthmüller, "Efficiency of ab-initio total energy calculations for metals and semiconductors using plane-wave basis set," *Computational Materials Science*, vol. 6, pp. 15–50, 1996.

[57] G. Kresse and D. Joubert, "From ultrasoft pseudopotentials to the projector augmented-wave method," *Physical Review B*, vol. 59, pp. 1758–1775, 1999.

[58] J. D. Perdew, K. Burke, and M. Ernzerhof, "Generalized Gradient Approximation Made Simple," *Physical Review Letters*, vol. 77, pp. 3865–3868, 1996.

[59] A. Seko, T. Maekawa, K. Tsuda, and I. Tanaka, "Machine learning with systematic density-functional theory calculations: application to melting temperatures of single- and binary-component solids," *Physical Review B*, vol. 89, p. 054303, 2014.

[60] C. S. Kong, W. Luo, S. Arapan, P. Villers, S. Iwata, R. Ahuja, and K. Rajan, "Information-theoretic approach for the discovery of design rules for crystal chemistry," *Journal of Chemical Information and Modeling*, vol. 52, pp. 1812–1820, 2012.

[61] H. K. D. H. Bhadeshia, R. C. Dimitriu, S. Forsik, J. H. Pak, and J. H. Ryu, "Performance of neural networks in materials science," *Material Science and Technology*, vol. 25, pp. 504–510, 2009.

[62] L. Ward, A. Agrawal, A. Choudhary, and C. Wolverton, "A general-purpose machine learning framework for predicting properties of inorganic materials," *NPJ Computational Materials*, vol. 2, p. 16028, 2016.

[63] Ø. Grong, *Metallurgical modelling of welding*. London: Institute of Metals, 2nd ed., 1997.

[64] O. R. Myhr, Ø. Grong, and S. J. Andersen, "Modelling of the age hardening behaviour of Al-Mg-Si alloys," *Acta Materialia*, vol. 49, pp. 65–75, 2001.

[65] T. F. Kelly, P. P. Camus, D. J. Larson, L. M. Holzman, and S. S. Bajikar, "On the many advantages of local-electrode atom probes," *Ultramicroscopy*, vol. 62, pp. 29–42, 1996.

[66] T. F. Kelly and D. J. Larson, "Local electrode atom probes," *Materials Characterization*, vol. 44, pp. 59–85, 2000.

[67] E. A. Marquis and J. M. Hyde, "Applications of atom-probe tomography to the characterisation of solute behaviours," *Materials Science and Engineering R*, vol. 69, pp. 37–62, 2010.

[68] J. A. Panitz, S. B. McLane, and E. W. Müller, "Calibration of the Atom Probe FIM," *Review of Scientific Instruments*, vol. 40, pp. 1321–1324, 1969.

[69] M. K. Miller and R. G. Forbes, "Atom probe tomography," *Materials Characterization*, vol. 60, pp. 461–469, 2009.

[70] K. Thompson, D. Lawrence, D. J. Larson, J. D. Olson, T. F. Kelly, and B. Gorman, "In situ site-specific specimen preparation for atom probe tomography," *Ultramicroscopy*, vol. 107, pp. 131–139, 2007.

[71] O. C. Hellman, J. A. Vandenbroucke, J. Rüsing, D. Isheim, and D. N. Seidman, "Analysis of Three-dimensional Atom-probe Data by the Proximity Histogram," *Microscopy and Microanalysis*, vol. 6, pp. 437–444, 2000.

[72] O. C. Hellman, J. B. du Rivage, and D. N. Seidmam, "Efficient sampling for three-dimensional atom probe microscopy data," *Ultramicroscopy*, vol. 95, pp. 199–205, 2003.

[73] C. K. Sudbrack, D. Isheim, R. D. Noebe, N. S. Jacobson, and D. N. Seidman, "The influence of tungsten on the chemical composition of a temporally evolving nanostructure of a model Ni-Al-Cr superalloy," *Microscopy and Microanalysis*, vol. 10, pp. 355–365, 2004.

[74] K. Matsuda, Y. Sakaguchi, Y. Miyata, Y. Uetani, T. Sato, A. Kamio, and S. Ikeno, "Precipitation sequence of various kinds of metastable phases in Al-1.0mass% Mg2Si-0.4mass% Si alloy," *Journal of Materials Science*, vol. 35, pp. 179–189, 2000.

[75] C. D. Marioara, H. Nordmark, S. J. Andersen, and R. Holmestad, "Post-β" phases and their influence on microstructure and hardness in 6xxx Al-Mg-Si alloys," *Journal of Materials Science*, vol. 41, pp. 471–478, 2006.

[76] C. D. Marioara, S. J. Andersen, T. N. Stene, H. Hasting, J. Walmsley, A. T. J. Van Helvoort, and R. Holmstad, "The effect of Cu on precipitation in Al-Mg-Si alloys," *Philosophical Magazine*, vol. 87, pp. 3385–3413, 2007.

[77] C. D. Marioara, S. J. Andersen, J. Røyset, O. R. S. Gulbrandsen-Dahl, T. E. Nicolaisen, I. E, Opheim, J. F. Helgaker, and R. Holmestad, "Improving Thermal Stability in Cu-Containing Al-Mg-Si Alloys by Precipitate Optimization," *Metallurgical and Materials Transactions A*, vol. 45A, pp. 2938–2949, 2014.

[78] A. Frøseth, R. Høier, P. M. Derlet, S. J. Andersen, and C. D. Marioara, "Bonding in MgSi and Al-Mg-Si compounds relevant to Al-Mg-Si alloys," *Physical Review B*, vol. 67, p. 224106, 2003.

[79] S. J. Andersen, C. D. Marioara, R. Vissers, A. Frøseth, and H. W. Zandbergen, "The structural relation between precipitates in Al-Mg-Si alloys, the Al-matrix and diamond silicon, with emphasis on the trigonal phase U1-$MgAl_2Si_2$," *Materials Science and Engineering A*, vol. 444, pp. 157–169, 2007.

[80] S. J. Andersen, C. D. Marioara, A. Frøseth, R. Vissers, and H. W. Zandbergen, "Crystal structure of the orthorhombic U2-$Al_4Mg_4Si_4$ precipitate in the Al-Mg-Si alloy system and its relation to the β' and β" phases," *Materials Science and Engineering A*, vol. 390, pp. 127–138, 2005.

[81] S. D. Dumolt, D. E. Laughlin, and J. C. Williams, "Formation of modified β' phase in aluminum alloy 6061," *Scripta Metallurgica*, vol. 18, pp. 1347–1350, 1984.

[82] K. Matsuda, Y. Uetani, T. Sato, and S. Ikeno, "Metastable Phases in an Al-Mg-Si Alloy Containing Copper," *Metallurgical and Materials Transactions A*, vol. 32A, pp. 1293–1299, 2001.

[83] C. Cayron, L. Sagalowicz, O. Beffort, and P. Buffat, "Structural phase transition in Al-Cu-Mg-Si alloys by transmission electron microscopy study on an Al-4 wt% Cu-1 wt% Mg-Ag alloy reinforced by SiC particles," *Philosophical Magazine A*, vol. 79, pp. 2833–2851, 1999.

[84] R. K. Mishra, A. K. Sachdev, and W. J. Baxter, "Strengthening Precipitates In Cast 339 Aluminum Alloy," *AFS Transactions*, vol. 112, pp. 179–191, 2004.

[85] J. Y. Hwang, R. Banerjee, H. W. Doty, and M. J. Kaufman, "The effect of Mg on the structure and properties of Type 319 aluminum casting alloys," *Acta Materialia*, vol. 57, pp. 1308–1317, 2009.

[86] M. W. Zandbergen, A. Cerezo, and G. D. M. Smith, "Study of precipitation in Al-Mg-Si Alloys by atom probe tomography II. Influence of Cu additions," *Acta Materialia*, vol. 101, pp. 149–158, 2015.

[87] A. R. Akbarzadeh, C. Wolverton, and V. Ozolins, "First-principles determination of crystal structures, phase stability, and reaction thermodynamics in the Li-Mg-Al-H hydrogen storage system," *Physical Review B*, vol. 79, p. 184102, 2009.

[88] M.-R. He, S. K. Samudrala, G. Kim, P. J. Felfer, A. J. Breen, J. M. Cairney, and D. S. Gianola, "Linking stress-driven microstructural evolution in nanocrystalline aluminium with grain boundary doping of oxygen," *Nature Communications*, vol. 7, p. 11225, 2015.

[89] M. Rajagopalan, M. A. Bhatia, M. A. Tschopp, D. J. Srolovitz, and K. N. Solanki, "Atomic-scale analysis of liquid-gallium embrittlement of aluminum grain boundaries," *Acta Materialia*, vol. 73, pp. 312–325, 2014.

[90] G. A. Edwards, K. Stiller, G. L. Dunlop, and M. J. Couper, "The precipitation sequence in Al-Mg-Si Alloys," *Acta Metallurgica*, vol. 46, pp. 3893–3904, 1998.

[91] A. Löffler, J. Gröbner, M. Hampl, H. Engelhardt, R. Schmid-Fetzer, and M. Rettenmayr, "Solidifying incongruently melting intermetallic phases as bulk single phases using the example of Al2Cu and Q-phase in the Al-Mg-Cu-Si system," *Journal of Alloys and Compounds*, vol. 515, pp. 123–127, 2012.

[92] M. Asta and V. Ozoliņš, "Structural, vibrational, and thermodynamic properties of Al-Sc alloys and intermetallic compounds," *Physical Review B*, vol. 64, p. 094104, 2001.

[93] W. Ostwald *Zeitschrift für Physikalische Chemie*, vol. 37, p. 385, 1901.

[94] I. M. Lifshitz and V. V. Slyozov, “The Kinetics of Precipitation from Supersaturated Solid Solutions,” *Journal of Physics and Chemistry of Solids*, vol. 19, pp. 35–50, 1961.

[95] C. Wagner, “Theorie der Alterung von Niederschlägen durch Umlösen,” *Zeitschrift für Elektrochemie*, vol. 65, pp. 581–591, 1961.

[96] S. Björklund, L. F. Donaghey, and M. Hillert, “The effect of alloying elements on the rate of ostwald ripening of cementite in steel,” *Acta Metallurgica*, vol. 20, pp. 867–874, 1972.

[97] C. J. Kuehmann and P. W. Voorhees, “Ostwald Ripening in Ternary Alloys,” *Metallurgical and Materials Transactions*, vol. 27a, pp. 937–943, 1996.

[98] A. Umantsev and G. B. Olson, “Ostwald Ripening in Multicomponent Alloys,” *Scripta Metallurgica et Materialia*, vol. 29, pp. 1135–1140, 1993.

[99] J. E. Morral and G. R. Purdy, “Particle coarsening in binary and multicomponent alloys,” *Scripta Metallurgica et Materialia*, vol. 30, pp. 905–908, 1994.

[100] J. E. Morral and G. R. Purdy, “Thermodynamics of particle coarsening,” *Journal of Alloys and Compounds*, vol. 220, pp. 132–135, 1995.

[101] T. Philippe and P. W. Voorhees, “Ostwald ripening in multicomponent alloys,” *Acta Materialia*, vol. 61, pp. 4237–4244, 2013.

[102] G. R. Speich and R. A. Oriani, “The Rate of Coarsening of Copper Precipitate in an Alpha-Iron Matrix,” *Transactions of the Metallurgical Society of AIME*, vol. 233, pp. 623–631, 1965.

[103] H. C. Lee, S. M. Allen, and M. Grujicic, “Coarsening resistance of M_2C carbides in secondary hardening steels: Part I. theoretical model for multicomponent coarsening kinetics,” *Metallurgical Transactions A*, vol. 22A, pp. 2863–2868, 1991.

[104] C. A. Johnson, “Generalization of the Gibbs-Thomson Equation,” *Surface Science*, vol. 3, pp. 429–444, 1965.

[105] E. A. Brandes and G. B. Brook, *Smithells Metals Reference Book*. Oxford: Butterworth-Heinemann, 7 ed., 1992.

[106] S. Fujikawa and K. Hirano, “Impurity-Diffusion of Copper in Aluminum,” *Defect and Diffusion Forum*, vol. 66-69, pp. 447–452, 1989.

[107] S. Dais, R. Messer, and A. Seeger, "Nuclear-Magnetic-Resonance Study of Self-Diffusion in Aluminium," *Materials Science Forum*, vol. 15-18, pp. 419–424, 1987.

[108] R. W. Balluffi, S. M. Allen, and W. C. Carter, *Kinetics of Materials*. John Wiley & Sons, 1 ed., 2005.

[109] D. A. Porter, K. E. Easterling, and H. Y. Sherif, *Phase Transformations in Metals and Alloys*. CRC Press, 3 ed., 2009.

[110] C. D. Marioara, S. J. Andersen, J. Jansen, and H. W. Zandbergen, "The influence of temperature and storage time at RT on nucleation of the β"-phase in a 6082 Al-Mg-Si alloy," *Acta Materialia*, vol. 51, pp. 789–796, 2003.

[111] D. Vaughan and J. M. Silcock, "Discussion of "Machanisms of formation of θ precipitates in Al-4%Cu" by C. Laird and H. I. Aaronson," *Acta Metallurgica*, vol. 15, pp. 658–660, 1967.

[112] A. Biswas, D. J. Siegel, C. Wolverton, and D. N. Seidman, "Precipitates in Al-Cu alloys revisited: Atom-probe tomographic experiments and first-principles calculations of compositional evolution and interfacial segregation," *Acta Materialia*, vol. 59, pp. 6187–6204, 2011.

[113] A. Deschamps, B. Decreus, F. De Geuser, T. Dorin, and M. Weyland, "The influence of precipitation on plastic deformation of Al-Cu-Li alloys," *Acta Materialia*, vol. 61, pp. 4010–4021, 2013.

[114] B. C. Muddle and I. J. Polmear, "The precipitate Ω Phase in Al-Cu-Mg-Ag Alloys," *Acta Metallurgica*, vol. 37, pp. 777–789, 1989.

[115] E. Orowan, *Symposium on Internal Stresses in Metals and Alloys*. London: Institute of Metals, 1947.

[116] M. F. Ashby, "Work hardening of dispersion-hardened crystals," *Philosophical Magazine*, vol. 14, pp. 1157–1178, 1966.

[117] J. F. Nie, B. C. Muddle, and I. J. Polmear, "The effect of Precipitate Shpae and Orientation on Dispersion Strengthening in High Strength ALuminium Alloys," *Materials Science Forum*, vol. 217-222, pp. 1257–1262, 1996.

[118] J. F. Nie and B. C. Muddle, "Microstructural Design of High-Strength Aluminum Alloys," *Journal of Phase Equilibria*, vol. 19, pp. 543–551, 1998.

[119] J. F. Nie and B. C. Muddle, "Strengthening if an AL-Cu-Sn alloys by deformation-resistant precipitate plates," *Acta Materialia*, vol. 56, pp. 3490–3501, 2008.

[120] N. F. Mott and F. R. N. Nabarro *Physcial Society Bristol Conference, Report*, pp. 1–19, 1948.

[121] R. Labusch, "A Statistical Theory of Solid Solution Hardening," *Physica Status Solidi B*, vol. 41, pp. 659–669, 1970.

[122] R. Labusch, "Statistische theorien der mischkristallhärtung," *Acta Metallurgica*, vol. 20, pp. 917–927, 1972.

[123] G. P. M. Leyson and W. A. Curtin, "Friedel vs. Labusch: the strong/weak pinning transition in solute strengthened metals," *Philosophical Magazine*, vol. 93, pp. 2428–2444, 2013.

[124] G. P. M. Leyson, L. G. Hector Jr., and W. A. Curtin, "Solute strengthening from first principles and application to aluminum alloys," *Acta Materialia*, vol. 60, pp. 3873–3884, 2012.

[125] H. R. Shercliff and M. F. Ashby, "A process model for age hardening of aluminum alloys- I. the model," *Acta Materialia*, vol. 38, pp. 1789–1802, 1990.

[126] P. Feltham, "Solid solution hardening of metal crystals," *British Journal of Applied Physics*, vol. 1, pp. 303–308, 1968.

[127] M. Z. Butt, K. M. Chaudhary, and P. Feltham, "Plastic flow in BCC solid solutions," *Journal of Materials Science*, vol. 18, pp. 840–846, 1983.

[128] M. Z. Butt, P. Feltham, and I. M. Ghauri, "On the temperature dependence of the flow stress of metals and solid solutions," *Journal of Materials Science*, vol. 21, pp. 2664–2666, 1986.

[129] M. Z. B. 1988, "Correlation between temperature dependence of critical resolved shear stress and nature of solute distribution in aluminium-magnesium alloys," *Journal of Materials Science Letters*, vol. 7, pp. 879–880, 1988.

[130] P. Feltham and N. Kauser, "Solid-Solution Hardening," *Physica Status Solidi A*, vol. 117, pp. 135–140, 1990.

[131] M. Z. Butt, "Stress equivalence of solid-solution hardening," *Journal of Physics: Condensed Matter*, vol. 2, pp. 5797–5808, 1990.

[132] M. Z. Butt and P. Feltham, "Review Solid-solution hardening," *Journal of Materials Science*, vol. 28, pp. 2557–2576, 1993.

[133] F. Lasagni and H. P. Degischer, "Enhanced Young's Modulus of Al-Si Alloys and Reinforced Matrices by Co-continuous Structures," *Journal of Composite Materials*, vol. 44, pp. 739–755, 2010.

[134] R. L. Fullman, "Measurement of approximately cylindrical particles in opaque samples," *Trans Metall AIME*, vol. 197, pp. 1267–1268, 1953.

[135] D. J. Bacon, U. F. Kocks, and R. O. Scattergood, "The effect of dislocation self-interaction on the orowan stress," *Philosophical Magazine*, vol. 28, pp. 1241–1263, 1973.

[136] V. Mohles, "Simulations of dislocation glide in overaged precipitation-hardened crystals," *Philosophical Magazine A*, vol. 81, pp. 971–990, 2001.

[137] H. Liu, Y. Gao, L. Qi, Y. Wang, and J. Nie, "Phase-Field Simulation of Orowan Strengthening by Coherent Precipitate Plates in an Aluminum Alloy," *Metallurgical and Materials Transactions A*, vol. 46A, pp. 3287–3301, 2015.

[138] A. W. Zhu and E. A. Starke, "Strengthening effect of unshearable particles of finite size: a computer experimental study," *Acta Materialia*, vol. 47, pp. 3263–3269, 1999.

[139] P. G. Shewmon, *Diffusion in Solids*. New York: McGraw Hill, 1963.

[140] M. Jobba, R. K. Mishra, and M. Niewczas, "Flow stress and work-hardening behaviour of Al-Mg binary alloys," *International Journal of Plasticity*, vol. 65, pp. 43–60, 2015.

[141] V. P. Podkuyko and V. V. Pustovalov, "Peculiar mechanical properties of aluminium-magnesium, aluminium-copper and aluminium-zinc alloys at low temperatures," *Cryogenics*, vol. 18, pp. 589–595, 1978.

[142] E. M. Taleff, L. G. Hector Jr., J. R. Bradley, R. Verma, and P. E. Krajewski, "The effect of stree state on high-temperature deformation of fine-grained aluminum-magnesium alloy AA5083 sheet," *Acta Materialia*, vol. 57, pp. 2812–2822, 2009.

[143] U. F. Kocks, "Statistical Treatment of Penetrable Particles," *Canadian Journal of Physics*, vol. 45, pp. 737–755, 1967.

[144] Z. Zhu and M. J. Starink, "Solution strengthening and age hardening capability of Al-Mg-Mn alloys with small additions of Cu," *Materials Science and Engineering A*, vol. 488, pp. 125–133, 2008.

[145] Z. Zhu and M. J. Starink, “Age hardening and softening in cold-rolled Al-Mg-Mn alloys with up to 0.4 wt% Cu,” *Materials Science and Engineering A*, vol. 489, pp. 138–149, 2008.

[146] M. J. Starink, P. Wang, I. Sinclair, and P. J. Gregson, “Microstructure and strengthening of Al-Li-Cu-Mg alloys and MMCS: II. Modelling of yield strength,” *Acta Materialia*, vol. 47, pp. 3855–3868, 1999.

[147] G. I. Taylor, “Plastic Strain in Metals,” *The Journal Institute of Metals*, vol. 62, pp. 307–324, 1938.

[148] U. F. Kocks, “The relation between polycrystal deformation and single-crystal deformation,” *Metallurgical and Materials Transactions*, vol. 1, pp. 1121–1143, 1970.

[149] W. A. Anderson, *Precipitation from Solid Solution*. Metals Park, Ohio: American Society of Metals, 1959.

[150] M. Song, “Modeling the hardness and yield strength evolutions of aluminum alloy with rod/needle-shaped precipitates,” *Materials Science and Engineering A*, vol. 443, pp. 172–177, 2007.

[151] J. T. Vietz and I. J. Polmear, “The Influence of Small Additions of Silver on the Ageing of Aluminum Alloys: Observations on Al-Cu-Mg Alloys,” *Journal of the Institute of Metals*, vol. 94, pp. 410–419, 1966.

[152] J. H. Auld, J. T. Vietz, and I. J. Polmear, “T-phase Precipitation induced by the Addition of Silver to an Aluminum-Copper-Magnesium Alloy,” *Nature*, vol. 209, pp. 703–704, 1966.

[153] S. I. Fujikawa, “Impurity Diffusion of Scandium in Aluminum,” *Diffusion in Materials: Dimat-96*, pp. 115–120, 1997.

[154] D. Bergner and N. van Chi, “Untersuchungen zur Diffusion von 3d-Metallen in Al,” *Wissenschaftliche Zeitschrift der Pädagogischen Hochschule*, vol. 15, p. 15, 1977.

[155] G. Rummel, T. Zumkley, M. Eggersmann, K. Freitag, and H. Mehrer, “Diffusion of Implanted 3d-Transition Elements in Aluminum. Part I: Temperature Dependence,” *Zeitschrift fÃijr Metallkunde*, vol. 86, pp. 122–130, 1995.

[156] G. Erdelyi, D. L. Beke, F. J. Kedves, and I. Godeny, “Determination of Diffusion Coefficients of Zn, Co and Ni in Aluminum by a Resistometric Method,” *Philosophical Magazine B*, vol. 38, pp. 445–462, 1978.

[157] N. L. Peterson and S. J. Rothman, "Impurity Diffusion in Aluminum," *Physical Review B*, vol. 1, pp. 3264–3273, 1970.

[158] T. Marumo, S. Fujikawa, and K. Hirano, "Diffusion of Zirconium in Aluminum," *Journal of the Japan Institute of Light Metals*, vol. 23, pp. 17–25, 1973.

[159] N. van Chi and D. Bergner, "Diffusion of Mo and W in Al," in *DIMETA-82: Diffusion in Metals and Alloys* (F. J. Kedves and D. L. Beke, eds.), pp. 334–337, Trans Tech Publications, 1983.

[160] S. P. Murarka and R. P. Agarwala, "Diffusion of Rare Earth Elements in Aluminum," Tech. Rep. 368, Government of India Atomic Energy Commision, 1968.

[161] S. I. Fujikawa, "Solid State Diffusion in Light Metals," *Journal of the Japan Institute of Light Metals*, vol. 46, pp. 202–215, 1996.

[162] D. N. Seidman, E. A. Marquis, and D. C. Dunand *Acta Materialia*, vol. 50, pp. 4021–4035, 2002.

[163] E. A. Marquis and D. N. Seidman, "Nanoscale Structural Evolution of Al_3Sc Precipitates in Al(Sc) Alloys," *Acta Materialia*, vol. 49, pp. 1909–1919, 2001.

[164] A. Biswas, D. Siegel, and D. N. Seidman, "Simultaneous Segregation at Coherent and Semicoherent Heterophase Interfaces," *Physical Review Letters*, vol. 105, p. 076102, 2010.

[165] D. J. Skinner, R. L. Bye, D. Raybould, and A. M. Brown, "Dispersion strengthened AlFeVSi alloys," *Scipta Metallurgica*, vol. 20, pp. 867–872, 1986.

[166] K. Matsuda, D. Teguri, T. Sato, Y. Uetani, and S. Ikeno, "Cu Segregation around Metastable Phase in Al-Mg-Si Alloy with Cu," *Materials Transactions*, vol. 48, pp. 967–974, 2007.

[167] R. Tibshirani, "Regression Shrinkage and Selection via the Lasso," *Journal of the Royal Statistical Society B*, vol. 58, pp. 267–288, 1996.

Appendix A Machine Learning Model for Growth of θ'-phase Plates

This appendix gives the details of the machine learning model used to generate functions for the growth and coarsening of θ'-phase plates. Both the diameter and thickness were modeled in terms of the natural log of each parameter, this was done due to the large scale over which they varied and to prevent any generated model from providing negative particle dimension values. The machine learning code works by taking a set of attributes which uniquely define each data point, applying function expanders to these attributes, selecting the best expanded attributes, and then generates a regression model using these. It was determined that the aging time, aging temperature, and bulk composition uniquely defined each datapoint of the set of particle dimensions. Two sets of function expanders were chosen for the diameter of the plates, where the first set acts on the input attributes, and the second set works on all combinations of the first set. The first set of function expanders are: $ln(x)$, x^2, x/y, and y/x. The second set of expanders are: $x \times y$ and $x \times y \times z$, where x, y, and z are any different attribute. The four expanded attributes that best describe the set of data are chosen using the least absolute shrinkage and selection operator (LASSO) regression analysis method [167]. A linear regression model is then found using 10-fold cross validation and all four of the chosen attributes. Similarly the thickness of the plates was modeled, with an additional function expander added to the first set: x^3.

The θ' plate diameters and thickness were measured for some of the alloys containing the θ'-phase, though an exhaustive literature review was performed to obtain particle sizes in a number of alloy systems. Data was found for aging temperatures ranging from 160°C to 260°C and alloy systems with a range of compositions: Cu from 0.62 at.% to 2.19 at.%, Mg from 0 at.% to 0.74 at.%, and Si from 0 at.% to 8.8 at.%. Training data for the thickness of the plates contained 59 unique aging times, temperatures, and compositions while data for the diameter had 58 data points. The equations for the two models are presented in the following equations:

$$t = exp\left(A + B\frac{ln(Cu)Cu}{T} + Cln(T)ln(t)T^3 + Dln(Cu)T^3Cu^3 + E\frac{T^3ln(Cu)Cu}{t}\right)$$

$$d = exp\left(A + Bln(t) + C\frac{TMg}{Cu^2} + DT^2Cu^3 + E\frac{ln(T)ln(Cu)Cu}{T}\right)$$

were T is temperature in °C, t is time in hours, Cu and Mg are the bulk concentrations in at.%, and A, B, C, D, and E are constants. The constants are determined using linear regression and are given in Table A.1. Over the range of compositions, aging temperatures, and times explored in this study this equation demonstrates expected growth behavior.

Table A.1: Constant terms for the θ'-phase ML model.

Constant	Thickness Eqn.	Diameter Eqn.
A	1.120106798e+00	4.006566036e+00
B	-2.192931729e+02	1.746992408e-01
C	3.748897603e-09	-2.806013355e-03
D	2.444652992e-08	6.967091025e-06
E	7.605369338e-09	-6.784937232e+01

Appendix B High-Temperature Yield Strength Data

This appendix gives the raw data for the high-temperature yield strength study performed in Chapter 5. Tensile tests were performed by General Motors as described in Chapter 2. All tensile specimens were aged at 200°C for either 4 or 5 hrs to peak strength, then conditioned at the testing temperature for 200 hrs. Bulk alloy compositions as determined using OES for the HT alloys are given in Table B.1 except for Alloy1. Tensile data pulled at temperature after 200 hrs of conditioning is given in Table B.2.

Table B.1: Bulk alloy chemical compositions as determined by OES.

Alloy	Si (wt.%)	Mg (wt.%)	Cu (wt.%)
356	6.59	0.41	0
AS7GU	6.59	0.41	0.5
CTQ	5.30	0.27	3.16
CQ	5.90	0.49	0.81
WQ	0.74	0.49	0.75
Eut-Q	12.2	0.48	0.8

Table B.2: High-temperature yield strength data.

Alloy	Yield Strength at Temp. (MPa)					
	25°C	150°C	200°C	225°C	250°C	300°C
356	261	224	83	-	55	41
AS7GU	284.0	254.4	175.1	118.6	101.2	39.8
Alloy1	286.3	252.2	170.5	128.7	89.1	38.6
CTQ	364.6	325.0	190.5	123.7	69.8	41.6
CQ	272.8	254.6	147.0	105.8	78.9	41.0
WQ	281.9	264.9	190.3	-	81.9	59.1
Eut Q	296.3	268.9	167.1	129.6	84.0	44.3